Ab ect

Galileo Orbiter Ultraviolet Observations of Jupiter Aurora

Joseph Ajello, Donald Shemansky*, Wayne Pryor+, Kent Tobiska^, Charles Hord+, Stuart Stephens*, Ian Stewart+, John Clarke#, Karen Simmons+, William McClintock+, Charles Barth+, Jeremy Gebben+, Deborah Miller+ and Bill Sandel@

JET PROPULSION LABORATORY
CALIFORNIA INSTITUTE OF TECHNOLOGY
PASADENA, CA 91109

+LABORATORY OF ATMOSPHERIC AND SPACE PHYSICS
UNIVERSITY OF COLORADO
BOULDER, CO 80303

*DEPARTMENT OF AEROSPACE ENGINEERING
UNIVERSITY OF SOUTHERN CALIFORNIA
LOS ANGELES, CA 90089

#SPACE PHYSICS RESEARCH LABORATORY
UNIVERSITY OF MICHIGAN
ANN ARBOR, MI 48109

^FDC/JET PROPULSION LABORATORY
PASADENA, CA 91109

@LUNAR AND PLANETARY LABORATORY
UNIVERSITY OF ARIZONA
TUCSON, AZ 85721

SUBMITTED TO:
JOURNAL OF GEOPHYSICAL RESEARCH-PLANETS

(SPECIAL ISSUE ON MAGNETOSPHERES OF THE OUTER PLANETS)

FAX: 626-393-4605
OFFICE: 626-354-2457
jajello@jpluvs.jpl.nasa.gov

MARCH 4 , 1998

Galileo orbiter ultraviolet observations of Jupiter aurora

Joseph Ajello,[1] Donald Shemansky,[2] Wayne Pryor,[3] Kent Tobiska,[4] Charles Hord,[3] Stuart Stephens,[4] Ian Stewart,[3] John Clarke,[5] Karen Simmons,[3] William McClintock,[3] Charles Barth,[3] Jeremy Gebben,[3] Deborah Miller,[3] and Bill Sandel[6]

Abstract. In 1996 during the first four orbits of the satellite tour the Galileo ultraviolet spectrometer (UVS) (1130-4320 Å) and extreme ultraviolet spectrometer (EUVS) (540-1280 Å) performed near-simultaneous observations of the Jupiter aurora in both the north and south polar regions. These observations are modeled to provide the absolute surface brightness of the aurora from the H_2 Rydberg Systems ($B, B', B'', C, D, D' \rightarrow X$ band systems). The spectral distribution and brightness of the EUV aurora are sensitive to H_2 abundance, H_2 temperature, and CH_4 abundance. Analysis of the emission spectra indicates that the EUV aurora (800-1200 Å) are produced over a range of altitudes corresponding to slant column abundances of H_2 from 10^{16} to 10^{20} cm^{-2} or greater. The UVS spectra of the far ultraviolet (FUV) from 1130 to 1700 Å are optically thin in H_2, but highly sensitive to the CH_4 column abundance and to the secondary electron energy distribution. The slant column abundance of CH_4 absorbers found from models of the FUV spectra varied in the range 0 - 10 x 10^{16} cm^{-2}, indicating the presence of both high altitude aurora, at or above the homopause, and deep aurora. The FUV spectra show C_2H_2 absorption bands near 1520 Å. The surface brightness of the aurora from the H_2 Rydberg Systems ranged from 100 to 600 kR and of H Lyman α was 60 to 130 kR for a 2000 km wide oval. The total power input to the atmosphere from particle deposition is estimated to be ~ 1 x 10^{14} W.

I. Introduction

Galileo began its planned 11-orbit tour of the Jupiter system in December 1995. The UV subsystem on the Galileo orbiter consists of two separate spectrometers. The extreme ultraviolet spectrometer (EUVS) measures radiation from 540 to 1280 Å and is on the spinning portion of the spacecraft. The ultraviolet spectrometer (UVS) is mounted on the scan platform and operates over the range from 1130 to 4320 Å [*Hord et al.*, 1992]. In the early orbits in 1996 at the time the boresight of the EUVS crossed the dawn terminator of Jupiter, simultaneous EUVS and UVS observations of the aurora from the same source location were performed. The spectra measured by each instrument provide important information about the energetics and structure of the aurora. The UVS far ultraviolet (FUV) observations furnish the CH_4 column abundance above the aurora and energy output of the Rydberg band systems of H_2, but provide no information on the H_2 foreground abundance. The EUVS also measures the energy output of the aurora and through self-absorption is sensitive to H_2 abundance and temperature, as well as CH_4 abundance. The energetics and CH_4 abundances ought to be self-consistent between the two sets of data.

These unique observations consisting of combined EUV and UVS spectra are an important step in understanding the Jupiter aurora. Voyager auroral EUV spectra obtained inside the magnetosphere were partially compromised by a high radiation environment. A single preliminary model is shown by *Broadfoot et al.* [1981]. Morphological studies by *Herbert et al.* [1987] of the northern aurora, from the outbound leg of Voyager 2, pinpointed the System III longitude, λ ~ 210° as a region of maximum brightness of H Lyα and H_2 bands and the southernmost extent of the aurora

as the footprint of the Io torus. In addition, the Voyager UVS spectral resolution was not sufficient to observe the CH_4 absorption structure. Recently, *Morrissey et al.* [1997] obtained simultaneous EUV/FUV spectra (900-1650 Å) and imaging of the Jovian aurora with the Hopkins Ultraviolet Telescope (HUT) and Hubble Space Telescope (HST). The HUT model analysis was limited to the wavelengths from 1000 to 1650 Å using molecular parameters of the H_2 Lyman and Werner system. Significant residuals existed in the 900-1000 Å wavelength region from the unmodeled higher Rydberg states. The Galileo EUVS observations provide excellent signal-to-noise (S/N) measurements inside the Jovian magnetosphere. The emergent spectrum from the Jupiter atmosphere is sensitive to gas temperature and H_2 abundance along the optical path. The resonance bands (v', 0) of the Rydberg band systems [*Ajello et al.*, 1984, 1988] appear in the 850-1100 Å wavelength range. If the gas temperature is near 1000 K and the H_2 column density above 10^{15} cm^{-2}, then the atmosphere is thick for both the (v', 0) and (v', 1) progressions, which extend to 1160 Å, a spectral region that begins to include the UVS. Multiple scattering in these bands is unimportant, since emissions in optically thick bands are fluoresced at longer wavelengths in optically thin bands of the same progression.

In this paper we report the EUVS auroral observations obtained on the "Big Four" set of orbits. The three sets of observations begin just prior to the satellite/Jupiter encounters: G1, C3, and E4. There were no EUVS/UVS aurora or torus spectra on G2. These first four orbits have large distances from Jupiter during the torus and aurora observation periods, roughly defined by 90° Jupiter phase angle. These orbits provided the least interference from radiation and the longest and most sensitive observations of the Jupiter aurora and Io torus. The geometry is shown in Figure 1 with the Io torus period. The period included 4 3/4 days per orbit for the torus and 1/4 day (6 hours) for the auroral observations by the EUVS. UVS observations of the aurora were planned for each orbit to accompany the EUVS. The total observation time per pole per orbit, considering the small duty cycle of the spinning EUVS, was 12 s. Excellent EUV spectra were obtained from these brief exposures. The EUVS acquired high-quality spectra of the aurora because of the smaller than expected radiation environment and an increased thickness of radiation shielding relative to the Voyager UVS. Modeling techniques developed by *Shemansky* [1985] were used as a basis for the EUV and FUV models.

Previous spectral information about the UV aurora is known from two decades of FUV measurements by International Ultraviolet Explorer (IUE), HUT, and HST Goddard high-resolution spectrometer (GHRS). The past history of FUV observations is extensive, consisting of both high-resolution spatial imaging (HST) in the Lyman bands and H Lyman α and spectral measurements of varying spectral coverage and resolution (GHRS high resolution echelle spectra of 0.07 Å full width at half maximum (FWHM) to IUE low resolution of 11 Å FWHM) [*Clarke et al.*, 1994; *Feldman et al.*, 1993; *Durrance et al.*, 1982;

Fig 1

Livengood et al., 1990; *Trafton et al.*, 1994; *Prange et al.*, 1995, 1997a,b; *Harris et al.*, 1996].

The most recent spectral model of the FUV aurora was published by *Liu and Dalgarno* [1996]. Using a prime set of HST GHRS observations from past observer cycles, *Liu and Dalgarno* derive H_2 auroral rotational temperatures of 400-600 K. The model includes the line transition probabilities of *Abgrall et al.* [1993a,b], a major improvement in modeling rotational-vibrational coupling. The model simulated the auroral spectra on the basis of primary electron beams of 20, 100, and 1000 eV energies and calculated the secondary electron distribution based upon cross sections for electron ionization, excitation, and dissociation of H_2. The model did not include photoabsorption of the calculated H_2 emissions. The secondary electron spectrum expected in the aurora is the basis of our current analysis. H_2 emission intensities are sensitive to the presence of low-energy electrons. The current analysis also includes effects of atmospheric absorption.

GHRS spectral line profiles of H Lyman α in the dayglow bulge region are highly structured and broad in the wings (~1 Å) [*Emerich et al.*, 1996], possibly from the collision of supersonic jets from the opposite poles. Global dynamics may be influenced by auroral processes. High-resolution H Lyman α line profiles in the aurora are found to be broad also, but with a self-reversed line core [*Prange et al.*, 1997b]. FUV wide-field planetary camera 2 (WFPC 2) imaging of the Jupiter aurora and Io footprint in the Lyman bands have been accomplished by *Clarke et al.* [1996] and *Ballester et al.* [1996]. *Trafton et al.* [1994] studied the northern aurora spectroscopically in the FUV with GHRS and observed the rotational lines of the Lyman system near 1600 Å and of the Werner system near 1270 Å. *Clarke et al.* [1994] and *Kim et al.* [1995] with GHRS studied the region of 1204 to 1241 Å. The reanalysis of the *Trafton et al.* [1994], *Kim et al.* [1995], and *Clarke et al.* [1994] results by *Liu and Dalgarno* [1996] gave auroral temperatures in the range of 400-600 K.

High-resolution spatial imaging by the faint object camera (FOC) was carried on by *Gerard et al.* [1993, 1994a]. They observed a transient bright arc in the north, indicating transient 3000 K or higher exosphere temperatures. In addition, *Gerard et al.* [1994b] performed a high spatial resolution single rotation morphological study of the northern aurora in 1993, finding that the auroral oval corresponded most closely to the L=30 R_J field line and that this auroral structure persists with time.

The most complete morphological study of the IUE data was accomplished by *Livengood et al.* [1990]. *Harris et al.* [1996] presented a second exhaustive analysis of the IUE data and included the Lyα line which *Livengood et al.* neglected. *Livengood et al.* analyzed a northern aurora data set of FUV spectra obtained from 1979-1989. They binned the data into two wavelength regions: the blue 1230-1300 Å and the red 1557-1619 Å as proposed by *Yung et al.* [1982]. The ratio of red/blue has been used as a measure of the CH_4 (principal hydrocarbon) optical depth in front of the auroral

layer with System III longitude. The two principal results of this study showed that the auroral brightness and the color ratio peaked at 180° longitude, indicating a maximum column density of CH_4 at 180° longitude with a variation of a factor of 2-3. This result could be interpreted as arising from an atmosphere that is uniform in longitude but has a longitude dependent energy in primary precipitating particles. A reconciliation of the long-term IUE results of *Livengood* (e.g., maximum brightness and color ratio at 180° longitude) with the WFPC 2 and FOC imaging is given by *Prange et al.* [1997a] and *Ballester et al.* [1996]. *Prange et al.* [1997a] give a summary of the southern aurora from IUE studies. A maximum in FUV brightness is observed at 0-40° System III longitude.

In this paper we report the first analysis of the near-simultaneous FUV and EUV spectra from three of the "Big Four" orbits, identified as Ganymede 1 (G1), Callisto 3 (C3), and Europa 4 (E4). In the next section, we describe the geometry and show the data. For each orbit, we show a pair of north and south observations for the UVS and EUVS instruments. We then briefly describe the model used to analyze the data. The model is an extension of earlier work by *Shemansky* [1985]. The following two sections show model fits to the UVS and EUVS data. A discussion section completes the paper and summarizes the data/model comparison.

2. Observations of the Jupiter Aurora

The instrument description for both the UVS and EUVS has been provided previously for the Galileo Phase 1 high-gain prime mission [*Hord et al.*, 1992]. With the loss of the high-gain antenna, telemetry rates were limited to a total of ~50 bits/s in the Galileo Phase 2 mission. To compensate, the UVS/EUVS flight software was rewritten to include a new summing capability for low light level sources or bright sources that do not fill the field of view. Real-time data transmission of the summed data allows the UVS and EUVS telemetry rates to be kept at a manageable 5 or 10 bits/s, while at the same time allowing the instrument to count all the photons to build S/N. In Phase 2 both instruments sum spectral regions over periods of time that are an integral number of real-time imagings (RIMs) (1 RIM = 60 2/3 s). The unit of time for the Galileo spacecraft clock is RIMs. For the auroral observations the times sequenced were normally 30 or 60 RIMS (1/2 or 1 hour). The UVS was given a 1092 word x 16 bits/word data buffer in the Command Data Subsystem (CDS) to continually store and co-add the spectral information at the original high-gain data rate of 1 spectrum per 4 1/3 s (546 words x 8 bits). The EUVS uses a portion of its own microprocessor for storing 1092 words of 16 bits/word spectral and engineering information. The instrument stores data as a two-dimensional array. One dimension represents wavelength, and the other dimension represents position in the sky. The wavelength dimension is stored as superpixels (45 for the aurora) and is a programmable set of the 126 spectral anode channels (5.9 Å per channel). The programmable set of

superpixels is read into the instrument microprocessor at the start of the aurora observations as the aurora fixed pattern noise table (FPNT). Superpixels vary in size from two to four channels. The aurora FPNT was chosen to optimize the resolution in the wavelength range for the H_2 Rydberg systems in the wavelength range 800-1250 Å; the torus FPNT was designed to achieve maximum resolution on the torus ion lines between 600 and 1200 Å. The sky position is divided into a programmable sector angle. A sector angle is the angle defined by the number of programmable scans (one for the aurora) times the spin rate (nominally 3.15 rpm) times the scan period for the detector (21.4 ms), resulting in a 0.4° sector angle. Sectors are scanned consecutively from the starting angle (~90° for the aurora) as measured from the north ecliptic pole until the commanded number of sectors have been scanned (24 for the aurora). EUVS spatial registration was improved in Phase 2 to be within ±1 detector scan (0.4°), whereas in Phase 1 the spatial registration was within 1.4°. This engineering change allows EUVS to obtain spatially resolved spectra of the poles and equator, which had an angular separation of about 0.8° as viewed from Galileo during a typical orbit of the Big Four.

Plate 1a shows typical geometry for a simultaneous EUVS/UVS observation on the C3 southern aurora, the first time a simultaneous UVS/EUV observation was obtained. The design shows both the UVS slit and the EUVS sector, which are aligned at right angles to one another. The EUVS boresight is mounted 90° to the spacecraft spin axis, which is the spacecraft cone angle reference axis. The UVS was commanded to the cone angle of 90° and the clock angle of the southern aurora. Both instruments use spacecraft (S/C) motion to carry the boresights through the target. For these orbits the drift lasts about 6 hours. We show in Plate 1b the three EUVS images from the Big Four orbits. They are labeled J0CD, G02C, and C03C for the name of the sequence loads that commanded the spacecraft in the approach to G1, C3, and E4, respectively. Although simultaneous UVS/EUVS observations occurred on some of these orbits, "simultaneous" is not synonymous with looking at the same area of the source region.

Plate 1

The EUVS images are presented as a Lyman α intensity (channels 100-120) in counts/s as a color brightness table (yellow is brightest) for each real-time data transmission. The image in the H_2 Rydberg system (channels 40-99) is shown side-by-side with the Lyman α image. The H Lyman α signal is caused by at least three processes, e.g., $H + e$, direct electron excitation from the auroral electrons or photoelectrons; and $H_2 + e$, dissociative excitation in the aurora and $H + h\nu$ solar fluorescence processes. The H_2 Rydberg bands are primarily excited by electron impact. The images of Jupiter show both dayglow and auroral signal rates in H Lyman α. The EUVS aurora image for the Rydberg bands stands out as bright intense stripes on each pole as the same sector number (the vertical axis) occurs for the brightest pixels for each spectral transmission, as the slit begins to drift across the two auroral regions. The horizontal axis is time as well as position in the sky. The

width of each pixel is either 1/2 hour or 1 hour, depending on the integration time between each spectral transmission.

On C3 the UVS was pointed to the south pole to maximize signals from the bright 0-50° longitudes. On E4 the UVS was pointed at the north pole to provide a high S/N UVS integration on the near-180° bright longitudes. For each of these orbits the UVS pointing was then changed at a later time to the opposite pole to complete a set of near-simultaneous observations with EUVS. The central meridian longitude (CML) at the center time of the spectral transmission is indicated for each orbit in Plate 1a. Black pixels or stripes indicate lost data. For the case of G1 the UVS data, obtained simultaneously with the EUVS, was flawed because of a grating anomaly at low spacecraft temperatures, a problem rectified on subsequent orbits by activating the UVS supplemental heater. The summary of the UVS/EUVS orbital data to be compared in this paper for the Big Four orbits are listed in Table 1.

We show the EUVS spectral data for each of the northern orbits in Figure 2 and each of the southern orbits in Figure 3 as an instrument count rate. The integration times in seconds for each of the spectra are indicated. The spectral resolution of the EUVS is 35 Å FWHM. A total of about 12 s (0.2 RIM) per orbit per pole is obtained with the angular duty cycle of 4.7 x 10^{-4} for the spinning EUVS 0.17° instantaneous field of view. The peak counts in a channel obtained in a single spectrum is about 10 counts. Hence meaningful analysis can only be performed on the entire accumulated spectrum for each orbit. For example, the peak Lyman α signal on E4 north is 80 counts in 361 RIM of continuous spin-scan imaging (10.3 s observation time of target). The wavelength-integrated accumulated spectrum of 1232 counts represents an average EUV aurora spectrum for over a 1/2 rotation of Jupiter. The wavelength scale is divided into superpixels for data collection; the spectrum is reconstructed with the count information divided equally among spectral channels contained within a superpixel. In these data the background from radiation environment and the torus background have been subtracted. The radiation environment produces a variable background count rate. The count rate varies between ~ 0.023 c/s/pixel (0.3 c/0.2 RIM/pixel), a minimum value at the same level as the radioisotope thermoelectric generator (RTG) cruise rate, to 0.29 c/s/pixel, a maximum rate at the centrifugal equator at 55 R_J and is negligible. The estimated torus background signal (solid curve) for the length of time of the observation is shown in Figure 4, compared to the G1 north total signal (dotted curve). The estimated torus background is obtained from the total EUVS torus spectrum from the Big Four set of orbits. The G1 torus background to the auroral signal below 800 Å shows a spectral shape with a peak signal 0.5 c/s/pixel (6 counts/0.2 RIM/pixel) at 690 Å. The integrated interplanetary H Lyman α signal with a maximum count rate of 2.4 c/s (29 c/0.2 RIM) over channels 100-120 is small compared to the auroral signal. For example, the auroral signal level at H Lyman α on C3 north is 799 c/0.2 RIM. The interplanetary signal level is equivalent to 676 R. A nominal FWHM of six channels with broad wings is found

Fig 2
Fig 3

Fig 4

for H Lyman α. The total count spectrum over the G1-E4 orbits is shown in Figure 5 with the 1σ error bars from signal statistics. The signal statistics are based on the fact that, on the average, a detected photon event produces 2.5 channel counts. The spectral structure of the data shows fundamental differences between north and south. However, both data sets show wavelength thresholds of near 880 Å. At wavelengths below H Lyman α the signal is much weaker and washed out in the south. It is characteristic of deeper penetration by the primary particles or a difference in the auroral atmospheres between north and south or limb effects. For example, the wavelength peaks at 1030 and 1100 Å are much stronger in the north. Data from later orbits will be used to further study this trend.

Fig 5

We turn our attention to the UVS spectra that were obtained simultaneously or closest in time with the six EUVS spectra above (three in the north and three in the south). We show the UVS north spectra for G1, C3, and E4 and the preflight electron impact spectrum of H_2 at 100 eV discussed in the calibration publications in absolute count rate in Figure 6 and relative intensity, normalized to 1580 Å in Figure 7 [*Ajello et al.*, 1988; *Hord et al.*, 1992]. The spectral resolution of the UVS is 6.5 Å FWHM. In Figures 8 and 9 we show the corresponding spectra for the south. Only C3 south and E4 north were simultaneous with the EUVS. G1 and E4 north spectra were able to capture the bright aurora from near 180° longitude. The observations used in the G1 comparison were obtained several days later, as shown in Table 1. They actually occurred in the official G1 sequence period, whereas EUVS observations were obtained in the J0CD sequence period. The count rates were highest in G1 near the bright 180° longitude, indicating a bright northern aurora. The count rate in the H_2 bands in the FUV for full spectral scans of 528 channels is determined by the UVS duty cycle of either 14 (G-G photomultiplier (PMT)) spectral scans or 7(F-G photomultipliers) scans per RIM. There are three separate PMTs located behind three separate exit slits in the focal plane of the spectrometer [*Hord et al.*, 1992]. The integration time for each of the 528 channels (1.5 Å/channel width) in the G-PMT wavelength range of 1133 - 1931 Å is 6 ms per spectrum, summed over the integration times per channel indicated in Figures 6 and 7. The signal rate was smallest in C3 north for the opposite side of the northern auroral oval than was measured in G1. The background count rate in the set of UVS observations is small, ~4 c/s/channel. The preflight laboratory electron impact spectrum has the lowest color ratio *CR* [*Livengood et al.*, 1990].

Fig 6
Fig 7
Fig 8
Fig 9

$$CR = 4\pi I_{1557\text{-}1619\text{Å}} / 4\pi I_{1230\text{-}1300\text{Å}}. \qquad (1)$$

and $4\pi I_\lambda$ is the monochromatic line intensity. The color ratio is used as a figure of merit to compare the amount of CH_4 absorption and other hydrocarbon absorption that is strong below 1400 Å. We show in Figure 7 the relative spectra. The presence of CH_4 absorption and other absorption in the region is clear, when compared to the

laboratory spectrum. The laboratory spectrum is stronger at all wavelengths below 1400 Å. Although the signal levels vary by a factor of 3 in the north, the amount of absorption appears nearly the same for the three analyzed spectra. E4 has slightly less absorption below 1400 Å than G1 or C3.

The southern aurorae show a much larger variation in both signal level and absorption. Figure 8 shows the three southern auroral observations. The signal level in the south was largest for G1 dayside. The relative spectrum is shown in Figure 9. The variation in color ratio is striking. E4, which is the weakest spectrum in terms of count rate, is similar to the northern auroral spectra earlier. E4 shows the smallest amount of absorption, when compared to the laboratory spectrum. G1 and C3, which were very strong, occur over similar System III longitudes and show a large amount of absorption. G1 and C3 represent relatively deep aurora. The color ratio change is a factor of 5.

Support imaging by the Galileo solid state imaging (SSI) system did not occur early in the mission. A cycle 5 HST program was in place to obtain aurora images at the same time as the G1 (G1JUFIXTMD, sequence observation name) north and G1 (G1JUAURMAP) south observations. Auroral images were obtained using the WFPC 2 Na Wood's filter F160WB [*Clarke et al.*, this issue]. The south aurora image, projected back in time, for the CML of the UVS observation is shown in Plate 2. The north aurora image, projected back in time, for the CML of the UVS observation is shown in Plate 3. The bright aurora in the north near the limb was observed by the UVS in G1. A few hours earlier, the bright aurora shown in the south was in the UVS field of view. Both observations were well placed on the WFPC 2 reference oval [*Clarke et al.*, 1996] to capture the bright auroral longitude regions (185° in the north and 23° in the south for G1) established from IUE and HST diagnostics of the aurora [*Prange et al.*, 1997a]. The figures show the latitude-longitude grid system of Jupiter at the time of the observation.

Plate 2
Plate 3

3. Data Analysis

The signal that is measured by the UVS or EUVS, summed over all channels for a monochromatic source at wavelength λ that partially fills the field of view can be expressed

$$C_\lambda\,(\mathrm{c/s}) = 4\pi I_\lambda(\mathrm{R})\, k_\lambda^{\mathrm{ext}}\,(\mathrm{c/s/R})\, f_{\mathrm{duty}} f_{\mathrm{fill}} \qquad (2)$$

where $4\pi I_\lambda$ is the total surface brightness in rayleighs (R) (units of 10^6 photons/cm^2 s) at the top of the atmosphere, k_λ^{ext} is the instrument calibration for an extended source and contains the factors relating to the instrument field of view, transmission characteristics, and detector quantum efficiency, f_{duty} is the duty cycle for the spectral bandpass (4.44 channels), and f_{fill} is the fill factor for the observation. The fill factors have been given in Table 1 for all the observations. The fill factor is defined as the percentage of the field of view that is filled by the auroral source. This

factor is based on an auroral oval that is 2000 km wide and is uniformly bright over the circumference of the $L = 30$ R_J footprint from the reference oval [*Clarke et al.*, 1996]. (A recent analysis of an observation of the auroral oval by SSI on orbit G7 indicates a much smaller width of ~ 200 km (A. Ingersoll et al., Imaging Jupiter's aurora at visible wavelengths, submitted to *Icarus*, 1998; hereinafter referred to as submitted paper); a 10 times smaller width would require a factor of 10 increase in the intensities derived here). The longitude-latitude dependence of reference auroral ovals has been established by WFPC 2 [*Clarke et al.*, 1996], which are close to the $L = 30$ R_J footprint in updated magnetic field models. The duty cycle for the EUVS has already been given as 4.722×10^{-4} arising from the spin-scan imaging mode for the array detector; the duty cycle for the UVS is based on the single pixel wavelength scan required to build up a spectrum. For example, for a G-G PMT scan the duty cycle is 1.385×10^{-3} per channel or 6.155×10^{-3} per monochromatic line. The k_λ^{cal} calibration factors that were used are given in the instrument description paper [*Hord et al.*, 1992] and represent the current performance of the instrument based on in-flight calibration at H Lyman α from observations of the interplanetary hydrogen glow [*Ajello et al.*, 1994; *Pryor et al.*, 1992]. The sensitivity at H Lyman α for the UVS is 170 c/s/kR and for the EUVS is 3.35 c/s/kR. The Lyman α intensities measured by the two instruments are within a factor of 2 for the C3 south and E4 north simultaneous auroral observations. The factor of 2 agreement is attributed to field of view differences. These intensities vary between 145 kR and 106 kR for the EUVS and 65 and 103 kR for the UVS on C3 and E4, respectively and will scale upward by a factor of 10 for a 200 km wide auroral arc. The Rydberg band contribution to the brightness in the channels of H Lyman α has been removed. This correspondence between the instruments is reasonable, given the different fields of view of the two instruments. The intensity of the Rydberg bands of H_2 should be about 10 times brighter than H Lyman α, since the total electron cross section for the entire Rydberg system is about 10 times the H Lyman α dissociative cross section [*Liu et al.*, 1998].

The model monochromatic line intensity, $4\pi I_\lambda^{mod}$, emerging from an auroral atmosphere of H_2, CH_4, C_2H_2, and other hydrocarbons penetrated to altitude z by a primary particle, ion, or electron is given by

$$4\pi I_\lambda^{mod}(\infty) = g_\lambda \eta(z+\Delta z: H_2)\, Tr[\tau_\lambda(\eta(\infty:H_2))]$$

$$Tr[\tau_\lambda(\eta(\infty:CH_4))]\, Tr[\tau_\lambda(\eta(\infty:C_2H_2))] \qquad (3)$$

Where g_λ is the emission rate per molecule per second in a particular rotational line $J' \rightarrow J''$; $\eta(z+\Delta z:H_2)$ is the column density of H_2 emitters in a layer, Δz thick (nominally several scale heights in this analysis), at altitude z for the lower edge of the layer and $Tr[\tau_\lambda(\eta(\infty:H_2))]$ is a transmission function through H_2 gas based on a curve of growth formulation of Voigt line profiles and molecular H_2 ionization, and $Tr[\tau_\lambda(\eta(\infty:CH_4))]$ and $Tr[\tau_\lambda(\eta(\infty:C_2H_2))]$

are continuum absorption terms for CH_4 and C_2H_2, respectively. The notation η (∞:H_2), η (∞:CH_4), and η (∞:C_2H_2) are the column densities of H_2, CH_4, and C_2H_2 absorbers present to the top of the atmosphere as measured from a layer at altitude z. In this paper we assume two analytic forms for hydrocarbon absorption in the region of the homopause. First, we assume that for CH_4 and C_2H_2, the product of transmission functions is given by

$$Tr[\tau_\lambda(\eta(\infty{:}CH_4))]\,Tr[\tau_\lambda(\eta(\infty{:}C_2H_2))]$$

$$= \exp[-\tau_\lambda(CH_4)]\exp[-\tau_\lambda(C_2H_2)] \qquad (4)$$

This equation is an approximation of extinction by absorber foreground gases separated from the emission region [*Shemansky*, 1985]. Second, we use the analytic solution for a Chapman layer aurora in a homogeneous H_2, CH_4, and C_2H_2 atmosphere. In this case it can be shown (G.R. Gladstone, private communication, 1997) that the product

$$Tr[\tau_\lambda(\eta(\infty{:}CH_4))]\,Tr[\tau_\lambda(\eta(\infty{:}C_2H_2))]$$

$$= 1./[1. + \tau_\lambda(CH_4) + \tau_\lambda(C_2H_2)] \qquad (5)$$

where $\tau_\lambda(CH_4) + \tau_\lambda(C_2H_2)$ is the total hydrocarbon slant optical depth above the peak of the Chapman layer from both CH_4 and C_2H_2. We show in Figure 10 the transmission function wavelength dependencies for the analytic approximations, (4) and (5), which are compared to the model atmosphere result with a Chapman layer peak at 370 km [*Gladstone and Skinner*, 1989]. The difference between the analytic approximation equation (5) and the model atmosphere calculation is not significant and is caused by the grid spacing. A displacement of the Chapman layer peak by a few kilometers can bring the transmission functions for the analytic model and the model atmosphere calculation of Gladstone and Skinner into close agreement. The two analytic models differ by nearly a factor of 2 in the estimated CH_4 column densities encountered in a deep Galileo aurora. The models have enough free parameters that it is not possible to choose between the two for simulating the data. From this point on, we choose to show only the representation from (4), except for one case for the UVS to illustrate the effects of C_2H_2.

Fig 10

All of the UVS observations considered in this analysis occurred on the darkside or within a few degrees of the dawn terminator. Since there is no measurable solar albedo in the FUV, there is no added constant of solar reflectance, unlike HUT or IUE auroral dayside spectra.

The H_2 emission rate g_λ–factor for an emission line ($J' \rightarrow J''$, $v' \rightarrow v''$, Ryd$\rightarrow$X) following electron impact excitation from a rotational level ($J_i \rightarrow J'$, $v_i \rightarrow v'$, $X \rightarrow$Ryd) in the ground state to rotational level J' is given by

$$g_\lambda(J' \rightarrow J'', v' \rightarrow v'') = F_e(\varepsilon,z)\omega_\lambda(J' \rightarrow J'', v' \rightarrow v'')\,x$$

$$\eta(z, H_2) \sum_{v_i, J_i = J'\pm 1} f(v_i, J_i, T(z))\,Q(\varepsilon, v_i, v'; J_i, J') \qquad (6)$$

where $F_s(\varepsilon,z)$ is the secondary electron distribution at altitude z as a function of energy ε; $Q(\varepsilon)$ is the excitation cross section for rotational level v', J' from initial level v_i, J_i; p is the fraction of the population of H_2 molecules in level v_i, J_i at temperature $T(z)$; and ω_λ is the emission branching ratio. At the resolution of the Galileo UVS and EUVS, where tens of rotational lines are summed, we have verified that the branching ratios are adequately described by using the *Allison and Dalgarno* [1970] oscillator strengths and Honl-London factors for the calculation of transition probabilities. The more accurate rotational line oscillator strengths from *Abgrall et al.* [1993a,b] are necessary for the high-resolution capability of HST, where perturbed rotational lines are resolved [*Liu and Dalgarno*, 1996]. However, the more accurate excitation cross sections of the Rydberg bands, recently measured at high resolution, are required to produce synthetic spectra [*Liu et al.*, 1998]. These excitation cross sections are given in Table 2 for the B, B', C, D' states of H_2. The B state cascade cross section value at 100 eV [*Ajello et al.*, 1988] is stated for the combined cascade cross sections of the E, $F \rightarrow B$ and $G,K \rightarrow B$ and $H \rightarrow B$ transitions [*James et al.*, this issue]. However, the cascade cross section at low energy (ε ~20 eV) is reduced by 1/2 for the modeling process of this paper from earlier estimates [*Shemansky et al.*, 1985; *Ajello et al.*, 1982, 1988]. The recent modeling of high-resolution FUV laboratory spectra at 20 eV indicates the cascade cross section is roughly 1/2 of the earlier estimates (X. Liu, private communication, 1998). This cross section is extremely important in interpreting FUV spectra, since the model spectral distribution and color ratio (1) is affected by this cross section. Since the EUVS spectra are optically thick with a measured wavelength threshold of 880 Å, we neglect in the model the emissions of the n=4 Rydberg series, $B'\,{}^1\Sigma_u^+$ and $D'\,{}^1\Pi_u$, to the ground state, which radiate primarily from 800-900 Å [*Ajello et al.*, 1984; *Liu et al.*, 1995].

In order to calculate the g factor, it is important to quantify the flux of secondary electrons from electron impact ionization of H_2. We show in Figure 11 the secondary electron distribution, measured by *Opal et al.* [1971]. The secondary electron energy spectrum is largely independent of primary impact energy. This secondary electron flux was used in the model calculations for exciting the H_2 aurora. The secondary electron flux can be parameterized by the sum of four Maxwellians:

$$F_s = \sum_{n=1}^{4} C_n \Phi_n(T_n) \qquad (7)$$

where C_n are constants and Φ_n are Maxwellians at electron temperature T_n. The constants C_n and corresponding temperatures are given in Figure 11. We have compared the Opal electron production spectrum in the energy range 10-1000 eV against the steady state distribution for electron precipitation in the Jupiter atmosphere [*Singhal et al.*, 1992]. The agreement in this range is excellent.

Fig 11

By considering all electrons from 10 to 1000 eV, we accurately model the effect upon the g factor of cross section variation with energy. The preponderance of low-energy electrons in the distribution function enhances the effect of the (E,F), (G,K) (double minimum potential functions) and $H \rightarrow B$ cascade cross section (optically forbidden excitation processes) contribution in the 1270-1600 Å spectral region, relative to a monoenergetic 100 eV electron distribution. We show in Figure 12 the importance of the electron energy distribution to the model FUV spectrum. In addition, we overplot the 100 eV preflight electron beam calibration spectrum, together with a 100 eV model. The differences between the Maxwellian secondary electrons and the monenergetic generated electron impact induced fluorescence spectrum are as large as 50% in the FUV for wavelengths above 1270 Å. These two distributions represent the extremes of a "cold" and "hot" electron distribution function, respectively. The spectra in Figure 12 represent the extreme of effects on the FUV spectrum by the secondary electron distribution for the same gas temperature. The enhancement of low-energy electrons in the Maxwellian distribution serves to pump the Lyman bands relative to the Werner bands. The intensity of the v' ' progression with v' = 0 of the B state is increased relative to progressions from higher vibrational levels. The use of the 100 eV monoenergetic "hot" electron distribution in analyzing Jupiter aurora spectra will lead to smaller CH_4 column abundances than the cold Maxwellian distribution. The actual Jupiter electron distribution at any longitude in the auroral oval may be variable with altitude and time between these two extremes.

Fig 12

The final consideration in the modeling is an understanding of the atmospheric distribution of H_2 and CH_4, the dominant hydrocarbon in the nonauroral atmosphere. C_2H_2, the next most abundant hydrocarbon, has a mixing ratio in the peak auroral region altitudes (250-400 km) of 10^{-1} to 10^{-2} of CH_4, albeit for the nonauroral atmosphere [*Gladstone et al.*, 1996]. The actual mixing ratios of the hydrocarbons in the auroral atmosphere are not known. *Livengood et al.* [1990] give arguments for both the net upward and downward motion of the semi-infinite photochemical layer of hydrocarbons by considering the added effects of vertical transport and electron impact dissociation. They estimate an upward or downward motion of the homopause by 1 or 2 scale heights, H= 30 km for 200 K. With this consideration, we show in Figure 13 the large scale, estimated distribution of the important atmospheric constituents in the auroral atmosphere, based on the Galileo probe results of the equatorial region for H_2 [*Seiff et al.*, 1996, 1997] and CH_4 from photochemical models from before the Galileo probe data [*Gladstone et al.*, 1996]. The effect of the increase of the acceleration of gravity at 60° N is the primary effect that has been used to modify the Galileo probe results. We have not modified the temperature distribution of the Galileo probe. Beneath the homopause the mixing ratio of CH_4 is 2×10^{-3}. The lowest layer in the model for the EUV and the highest layer for the FUV, near the homopause, are the only layers whose

Fig 13

emissions may be affected by CH_4 absorption in the modeling process. We mark in Figure 13 four important altitudes above the 1 bar reference level, corresponding to the column density locations of 10^{16} cm^{-2} (0.0001 μbar) at 1240 km, 10^{18} cm^{-2} (0.006 μbar) at 660 km, 10^{20} cm^{-2} (0.4 μbar) at 340 km, and 10^{21} cm^{-2} at 265 km (3 μbar) (pressures). The pressures and altitudes for each layer can vary significantly, depending on the temperature structure in the auroral zone. The auroral temperatures are very uncertain and time variable with effects from joule heating and H_3^+ cooling [*Kim et al.*, 1992].

We address the modeling problem, realizing that more than one atmospheric layer will contribute to the emergent UV spectrum. We indicate schematically in Figure 13 the layer that contributes the most emission to four wavelength intervals in the EUV and FUV found from this study with the understanding that the FUV layer may be very extended in the homosphere. The FUV layer can be extended, since slant optical depth unity varies by a factor of 10 or more from 1250 Å, where CH_4 opacity dominates to 1600 Å, where C_2H_2 and other hydrocarbon/aerosol opacity is important. The temperatures for these layers in the equatorial region have been measured by the Galileo probe. In the modeling process, we use a temperature of 1000 K for the 10^{16} cm^{-2} layer, 900 K for the 10^{18} cm^{-2} layer, and 600 K for the 10^{20} and 10^{21} cm^{-2} layers, based on the mean line-of-sight rotational temperature from HST analysis of high-resolution FUV spectra [*Liu and Dalgarno*, 1996]. In general, we find the sensitivity to the H_2 gas temperature of the models to be very weak in the 200-600 K range, the extremes of temperatures measured by Galileo probe and HST, respectively, in this region of the stratosphere above 250 km altitude where the auroral FUV emission probably occurs. We will be discussing the various layers in the next section as we model the FUV and EUV spectra.

Atomic H is an important absorber in the atmosphere for wavelengths below 911 Å. We use H/H_2 mixing ratios given by *Shemansky* [1985]. The mixing ratios are 0.021, 0.13, and 0.67 for vertical H_2 column densities of 1×10^{16} cm^{-2}, 3×10^{16} cm^{-2}, and 1×10^{15} cm^{-2}, respectively. The atomic H composition at the present time is highly speculative, since models of the auroral atmosphere are not well established [*Waite et al.*, 1983].

The spectral analysis scales model spectra for a least squares fit to the data. The requirement of the model is to minimize the difference C_λ^{mod} (c/s) - C_λ^{data} (c/s) in the least squares sense, when summed over the number of channels, n:

$$R(4\pi I_{layer1}, 4\pi I_{layer2}, 4\pi I_{layer3}) = 1/n \left\{ \sum_{i=1}^{n} [C_\lambda^{mod}(i) - C_\lambda^{data}(i)]^2 \right\}^{1/2} \quad (8)$$

The functional dependence of the residual R is defined in terms of the emission from each layer. The data analysis is performed for both the UVS and EUVS observations by a convolution of the model line intensities with the

instrument transmission function, taken to have a trapezoidal line profile with a peak half-width of 10% of the instrument FWHM, multiplied by the wavelength sensitivity to determine a model signal intensity in c/s/channel. The FWHM varies slightly over the spectrum by 10%. We then compare the model signal intensity with the data directly. This type of calculation is necessary for the EUVS, rather than trying to model the calibrated data. The instrument sensitivity is not constant over the FWHM of 35 Å. *Shemansky* [1985] and *Broadfoot et al.* [1981] have successfully used this approach for the Jupiter dayglow for the Voyager UVS. The Galileo EUVS, which is the flight spare Voyager UVS, has been modified to have improved radiation shielding, a holographic grating with reduced scatter, a smaller grating constant, and a larger field of view [*Hord et al.*, 1992].

4. Modeling the UVS observations

We have modeled the UVS observations for G1, C3, and E4. The results are shown in Figures 14, 15 and 16. The FUV model spectra have very little dependence on H_2 foreground gas abundance. Electric field modifications of the electron energy spectrum are not considered here. However, the spectra are very sensitive to CH_4 absorption [*Gladstone and Skinner*, 1989; *Durrance et al.*, 1982]. The models have varying amounts of CH_4 slant column densities from 0 to 2 x 10^{17} cm^{-2} with the C_2H_2 abundance maintained at 10^{-1} to 10^{-2} of the CH_4 abundance [*Gladstone and Skinner*, 1989; *Gladstone et al.*, 1996]. The best model fits to the data for the three north observations occur at a column density of 0 - 1.0 x 10^{16} cm^{-2} of CH_4 for both sets of transmission function models. The best model fits to the data for the south observations occur at a column density of 7.5 ±2.5 x 10^{16} cm^{-2} for G1 and C3 and near 0 cm^{-2} for E4. The sampled latitudes and longitudes for G1, C3, and E4 north were within 35° of one another. The FOV of the UVS is 0.1° x 1.0°. On the sky the arc length of the aurora that is observed is about 6000 km and ensures a range of distinct regions are observed in each case. *Ballester et al.* [1996] have measured small-scale aurora structures of 3300 km arc length. The UVS north aurora were all observed in the IUE enhanced emission region fixed around 180-210° [*Ballester et al.*, 1996; *Gladstone and Skinner*, 1989]. We have sampled too few points in these observations to make any statement on morphology. We consider in more detail the energetics of the aurora and the location of the homopause by comparison with the EUVS.

Most of the UV emission that escapes the atmosphere takes place in the Lyman bands of H_2. The Lyman bands ($B \rightarrow X$) are spread out over 35 upper state vibrational levels connected to 14 lower state vibrational levels as well as the Lyman continuum. The Lyman band system constitutes ~10,000 rotational lines at ~600 K. At an H_2 column density of 10^{20} cm^{-2} the line center optical depths of the Rydberg resonance bands (v',0) below 1110 Å are saturated. At this column density, self-absorption from v''=1 is also significant. High auroral temperatures of 1000 K can even

bring about self-absorption from v''=2. The upper wavelength limit for self-absorption by v''=1 is 1160 Å and by v''=2 is 1230 Å. For the latter case, Lyman α fluorescence would affect the spectra considerably. The self-absorption manifests itself in the EUVS spectrum only. The three strong Rydberg transitions (*C*, *B'*, and *D*) have all their emission in the EUV below 1300 Å and are greatly attenuated in the radiative transport through the Jupiter atmosphere, both by self-absorption and hydrocarbon absorption. The spectral data from the EUV and FUV observations will be compared for the first time to models to demonstrate self-consistency can be achieved.

The results for the UVS analysis are given in Table 3. In detail, the model for the G1 observations for the north indicate an emergent Rydberg band (800-1700 Å) surface brightness of 529 kR. The modeled surface brightness can be compared to the measured surface brightness of 290 kR, integrated over the wavelength range of 1140-1625 Å. In addition, 70 kR is attributed to H Lyman α, not included in the H_2 band emission rate. The models for the G1 observations in the north are shown in Figures 14a and 14c for the transmission function models described by (4) and (5). The best fit models for both cases indicate a column density of CH_4 of about 1 x 10^{16} cm^{-2} The two models differ in the amount of C_2H_2, where we have used a mixing ratio of 10^{-2} of CH_4 for Figure 14a and 10^{-1} of CH_4 for Figure 14c. The effects of the differing amounts of C_2H_2 to the FUV spectrum occur at wavelengths of strong absorption at 1340, 1440, 1480, and 1520 Å. A value of 10^{-1} of the CH_4 abundance for the C_2H_2 abundance seems to cause too much absorption in the deep C_2H_2 bands, whereas the 10^{-2} mixing ratio shown in Figure 14a is not enough. The sensitivity to measuring CH_4 begins at a slant column density of 1 x 10^{16} cm^{-2}. At this column density the optical depth is about 0.15 near 1250 Å.

Fig 14a

Additional auroral modeling parameters are given in Table 3. Table 3 indicates that prior to transmission through the overlying atmosphere, the surface brightness for G1 north at the source region is 941 kR from the Rydberg bands. We assume a 10% conversion efficiency of input energy to UV radiated power. The energy input deposition rate is 151 ergs/cm^2/s. The auroral source is assumed to be 2000 km wide and to fill the 0.1° width of the UVS slit. The observed count rate for G1 north requires a secondary electron flux of 8.2 x 10^8 electrons/cm^2/s for a single-layer column density of 1 x 10^{20} cm^{-2} (~350 km altitude referenced to 1 bar). The radiated power observed in the aurora is similar to HST measurements of an intense FUV aurora [*Ballester et al.*, 1996]. The root-mean-square (RMS) uncertainty of the 1 x 10^{16} cm^{-2} CH_4 column density model to the data is 38% for Figure 14a. The channels containing Lyman α were not considered in the RMS calculation. The largest discrepancy occurs in the 1300 - 1400 Å region and can be accommodated by the simple one-layer model of (4) or (5) by including a "warmer" electron distribution than the Opal distribution.

Table 3

The comparison of the model and data for G1 south is shown in Figure 14c. The model results for the G1 aurora for

Fig 14c

the south listed in Table 3 show a radiated surface brightness of 593 kR in the Rydberg bands at the top of the atmosphere. The measured surface brightness is 541 kR at the spacecraft in the UVS wavelength range and 150 kR in H Lyman α. The secondary electron flux required for this brightness is 1.7 x 10^9 electrons/cm^2/s for a column density of 1 x 10^{20} cm^{-2}. The south aurora is a factor of 5 deeper in the CH_4 slant column density than the north. We find Figure 14b, which uses the transmission function of (4), indicates a best fit of 5 x 10^{16} cm^{-2} for the CH_4 column density, while the transmission function of (5) gives a best fit of 7 x 10^{16} cm^{-2} for the CH_4 column density. It is not possible to compute a meaningful RMS uncertainty, since it is not possible to model the Jupiter spectrum in the wavelength range of 1300-1500 Å. The uncertainties in the *E,F* and *G,K* and *H* cascade cross sections or the electron energy distribution could not account for this large deficit in the one-layer model. As we have noted, the model in the same spectral region in the north is also somewhat stronger than the observation in the 1300-1500 Å wavelength range. The μ factors for the observation are given in Table 1 and are not much different from those for the north. The major result of the analysis of G1 south is the failure of the simple one-layer model to describe deep aurora. We can interpret this effect to indicate the presence of additional absorbers and additional layers. A more realistic atmospheric model of the primary absorbers altitude distribution is required to explain the FUV spectrum.

Fig 14b

To further explore the "extra" absorbers in the G1 south spectrum, we make use of the auroral atmosphere treatment of *Gladstone and Skinner* (G & S) [1989], including Chapman profiles of the auroral emission rate in the H_2 bands, $V(z)$. $V(z)$ can be written

$$V(z) = k\,N(z)\exp[-N(z)/N(z_e)] \qquad (9)$$

where k is a constant of proportionality, $N(z)$ is the total number density at altitude z, and z_e is the altitude of the Chapman layer peak volume emission rate. The original G & S model atmosphere included equatorial photochemical altitude profiles of just two hydrocarbon absorbers, C_2H_2 and CH_4. Their work found IUE FUV spectra could be fit with these two absorbers. However, the recent work by *Gladstone et al.* [1996] plots altitude profiles at 60° polar latitudes for six absorbers: CH_4, C_2H_2, C_2H_4, C_2H_6, C_3H_8, and C_4H_{10}. The altitude distributions derived by *Gladstone et al.*[1996] did not make use of the Galileo probe results, and altitudes in this discussion based on these profiles will need revision.

The G & S transmission function (Figure 10) differs from the analytic functions in the sense that the FUV transmission is increased in spectral regions (1100 - 1300 Å) where the absorption is largest. This is the effect that is needed to explain the deep aurora, like G1 south. The mean transmission function is defined

$$Tr_{mean}(\lambda) = \int V(z)\exp[-\tau_\lambda^{vert}(z)/\mu]\,dz \,/\, \int V(z)\,dz \qquad (10)$$

where τ_λ^{max} is the total vertical optical depth and μ is the cosine of the emission angle. For this analysis, we use the *Opal et al.* [1971] secondary electron function to generate the FUV fluorescence spectrum, without any overlying hydrocarbon absorption, as the estimate of the relative spectral intensity of the source emission region. A typical thin emission spectrum is shown in Figure 12. For the G1 south aurora data, the use of the new transmission function with the six absorbers (CH_4, C_2H_2, C_2H_4, C_2H_6, C_3H_8, and C_4H_{10}) provides improved agreement with the data, compared to models using the analytic expressions of (4) and (5) shown in Figure 10. We varied z_o in the Chapman profile, which in turn, varied the mean transmission function, until we minimized the RMS deviation between the G1 south data and the G1 south model, which is the product of the mean transmission function and the source spectrum. We show in Figures 14d-14h the results of the analysis. Figures 14d and 14e show the absorption cross sections for the six absorbers used to calculate the total optical depth. Figure 14f shows the mean transmission. Figure 14g compares the model and the data and gives the RMS fit. For G1 south, we find an RMS fit of 1.44%. We show in Figure 14h the altitude of the volume emission rate and the altitude profile of the principal constituents. The peak in the Chapman function occurs at 358 km. We also list the Chapman layer column densities for each atmospheric component and the total atmospheric density. The slant column densities of CH_4 and C_2H_2 for G1 south by this technique are 8×10^{16} cm^{-2} and 5×10^{15} cm^{-2}. The slant column densities are nearly the same values found from the analytic transmission functions of (4) and (5). Although a single-layer model cannot fit the spectra from deep aurora, it appears to be a legitimate means of obtaining the CH_4 abundances from the color ratio of (1). A similar analysis for G1 north gives a Chapman layer peak of 405 km. In order to model deep aurora, the atmosphere is better approximated by at least two layers or multi-layers, as above, with (1) a topside diffusive separation layer above the homopause, where the only emitters and absorbers are H and H_2, and (2) a layer of mixed H_2 and hydrocarbons.

Fig 14 d-h

A major result of this analysis is confirmation of the IUE result that C_2H_2 is present above the auroral emissions. This is particularly clear in the fit to the strong absorption band near 1520 Å. Are additional absorbers actually present in the aurora? Photochemical models of Jupiter predict C_2H_6 to be present in a similar amount to C_2H_2. We conclude that the data are also consistent with the presence of C_2H_6 above the aurora. The longer wavelength data absorption edge of C_2H_6 (above 1550 Å) compared to CH_4 helps to minimize systematic offsets between data and model from 1400-1500 Å. The C_2H_6 absorption edge below about 1550 Å serves to improve model fits to Jupiter's reflection spectrum from 1500 to 1740 Å [*Gladstone* and *Yung*, 1983). As shown in Figure 14g, the absorption edge occurs at even longer wavelengths in C_3H_8 and C_4H_{10}. Use of a modern photochemical model with six hydrocarbon absorbers does improve the fits to the spectrum, although the identifications may not be unique. Other aerosols or

Fig 14 g

hydrocarbons may also produce continuous absorption that affects the FUV spectrum. The major remaining discrepancies between the G1 south data and model remain in the 1300-1400 Å range. At this point, the use of a "warmer" electron distribution and a more accurate *E,F* cross section value would probably reduce these remaining residual differences.

The model for the C3 observations for the north indicates a radiated surface brightness of 338 kR. We show the model fits in Figures 15a and 15b. In the north for C3 the best fit occurs for a column density of 1 x 10^{16} cm^{-2} for the CH_4 column density for both transmission function models considered. The secondary electron flux required for this brightness is 5.3 x 10^{8} electrons/cm^2/s for a column density of 1 x 10^{20} cm^{-2}. The RMS uncertainty is about 65% in Figure 15a. The models in Figure 15b show a best fit for the C3 south aurora of 5 x 10^{16} cm^{-2} for the CH_4 column density and from the model of (5) (not shown) of 1 x 10^{17} cm^{-2} for the CH_4 column density. The models for the south show a radiated surface brightness of 293 kR. The electron flux required for this brightness is 8.3 x 10^{8} electrons/cm^2/s for a column density of 1 x 10^{20} cm^{-2}. Once again the model in the 1300-1500 Å wavelength range seriously overestimates the auroral intensity by a factor of 3. The same kind of Chapman analysis presented for G1 south can be used to explain this discrepancy.

Fig 15

The model for the E4 observations for the north indicates a radiated surface brightness of 460 kR. The models are shown in Figures 16a and 16b. The secondary electron flux required for this brightness is 7.2 x 10^{8} electrons/cm^2/s for a column density of 1 x 10^{20} cm^{-2}. The RMS uncertainty is about 50%. The model for the E4 aurora for the south shows a radiated power of 460 kR. The secondary electron flux required for this brightness is 2.7 x 10^{8} electrons/cm^2/s for a column density of 1 x 10^{20} cm^{-2}. In both E4 south and E4 north the best fit occurs for a CH_4 abundance of near 0 cm^{-2}. The quality of the two fits for wavelengths in the range 1270 - 1400 Å can be improved by including a warmer secondary electron distribution function. For other wavelengths the quality of the fit is excellent. Evidently, very weak and shallow aurorae occurred in both E4 north and south at an altitude near 300- 400 km (at or above the homopause), where the vertical H_2 column density is near 3 x 10^{19} cm^{-2} (see Figure 13). The other UVS aurorae on G1 and C3 probably occurred over a more extensive altitude range from 250 to 400 km, where the CH_4 column abundance varies between 1 and 10 x 10^{16} cm^{-2} [*Gladstone et al.*, 1996]. A higher primary energy is required for the deeper penetration.

Fig 16

5. Modeling the EUVS observations

The EUVS data are of sufficient quality to perform the first extensive wavelength modeling in the spectral range of 800-1200 Å. The models of the EUVS data are sensitive to (1) the H_2 gas temperature which controls the number of levels participating in the absorption process, (2) the H_2 column abundance which determines the amount of self-

absorption, and (3) absorption by the CH_4 column. We begin the analysis using the result for the CH_4 column abundances from the previous section for UVS. The model analysis of the EUVS observations is performed using a multiple linear regression technique, involving emission from two or three atmospheric layers [*Bevington*, 1969]. The emergent radiation was fit to the observed data. The amount of contribution from each layer was the fitting parameter. The final model spectrum is a linear sum of the emission from each layer.

We show in Figure 17 the first attempt at modeling the G1 aurora. The figure shows the southern aurora modeled with a 5 x 10^{16} cm^{-2} CH_4 slant column density, which is the mean column abundance indicated by the UVS. The model in Figure 17 uses a two-layer model with a temperature of 600 K for the 1 x 10^{20} cm^{-2} layer and 900 K for the 1 x 10^{18} cm^{-2} layer. The interplanetary H Lyman α line profile serves as the emission model for analyzing the Jupiter H Lyman α line in the EUVS spectra but is not used to yield any physical parameters of the aurora. This observed emission line is simply used in the linear regression analysis along with the model H_2 bands. There are two problems with the two-layer model. First, the output power from the Rydberg bands and the Lyman bands is a factor of 10 below the corresponding intensities from the UVS. Second, the model structures do not match the data structures at 1030 and 1120 Å. The RMS fit is not very satisfactory. In order to match the UVS power from the aurora for the Rydberg bands the temperature of the gas was increased in order to augment the Lyman band output relative to the Werner bands and the high (B', D) Rydberg bands. As the gas temperature increases, the self-absorption in the Rydberg bands becomes more significant. At 3000 K it is possible to match the UVS and EUVS power outputs for all the orbits. We show in Figure 18 the C3 south observation, which occurred at the same time as the C3 UVS observation. The two instruments are boresighted as shown in Plate 1a. The match with the UVS intensity of 300 kR is perfect. However, the RMS fit is not satisfactory, and the required gas temperature is too large to explain the rotational line structure observed by HST. HST has measured the auroral temperatures many times to be near 500 K [*Liu and Dalgarno*, 1996]. This temperature result from HST appears to be stable over the several FUV spectra surveyed.

Fig 17

Fig 18

The one remaining variable is the hydrocarbon abundance. We can simulate an increase in the hydrocarbon abundance by allowing the CH_4 column density to rise beyond the values measured by the UVS in the lowest layer (H_2 ~ 1 x 10^{20} cm^{-2}). The justification for this increase follows from the probable UVS identification of additional hydrocarbon absorption in the 1300-1500 Å range from additional layers. In addition, *Pryor* [1989] has shown the presence of high-altitude complex hydrocarbon absorbers in Jovian auroral zones from Voyager photopolarimeter observations in the UV, which exhibited increased darkening at the poles, with greatest darkening contrast in the south. We show in Figures 19a and 19b the results for G1 for the north with 2 x 10^{17} cm^{-2} CH_4 slant column density for the trans-

mission function model of (4). A nearly identical fit is found for 5×10^{17} cm^{-2} CH_4 slant column density for the transmission function model of (5). We summarize the model Rydberg band surface brightness in Table 3 for the two column abundances of CH_4 of 1×10^{17} cm^{-2} and 2×10^{17} cm^{-2}. The change of a factor of 2 in column abundance leads to a factor of 8 variation in surface brightness. Most of the emission is in the FUV and is unobserved by the EUVS. The best fit surface brightness for the EUVS to match the UVS occurs about halfway between the two column abundance values at about 1.5×10^{17} cm^{-2}. The EUVS models are not dependent on the C_2H_2 slant column density, since the CH_4 absorption cross sections are about twice as large in the 800-1000 Å wavelength range. We have input to the model codes the same C_2H_2 slant column densities as in the UVS modeling, relative to CH_4 column density.

The quality of the RMS fit shown in Figure 19 is excellent in G1 north for both sets of transmission function models. The layer contributing 98.3% of the radiated intensity is the third layer (1×10^{20} cm^{-2} slant column density), since most of the emission takes place in the FUV in the Lyman bands. Yet the second layer (1×10^{18} cm^{-2} slant column density) contributes most of the short-wavelength EUV 880-1100 Å radiation. In total, the second layer contributes 1.4% of the emergent intensity. The results for the G1 south aurora are similar (Figure 20). There is also a measurable contribution from the first layer (1×10^{16} cm^{-2} slant column density) in the vicinity of 900 Å; although it contributes less than 0.3% of the output power in the H_2 bands. The shortest wavelength EUV radiation arises from very high in the atmosphere from an altitude of near 1300 km above the 1 bar level. The various observed spectral structures are adequately explained by the individual spectra from each layer. Self-absorption and hydrocarbon absorption are equally important in understanding the EUV aurora spectra from Jupiter. The deep layer (layer 3) is responsible for the peak at 1150 Å, and layer 2 produces most of the broad peak near 1020 Å. Most of the peak near 1020 Å arises from H_2 bands rather than H Lyman β. The emission cross section of H Lyman β from dissociative excitation of H_2 is about 4% of the emission cross section of H Lyman α from dissociative excitation of H_2 [*Ajello et al.*, 1996).

The C3 south observation depicted in Plate 1a is shown in Figure 21 and is simultaneous with UVS observation of C3 south. The model employs a column density of CH_4 of 2×10^{17} cm^{-2}. This particular model produces a surface brightness of about 1 MR and is listed in Table 3. The actual Rydberg band surface brightness should be near 292 kR, the UVS value. Table 3 shows this value can be attained for a column density of CH_4 between 1×10^{17} cm^{-2} and 2×10^{17} cm^{-2}. We show in Figure 22 the results for the E4 north, which is simultaneous with the UVS E4 north. The modeling results for surface brightnesses are given in Table 3.

The statistics of the EUVS observations can be improved by summing all three observations in the north and the south. We plot in Figure 23 the model fit to the summed

Fig 19

Fig 20

Fig 21

Fig 22

Fig 23

spectrum for a column abundance of CH_4 of 2 x 10^{17} cm^{-2}. The point is to clearly identify the real spectral features in the data and show the good agreement in spectral structure between the data and model.

6. Comparison of UVS observations to HST

The HST GHRS obtained a low-resolution spectrum of the southern Jupiter aurora at the same time as the G2 observations. We show in Figure 24 a calibrated GHRS spectrum and two calibrated UVS spectra normalized at 1610 Å. The two UVS aurora spectra are G1 and E4 south. We have modeled these two spectra to obtain CH_4 column densities of 5 to 7 x 10^{16} cm^{-2} and 0 cm^{-2}, respectively. The HST spectrum and the UVS spectra appear to be well calibrated to one another. Indeed, the intensity for this particular HST spectrum is about 1 MR for a 2000 km wide source. Analysis of the HST spectrum by the same techniques employed here would yield a CH_4 column abundance midway between the abundances found for the two UVS spectra.

Fig 24

7. Discussion

We have presented an analysis of near-simultaneous EUV/FUV observations of the Jupiter aurorae by the Galileo EUVS and UVS. Consistency was achieved between the analysis of the two data sets in terms of the Rydberg band energy outputs at the top of the atmosphere. Auroral sources need to be modeled over a range of a altitudes. For the UVS observations presented here the FUV emission from wavelengths below 1400 Å could be a component of the aurora from above the homopause (~300 - 400 km altitude). For aurorae arising deep in the atmosphere, the wavelengths near 1600 Å can arise partially from regions up to one or two scale heights deeper in the stratosphere [*Gladstone et al.*, 1996; *Gladstone and Skinner*, 1989] near 250 - 300 km altitude. The scale height of the auroral atmosphere at 600 K is 90 km. For deep aurora the model must include at least two layers and hydrocarbons or aerosols in addition to CH_4 : (1) an upper layer of emission from an atmosphere of H_2 and H located above the homopause and (2) a lower layer containing hydrocarbons. The details of the FUV spectra can be fit with an electron energy distribution that is variable with time and altitude.

The *Opal et al.* [1971] distribution generates an electron impact induced fluorescence spectrum that fits most of the spectral structure in the FUV. We show in Figure 25 an FUV model based on a warm 27 eV electron energy distribution exciting an H_2 gas with an elevated vibrational temperature of 1400 K. The model provides a better fit of some of the electron impact induced fluorescence spectra in the wavelength range from 1270 to 1400 Å for shallow aurorae, such as occurred on E4. Electric field accelerations could modify the Opal distribution. Note the different structure in the wavelength region longward of 1270 Å for the warm and cold distributions. Until there is a high-resolution study of the $E,F \rightarrow B$ cascade cross-section dependence at low impact

Fig 25

energies (12-50 eV), the spectral modeling in the range 1270-1400 Å will remain uncertain. In addition, the high-resolution structure of the C_2H_2 absorption cross section is critical in building an accurate transmission model for the H_2 Lyman band rotational line spectrum. This study shows a simple one-layer mixed atmosphere does not work as a basis for a model for either the Galileo UVS or EUVS observations. A statement can now be made of the Jupiter auroral parameters that influence the multilayer modeling of spectra. The parameters to be considered for future work are (1) location of homopause, (2) altitude distribution of hydrocarbons and aerosols, (3) secondary electron distribution with altitude, (4) H_2 vibrational temperatures, and (5) multienergy primary particle deposition into the aurora, which can deposit significant amounts of energy above the homopause as well as deep in the stratosphere, causing multi-Chapman layers.

The slant column densities of CH_4, the principal absorber, required to match the six UVS auroral observations lie between 0 cm^{-2} and 10 x 10^{16} cm^{-2} (Table 3). The cosine of the emission angle for these observations is close to 0.3 (Table 1). The vertical column densities of CH_4 are in the range 0 cm^{-2} to 3 x 10^{16} cm^{-2}. The EUVS and UVS observations in the wavelength range of 1000-1300 Å are consistent with vertical column densities of H_2 of 3 x 10^{19} cm^{-2} to 1 x10^{21} cm^{-2}. The lower limit is based on the smallest column density required to fit the EUVS data and the high-altitude aurorae measured by the UVS, which requires the emission to take place near the homopause. The upper limit is estimated, based on the location of the visible aurora at an altitude of 240 km (A. Ingersoll *et al.*, submitted paper, 1998), since the EUVS models are not sensitive to column densities in excess of 1 x 10^{20} cm^{-2}. The lowest layer in the EUVS modeling occurs at an altitude range of 300 to 400 km above the 1 bar level. Higher atmospheric layers produce the observed EUV radiation from 880 to 1000 Å.

These abundances provide the best comparison of the auroral ratio of H_2/CH_4 column densities which can be used as a basis for volumetric altitude distributions. Earlier works [*Gladstone and Skinner*, 1989; *Yung et al.*, 1982] have quantified the CH_4 abundance from IUE work. The ratio of H_2/CH_4 column densities at the homopause in the aurora is uncertain and may be variable with values between 10^3 to 10^6. This range includes the equatorial mixing ratio of 5 x 10^4 [*Gladstone et al.*, 1996]. Further modeling will determine the auroral ratio more exactly.

The combined EUVS and UVS observations show that the aurora is produced over a wide range of altitudes. For a single mean primary energy the emission layer resembles a Chapman layer, whose emission profile is distributed with an *e*-folding distance of an atmospheric scale height [*Gladstone and Skinner*, 1989]. The mean primary electron energies required to penetrate to the deep EUV/FUV layers are shown in Figure 26 with a comparison to previous estimates from *Cravens et al.* [1975], *Gladstone and Skinner* [1989] and *Koral and Cohen* [1965]. The cross sections for electron energy loss are from *Northcliffe and Schilling* [1970]. The primary energies required to penetrate to the

Fig 26

deep 10^{19} - 10^{21} cm^{-2} layers are in the range 10 - 50 keV. However, a more general model of the emission layers is required with a knowledge of the distribution function of primaries [*Gerard and Singh*, 1982]. Perhaps the joint fields and particles and remote sensing observations of the ~30 R_J aurora in the C3 and G8 orbits will help quantify the primary particle distribution entering the loss cone.

We can estimate the energy input to the aurora required to produce the observations described in this paper. The modeling results are summarized in Table 3. We indicate the emission rate at the top of the atmosphere in the Rydberg bands for both instruments as predicted by the model. For the UVS the surface brightness emission rates at the top of the atmosphere from both the model and the data are in close agreement, since most of the output flux is in the Lyman bands. The surface brightnesses described in Table 3 for the 2000 km wide model source exceed 100 kR for all observations. We use the 10% efficiency [*Waite et al.*, 1983] for converting energy deposition from a primary electron flux above 1 keV into the source region to emission from the Rydberg bands. The energy deposition fluxes are shown in Table 3. For the brightest aurora on G1 south the energy flux to excite the Rydberg bands is about 30 ergs/cm^{2}s. The total energy flux to all processes at the source region is 307 ergs/cm^{2}s.

There may be multiple ways to produce a given transmission function from models and match the energy output with the EUV. A variety of transmission functions have been studied in this paper (Figures 10 and 14). Future work will include extending our EUV/FUV models to include many-layer atmospheres with more realistic chemical distributions and auroral energy deposition, to produce new transmission functions that may clarify the role of additional absorbers, which may be particularly important in the EUV.

We summarize the results from this analysis for the EUVS in Section 7.1, and similarly, we summarize results for the UVS in Section 7.2. This analysis of the combined EUVS/UVS data sets will be examined in more detail to understand the model variables of temperature, secondary electron distribution functions, and high-resolution effects of absorption by other hydrocarbons.

7.1. Major EUVS Results

Data Results. Three EUV spectral images of Jupiter aurora and dayglow; Spectra are highly variable with cutoff near 880 Å.

Modeling Results. Model development with H_2 self-absorption, latest H_2 excitation cross sections, hydrocarbon absorption and *Opal et al.* [1971] secondary electron distribution (0 - 1 keV); Peak energy deposition occurs at H_2 slant column density ~ 3 x 10^{19} to 10^{21} cm^{-2}; EUV aurora are produced over a range of altitudes from 1 x 10^{16} cm^{-2} to 1 x 10^{21} cm^{-2} H_2 slant column density (250-1300 km altitude) with the bulk of the integrated intensity (>99%) occurring at altitudes from 1 x 10^{18} cm^{-2} to 1x 10^{21} cm^{-2} H_2 slant column density (250-700 km altitude); Primary electron energy 10-

50 keV with energy input to Rydberg bands of ~30-300 ergs/cm^{2}s for a 2000 km wide aurora.

7.2 Major UVS Results

Data Results. Simultaneous (C3 south and E4 north) EUV/UVS auroral imaging and near-simultaneous imaging on other observations; Surface brightness of aurora of Rydberg bands are 100-500 kR with Lyman α surface brightnesses from 50 to 150 kR.

Modeling Results. Aurora are modeled with peak deposition at a slant column density of CH_4 of 0-1x10 ^{16} cm^{-2} in the north and 0-10 x 10^{16} cm^{-2} in the south; Secondary electron distribution function ~ 10^{8-9} e/cm^2/s at 250 - 400 km altitude.

Acknowledgments. The research described in this text was carried out at the Jet Propulsion Laboratory, California Institute of Technology, the University of Colorado, University of Southern California, University of Michigan, and University of Arizona. The work was supported by the Galileo Project and Space Telescope Program Office. J.C. acknowledges grant 5828-01-94A from ST ScI to the University of Michigan. We appreciate careful review of the manuscript by G. R. Gladstone.

References

Abgrall, H., E. Roueff, F. Launay, J.-Y. Roncin, and J.-L. Subtil, Table of the Lyman band system of molecular hydrogen, *Astron. Astrophys. Suppl.*, *101*, 273-321, 1993a.

Abgrall, H., E. Roueff, F. Launay, J.-Y. Roncin, and J.-L. Subtil, Table of the Werner band system of molecular hydrogen, *Astron. Astrophys. Suppl.*, *101*, 323-362, 1993b.

Ajello, J. M., S. K. Srivastava, and Y. L. Yung, Laboratory studies of uv emissions of H_2 by electron impact: The Werner and Lyman band systems, *Phys. Rev. A*, *29*, 636-653, 1982.

Ajello, J. M., D. E. Shemansky, T. L. Kwok, and Y. L. Yung, Studies of extreme-ultraviolet emission from Rydberg series of H_2 by electron impact, *Phys. Rev. A*, *29*, 636-653, 1984.

Ajello, J. M., *et al.*, A simple ultraviolet calibration source with reference spectra and application to the Galileo orbiter ultraviolet spectrometer, *Appl. Opt.*, *27*, 890-914, 1988.

Ajello, J. M., W. R. Pryor, C. A. Barth, C. W. Hord, A. I. F. Stewart, K. E. Simmons, and D. T. Hall, Observations of interplanetary Lyman α with the Galileo ultraviolet spectrometer experiment: Multiple scattering effects at solar maximum, *Astron. Astrophys.*, *289*, 283-303, 1994.

Ajello, J. M., S. M. Ahmed, and X. Liu, Line profile of H Lyman β from dissociative excitation of H_2, *Phys. Rev. A*, *53*, 2303-2308, 1996.

Allison, A. C., and A. Dalgarno, Band oscillator strengths and transition probabilities of the Lyman and Werner systems of H_2, HD and D_2, *At. Data*, *1*, 289-304 , 1970.

Ballester, G., et al., Time-resolved observations of Jupiter's far-ultraviolet aurora, *Science*, *274*, 409-412, 1996.

Bevington, P. R., *Data Reduction and Error Analysis for the Physical Sciences*, pp. 164-186, McGraw-Hill, New York, 1969.

Broadfoot, A. L., B. R. Sandel, D. E. Shemansky, J. C. McConnell, G. R. Smith, J. B. Holberg, S. K. Atreya, T. M. Donahue, D. F. Strobel, and J. L. Bertaux, Overview of the Voyager ultraviolet spectrometry results through Jupiter encounter, *J. Geophys. Res.*, *86*, 8259-8284, 1981.

Clarke, J., T., L. B. Jaffel, A. Vidal-Madjar, G. R. Gladstone, J. H. Waite, R. Prange, J.-C Gerard, J. Ajello, and G. James, Hubble Space Telescope Goddard high-resolution spectrograph H_2 rotational spectra of Jupiter's aurora, *Astrophys.. J.*, *430*, L73-L76, 1994.

Clarke J. T., et al., Far-ultraviolet imaging of Jupiter's aurora and the Io "footprint", *Science*, *274*, 404-409, 1996.

Clarke, J. T., et al.., Hubble Space Telescope imaging of Jupiter's UV aurora during the Galileo orbiter mission, *J. Geophys. Res.*, this issue.

Cravens, T. E., G. A. Victor, and A. Dalgarno, The absorption of energetic electrons by molecular hydrogen gas, *Planet. Space Sci.*, *23*, 1059-1070, 1975.

Durrance, S. T., P. D. Feldman, and H. W. Moos, The spectrum of the Jovian aurora 1150-1700 Å, *Geophys. Res. Lett.*, 9, 652-655, 1982.

Emerich, C., L. B. Jaffel, J. T. Clarke, R. Prange, G. R. Gladstone, J. Sommeria, and G. Ballester, Evidence for supersonic turbulence in the upper atmosphere of Jupiter, *Science*, *273*, 1085-1087, 1996.

Feldman, P. D., M. A. McGrath, H. W. Moos, S. T. Durrance, D. F. Strobel, and A. F. Davidsen, The spectrum of the Jovian dayglow at 3Å resolution with the Hopkins ultraviolet telescope, *Astrophys. J.*, *406*, 279-284, 1993.

Gerard, J. C., and V. Singh, A model of energy deposition and EUV emission in the Jovian and Saturnian atmosphere and implications, *J. Geophys. Res.*, *87*, 4525-4532, 1982.

Gerard, J. C., V. Dols, F. Paresce, and R. Prange, Morphology and time variation of the Jovian far UV spectra: Hubble Space Telescope observations, *J. Geophys. Res.*, *98*, 18,793-18,801, 1993.

Gerard, J. C., D. Grodent, R. Prange, J. H. Waite, G. R. Gladstone, V. Dols, F. Paresce, A. Storrs, L. B. Jaffel, and K. A. Franke, A remarkable event on Jupiter observed in the ultraviolet with the Hubble space telescope, *Science*, *266*, 1675-1678, 1994a.

Gerard, J. C., V. Dols, R. Prange, and F. Paresce, The morphology of the north Jupiter ultraviolet aurora observed with the Hubble space telescope, *Planet. Space Sci.*, *42*, 905-917, 1994b.

Gladstone, G. R., and T. E. Skinner, Spectral analysis of Jovian auroral emissions, in *Time Variable Phenomena in the Jovian System*, edited by M. J. S. Belton, R. A. West and J. Rahe, NASA *Spec. Publ.*, *SP-494*, 221-228, 1989.

Gladstone, G. R. and Y. L. Yung, An analysis of the reflection spectrum of Jupiter from 1550 Å to 1740 Å, *Astrophys. J.*, *266*, 415-424, 1983.

Gladstone, G. R., M. Allen, and Y. L. Yung, Hydrocarbon photochemistry in the upper atmosphere of Jupiter, *Icarus*, *119*, 1-52, 1996.

Harris, W. M., J. T. Clarke, M. A. McGrath, and G. E. Ballester, Analysis of Jovian auroral H Lyα emission (1981-1991), *Icarus*, *123*, 350-365, 1996.

Herbert, F., B. R. Sandel, and A. L. Broadfoot, Observations of the Jovian UV aurora by Voyager, *J. Geophys. Res.*, *92*, 3141-3154, 1987.

Hord, C. W., et al., Galileo ultraviolet spectrometer experiment, *Space Sci. Rev.*, *60*, 503-530, 1992.

James, G. K., J. M. Ajello, and W. Pryor, The MUV-visible spectrum of H_2 excited by electron impact, *J. Geophys. Res.*, this issue.

Kim, Y. H., J. L. Fox, and H. S. Porter, Densities and vibrational distribution of H_3^+ in the Jovian auroral ionosphere, *J. Geophys. Res.*, *97*, 6093-6101, 1992.

Kim, Y. H., J. J Caldwell, and J. L. Fox, High-resolution ultraviolet spectroscopy of Jupiter's aurora with the Hubble space telescope, *Astrophys. J.*, *447*, 906-914, 1995.

Koral, K. F., and A. J. Cohen, Empirical equations for electron backscattering coefficients, *NASA Tech. Note, TN D-2909*, 1965.

Liu, W., and A. Dalgarno, The ultraviolet spectra of the Jovian aurora, *Astrophys. J.*, *467*, 446-453, 1996.

Liu, X., S. M. Ahmed, R. A. Multari, G. K. James, and J. M. Ajello, High-resolution electron impact study of the far ultraviolet emission spectrum of molecular hydrogen, *Astrophys. J. Suppl.*, *101*, 375-399, 1995.

Liu, X., D. E. Shemansky, S. M. Ahmed, G. K. James, and J. M. Ajello, Electron impact excitation and emission cross sections of the H_2 Lyman and Werner systems, *J. Geophys. Res.*, in press, 1998.

Livengood, T. A., D. F. Strobel, and H. W. Moos, Long-term study of longitudinal dependence in primary particle precipitation in the north Jovian aurora, *J. Geophys. Res.*, *95*, 10,375-10,388, 1990.

Morrissey, P. F., P. D. Feldman, J. T. Clarke, B. C. Wolven, D. F. Strobel, S. T. Durrance, and J. T. Trauger, Simultaneous spectroscopy and imaging of the Jovian aurora with the Hopkins ultraviolet telescope and the Hubble space telescope, *Astrophys. J.*, *476*, 918-923, 1997.

Mount, G., E. S. Warden, and H. W. Moos, Photoabsorption cross sections of methane from 1400 to 1850 Å, *Astrophys. J.*, *214*, L47-L49, 1977.

Mount, G., E. S. Ward, and H. W. Moos, Photoabsorption cross sections of methane and ethane from 1380-1600 Å at T = 295 K and T = 200 K, *Astrophys. J.*, *224*, L35-L38, 1978.

Nakayama, T. and K. Watanabe, Absorption and photoionization coefficients of acetylene, propyne and 1-butyne, *J. Chem. Phys.*, *40*, 558-561, 1964.

Northcliffe, L. C., and R. F. Schilling, Range and stopping power tables for heavy ions, *Nucl. Data Tables*, *A7*, 233-463, 1970.

Opal, C. B., W. K. Petersen, and E. .C. Beaty, Measurements of secondary-electron spectra by electron impact ionization of a number of simple gases, *J. Chem. Phys.*, *55*, 4100-4106, 1971.

Prange, R., D. Rego, and J. C. Gerard, Auroral Lyman α and H_2 from the giant planets, 2, Effect of the anisotropy of the precipitating particles on the interpretation of "color ratio", *J. Geophys. Res.*, *100*, 7513-7521, 1995.

Prange, R., S. Maurice, W. M. Harris, D. Rego, and T. Livengood, Comparison of IUE and HST diagnostics of the Jovian Aurorae, *J. Geophys. Res.*, *102*, 9289-9301, 1997a.

Prange, R., D. Rego, L. Pallier, L. B. Jaffel, C. Emerich, J. Ajello, J. T. Clarke, and G. Ballester, Detection of self-reversed Lyman α lines from the Jovian aurorae with the Hubble space telescope, *Astrophys. J.*, *484*, L169-L173, 1997b.

Pryor, W., Auroral ultraviolet darkening on the outer planets, Ph.D. thesis, chap. IV, University of Colo., Boulder, 1989.

Pryor, W., J. M. Ajello, C. A. Barth, C. W. Hord, A. I. F. Stewart, K. E. Simmons, W. E. McClintock, B. R. Sandel, and D. E. Shemansky, The Galileo and Pioneer Venus ultraviolet spectrometer experiments: Solar Lyman α latitude variation at solar maximum from interplanetary Lyman α experiments, *Astrophys. J.*, *394*, 363-377, 1992.

Seiff, A., D. B. Kirk, T. C. D. Knight, J. D. Mihalov, R. C. Blanchard, R. E. Young, G. Schubert, U. von Zahn, G. Lehmacher, F. S. Milos, and J. Wang, Structure of the atmosphere of Jupiter, *Science*, *272*, 844 - 845, 1996.

Seiff, A., D. B. Kirk, T. C. D. Knight, L. A. Young, F. S. Milos, E. Venstatapathy, J. D. Mihalov, R. C. Blanchard, R. E. Young, and G. Schubert, Thermal structure of Jupiter's upper atmosphere derived from the Galileo probe, *Science*, *276*, 102-104, 1997.

Shemansky, D. E., An explanation for the H Lyα longitudinal asymmetry in the equatorial spectrum of Jupiter: An outcrop of paradoxical energy distribution in the exosphere, *J. Geophys. Res.*, *90*, 2673-2694, 1985.

Shemansky, D. E., J. M. Ajello, and D. T. Hall, Electron impact excitation of H_2: Rydberg band systems and the benchmark cross section for H Lyman α, *Astrophys. J.*, *296*, 765-773, 1985.

Singhal, R. P., S. C. Chakravarty, A. Bhardwaj, and B. Prasad, Energetic electron precipitation in Jupiter's upper atmosphere, *J. Geophys. Res.*, *97*, 18,245-18,256, 1992.

Suto, M., and L. C. Lee, Quantitative photoexcitation and fluorescence studies of C_2H_2 in vacuum ultraviolet, *J. Chem. Phys.*, *80*, 4824-4831, 1984.

Trafton, L. M., J. C. Gerard, G. Munhoven, and J. H. Waite, High resolution spectra of Jupiter's northern auroral ultraviolet emission with the Hubble space telescope, *Astrophys. J.*, *421*, 816-827, 1994.

Waite, J. H., T. E. Cravens, J. Kozyra, A. F. Nagy, S. K. Atreya, and R. H. Chen, Electron precipitation and related aeronomy of the Jovian thermosphere and ionosphere, *J. Geophys. Res.*, *88*, 6143-6163, 1983.

Wu, C., W. Robert, T. S. Chien, G. S. Liu, D. L. Judge, and J. J. Caldwell, Photoabsorption and direct dissociation cross sections of C_2H_2 in the 1530-1930 Å region: A temperature dependent study, *J. Chem. Phys.*, *91*, 272-280, 1989.

Yung, Y. L., G. R. Gladstone, K. M. Chang, J. M. Ajello, and S. K. Srivastava, H_2 fluorescence spectrum from 1200 to 1700 Å by electron impact: Laboratory study and application to Jovian aurora, *Astrophys. J. Lett.*, *254*, L65-L69, 1982.

J. Ajello, Jet Propulsion Laboratory, California Institute of Technology, MS 183-601, 4800 Oak Grove Drive, Pasadena, CA 91109. (e-mail: jajello@jpluvs.jpl.nasa.gov)

C. Barth, J. Gebben, C. Hord, W. McClintock, D. Miller, W. Pryor, K. Simmons, and I. Stewart, Laboratory for Atmospheric and Space Physics, University of Colorado, Boulder, CO 80303.

B. Sandel, Lunar and Planetary Laboratory, University of Arizona, Tucson, AZ 85721.

J. Clarke, Space Physics Laboratory, University of Michigan, Ann Arbor, MI 48109.

D. Shemansky, Department of Aerospace Engineering, University of Southern California, Los Angeles, CA 90089.

S. Stephens and K. Tobiska, FDC/Jet Propulsion Laboratory, Pasadena, CA 91109.

(Received September 10, 1997; revised March 4, 1998;
accepted March 9, 1998

[1]Jet Propulsion Laboratory, California Institute of Technology, Pasadena.
[2] Department of Aerospace Engineering, University of Southern California, Los Angeles.
[3] Laboratory for Atmospheric and Space Physics, University of Colorado, Boulder.
[4] Federal Data Corporation, Jet Propulsion Laboratory, Pasadena, California.
[5]Space Physics Research Laboratory, University of Michigan, Ann Arbor.
[6] Lunar and Planetary Laboratory, University of Arizona, Tucson.

Paper number 98JE00832.
0148-0227/98/98JE-00832$09.00.

AJELLO ET AL.: EUV AND FUV OBSERVATIONS OF JUPITER AURORA
AJELLO ET AL.: EUV AND FUV OBSERVATIONS OF JUPITER AURORA
AJELLO ET AL.: EUV AND FUV OBSERVATIONS OF JUPITER AURORA
AJELLO ET AL.: EUV AND FUV OBSERVATIONS OF JUPITER AURORA
AJELLO ET AL.: EUV AND FUV OBSERVATIONS OF JUPITER AURORA
AJELLO ET AL.: EUV AND FUV OBSERVATIONS OF JUPITER AURORA
AJELLO ET AL.: EUV AND FUV OBSERVATIONS OF JUPITER AURORA
AJELLO ET AL.: EUV AND FUV OBSERVATIONS OF JUPITER AURORA
AJELLO ET AL.: EUV AND FUV OBSERVATIONS OF JUPITER AURORA
AJELLO ET AL.: EUV AND FUV OBSERVATIONS OF JUPITER AURORA
AJELLO ET AL.: EUV AND FUV OBSERVATIONS OF JUPITER AURORA
AJELLO ET AL.: EUV AND FUV OBSERVATIONS OF JUPITER AURORA
AJELLO ET AL.: EUV AND FUV OBSERVATIONS OF JUPITER AURORA
AJELLO ET AL.: EUV AND FUV OBSERVATIONS OF JUPITER AURORA

AJELLO ET AL.: EUV AND FUV OBSERVATIONS OF JUPITER AURORA
AJELLO ET AL.: EUV AND FUV OBSERVATIONS OF JUPITER AURORA
AJELLO ET AL.: EUV AND FUV OBSERVATIONS OF JUPITER AURORA
AJELLO ET AL.: EUV AND FUV OBSERVATIONS OF JUPITER AURORA
AJELLO ET AL.: EUV AND FUV OBSERVATIONS OF JUPITER AURORA
AJELLO ET AL.: EUV AND FUV OBSERVATIONS OF JUPITER AURORA
AJELLO ET AL.: EUV AND FUV OBSERVATIONS OF JUPITER AURORA
AJELLO ET AL.: EUV AND FUV OBSERVATIONS OF JUPITER AURORA
AJELLO ET AL.: EUV AND FUV OBSERVATIONS OF JUPITER AURORA

TABLE 1. Summary of EUVS/UVS Near-Simultaneous Observations for the Big Four Orbits

EUVS

Orbit	Day of Year 1996/Observation Mid-Time (DOY/hour min)	Spacecraft Distance, R_J	Start Time (RIMS)	End Time (RIMS)	Duration (RIMS)	Fill Factor, %	MU (mid-time) (mean cosine emission angle)	Latitude, Longitude Mid-Time, degrees
G1 North	172/23^{h}44^m	67.6	3488463	3488866	403	7.7	0.24	58-70N,150-220W
G1 South	172/23^{h}44^m	67.6	3488463	3488866	403	5.3	0.17	76-84S,120-270W
C3 North	304/11^{h}55^m	61.7	3675730	3676179	449	4.0	0.35	65-77N,60-120W
C3 South	304/09^{h}08^m	62.8	3675560	3675759	199	6.8	0.30	70-73S,331-60W
E4 North	347/22^{h}27^m	55.2	3737639	3738000	361	10.2	0.47	57-74N,100-210W
E4 South	348/04^{h}02^m	54.0	3738001	3738300	299	---	none	77S,308W

UVS

Orbit	Day of Year 1996/Observation Mid-Time (DOY/hour min)	Spacecraft Distance, R_J	Start Time (RIMS)	End Time (RIMS)	Duration (RIMS)	Integration Time per channel, s	Fill Factor, %	MU (mid-time) (mean cosine emission angle)	Latitude, Longitude Mid-Time, degrees
G1 North	176/06^{h}08^m	43.0	3493308	3493328	20	1.44	4.1	0.25	53N,185W
G1 South	176/03^{h}36^m	44.1	3493156	3493176	20	1.44	5.8	0.34	71S,23W
C3 North	304/13^{h}41^m	61.2	3675880	3676239	359	29.74	2.7	0.27	67N,216W
C3 South	304/09^{h}09^m	62.2	3675700	3675879	179	9.83	2.6	0.26	69S,57W
E4 North	347/21^{h}55^m	55.3	3737639	3737938	299	12.31	2.9	0.45	67N, 210W
E4 South	348/04^{h}33^m	53.8	3738001	3738362	361	14.87	3.0	0.20	69S, 70W

TABLE 2. Excitation Cross Sections from the $X\ ^1\Sigma_g^+$ Ground State at 100 eV for H_2

State	Cross Section at 300°K, 10^{-17} cm^2	Range of Vibrational Levels Considered
$B\ ^1\Sigma^+_u$ (Direct)	2.62	0-34
$C\ ^1\Pi_u$	2.41	0-13
$B'\ ^1\Sigma^+_u$	0.16	0-7
$D\ ^1\Pi_u$	0.30	0-2(Π^+) 0-14 (Π^-)
$B\ ^1\Sigma^+_u$ (Cascade)	0.29[a]	

[a]Cross sections at low energy are reduced by 1/2 from earlier estimates [*Ajello et al.*, 1982, 1988].

TABLE 3. UVS Modeling Results

Orbit	Model Emission Rate at Top of Atmosphere Rydberg Bands, kR	Observed Emission Rate from Galileo 1160-1725 Å,[a] kR	Observed Emission Rate from Galileo Lyman-α, kR	Model Emission Rate at Source in Atmosphere Rydberg Bands, kR	Energy Input Rate at 2000 km Wide Source Region for 10% UV Efficiency, ergs/cm²s	Slant CH_4 Model Abundance from (4),[b] 10^{16} cm^{-2}	Slant CH_4 Model Abundance from (5),[b] 10^{16} cm^{-2}	Secondary Electron Distribution at Level of 1 x 10^{20} cm^{-2}, 10^8 e/cm²s
*G*1 North	529	290	70	941	1510	1	1	8.2
*G*1 South	593	541	130	1920	3072	5	7	17.0
*C*3 North	338	284	73	601	961	1	1	5.3
*C*3 South	292	130	65	945	1512	5	10	8.3
*E*4 North	460	226	103	818	1312	0	0	7.2
*E*4 South	176	226	86	312	499	0	0	2.7

EUVS Modeling Results for Lowest Layer

Orbit	Emission Rate at Top of Atmosphere with 1 x 10^{17} cm² of CH_4,[c] kR	Emission Rate at Top of Atmosphere with 2 x 10^{17} cm² of CH_4,[c] kR
*G*1 North	129	1025
*G*1 South	162	1238
*C*3 South	128	1057
*E*4 North	120	1140

[a] Without Lyman α
[b] C_2H_2 column abundances are 10^{-1} - 10^{-2} of CH_4.
[c] Most of the emission brightness from the Rydberg band systems occurs in the FUV.

Figure 1. North ecliptic view of the Galileo trajectory during the orbital tour. The spacecraft z axis is nominally pointed in the Earth direction, and the UVS/EUVS can be boresighted to look at the torus and aurora. The orbit numbers are indicated. The white area is the time during which the bulk of the UVS/EUVS observations were planned. Jupiter and the Io torus are available in the region called Io torus period. The 15 R_J radiation constraint is a predicted closest approach distance to operate the instrument. The dark stippled area is the time when the cone angle of Jupiter system is less than 90° and unobservable by the UVS because of spacecraft obstructions.

Plate 1. (a) The geometry for the simultaneous UVS/EUVS observations on C3 (G02C-sequence) at time of crossing the CML of Jupiter. The UVS slit is 1°x 0.1° FWHM rectangular field of view. The EUVS slit is 0.87° x 0.17° triangular field of view. The sector size for the EUVS is 0.87° x 0.4°. (b) The EUVS image of the aurora for G1, C3, and E4 in H Lyα and in the H_2 Rydberg bands. Time is the linear x axis scale as produced by spacecraft motion. The width of each pixel is proportional to the spectral integration time (30 or 60 RIMS), and the height is proportional to the sector size (0.4°) traced out by the spacecraft spin in 21.4 ms.

Figure 2. The EUVS north spectrum for three of the Big Four orbits that obtained spectra: G1, C3, and E4. The units for signals are shown in counts per 0.2 RIM and counts per second. The signal rate magnitudes are close to the total counts received in that orbit. The 1σ error bar for the signal at any wavelength can be found by dividing the count rate by 2.5, which gives the photon events. The square root of the number of photon events is the 1σ error bar. We show the 1σ error bar for the peak signal. The wavelength regions of the Rydberg bands are indicated.

Figure 3. The EUVS south spectrum for three of the Big Four orbits that obtained spectra: G1, C3, and E4. The units for signals are shown in counts per 0.2 RIM and counts per second. The signal rate magnitudes are close to the total counts received in that orbit. The 1σ error bar for the signal at any wavelength can be found by dividing the count rate by 2.5, which gives the photon events. The square root of the number of photon events is the 1σ error bar. We show the 1σ error bar for the peak signal.

Figure 4. The EUVS G1 north spectrum count rate (dotted line) compared to the predicted torus background signal (solid line) for the length of time of the observation. The torus background is obtained from a summation of all the total torus spectra from the Big Four. There is a torus background present in all aurora observations over the approximately 0.2 RIM of the observation. The torus spectrum is subtracted from all EUVS aurora observations by normalizing the estimated torus background signal to the actual auroral observation. The signal rate magnitudes are close to the total counts received in that orbit. The 1σ error bar for the signal at any wavelength can be found by dividing the count rate by 2.5, which gives the photon events. The square root of the number of photon events is the 1σ error bar.

Figure 5. The spectrum of the total of all counts received in G1+ C3+ E4 for (a) the south and (b) the north. The ± 1σ signal statistics are indicated as plus signs.

Figure 6. The UVS spectrum measured simultaneous to or closest in time to the EUVS observations for the north aurora for G1, C3, and E4. The preflight UVS $H_2 + e$ (100 eV) electron impact calibration spectrum is also shown. The 1σ error bar for the signal level in any channel can be calculated as the square root of the plotted count rate times the length of time of the measurement, given in seconds in the plot.

Figure 7. The UVS relative intensity variation as a function of wavelength, normalized to 1580 Å for the northern aurora G1, C3, E4. The preflight electron impact spectrum is also shown.

Figure 8. The UVS spectrum measured simultaneous to or closest in time to the EUVS observations for the south aurora for G1, C3, and E4. The 1σ error bar for the signal level in any channel can be calculated as the square root of the plotted count rate times the length of time of the measurement, given in seconds in the plot.

Figure 9. The UVS relative intensity variation as a function of wavelength, normalized to 1580 Å for the southern aurora G1, C3, and E4. The preflight electron impact spectrum is also shown.

Plate 2. Hubble Space Telescope WFPC 2 image of the G1 south aurora as would be observed by Galileo UVS at time of G1 south observation. The HST observation occurred at day 176 15^h 07^m with a CML of 6°.

Plate 3. Hubble Space Telescope WFPC 2 image of the G1 north aurora as would be observed by Galileo UVS at time of G1 north observation. The HST observation occurred at day 176 18^h 19^m with a CML of 119°. The terminator is shown near 60°W longitude.

Figure 10. Transmission function of hydrocarbon absorbers in the FUV for two analytic models and the model atmosphere of *Gladstone and Skinner* [1989].

Figure 11. Secondary electron flux from $e + H_2$ primary ionization. The data of *Opal et al.*, [1971] and model are shown, along with the model parameters as described in the text. $f(E)$ is the secondary electron distribution.

Figure 12. The Maxwellian model of secondary electrons of Figure 11 are used for the production of an electron impact induced FUV spectrum and a monoenergetic electron impact model spectrum at 100 eV. In addition, we show the preflight laboratory spectrum at 100 eV spectrum.

Figure 13. The low-latitude nonauroral atmosphere based on the Galileo probe results [*Seiff et al.*, 1996; 1997] and the photochemical models for CH_4 [*Gladstone et al.*, 1996].

Figure 14. The G1 UVS FUV observations on day of year (DOY) 176 and model (a) north and (b) south for the hydrocarbon transmission function of (4) and model (c) north for the hydrocarbon transmission function of (5), $1./(1. + \tau)$. In Figures 14d and 14e are the absorption cross section of the six absorbers, CH_4 [*Mount et al.*, 1977], C_2H_2 [*Nakayama and Watanabe*, 1964; *Suto and Lee*, 1984; *Wu et al.*, 1989], C_2H_6 [*Mount et al.*, 1978], C_3H_8, C_2H_4, and C_4H_{10} (see *Gladstone et al.* [1996] for remaining absorption cross section references) to model the G1 south aurora. In Figure 14f is the transmission function derived from the *Gladstone et al.* [1996] model atmosphere. The number density at the Chapman layer peak is 1.2×10^{14} cm^{-3}. We plot the best fit model in Figure 14g of the G1 south observation compared with the G1 south data and the source region H_2 emission spectrum. We plot in Figure 14h the altitude profile of the model atmosphere [*Gladstone et al.*, 1996] and the volume emission rate, $V(cm^{-3}s^{-1})$. The Chapman layer vertical peak column abundances are listed along with the altitude z_p and number density $N(z_p)$.

Figure 15. The C3 UVS FUV observations on DOY 304 and model (a) north and (b) south for the hydrocarbon transmission function of (4).

Figure 16. The E4 UVS FUV observations on DOY 347 and model (a) north and (b) south for the hydrocarbon transmission function of (4).

Figure 17. The G1 EUVS data for the south aurora with a two-layer model atmosphere of 1×10^{16} cm^{-2} of H_2 in layer 1 and 5×10^{16} cm^{-2} of CH_4 and 1×10^{21} cm^{-2} H_2 in layer 2, showing (a) the amount of radiation from each layer at the top of the atmosphere, contributing to the measured signal, based on a linear regression analysis to the data, and (b) the resultant comparison of data and model.

Figure 18. The C3 EUVS data for the south aurora with a two-layer model atmosphere of 1×10^{19} cm^{-2} of H_2 in layer 1 and 5×10^{16} cm^{-2} of CH_4 and 1×10^{21} cm^{-2} of H_2 at a temperature of 3000 K for H_2 in layer 2, showing (a) the output of each layer at the top of the atmosphere contributing to the measured signal, based on a linear regression analysis to the data, and (b) the resultant comparison of data and model.

Figure 19. The G1 EUVS data for the north aurora with a three-layer model atmosphere of 1×10^{16} cm^{-2} of H_2 at T = 1000 K in layer 1, of 1×10^{18} cm^{-2} of H_2 at T=900 K in layer 2 and 2×10^{17} cm^{-2} of CH_4 and 1×10^{20} cm^{-2} H_2 at 600 K in layer 3, showing (a) the count rate produced by each layer contributing to the measured signal, based on a linear regression analysis to the data with (4) as the transmission function, and (b) the resultant comparison of data and model.

Figure 20. The G1 EUVS data for the south aurora with a three-layer model atmosphere of 1 x 10^{16} cm^{-2} of H_2 at T = 1000 K in layer 1, of 1 x 10^{18} cm^{-2} of H_2 at T=900 K in layer 2, and 2 x 10^{17} cm^{-2} of CH_4 and 1 x 10^{20} cm^{-2} of H_2 at 600 K in layer 3, showing (a) the count rate produced by each layer at the top of the atmosphere, contributing to the measured signal, based on a linear regression analysis to the data, and (b) the resultant comparison of data and model. The transmission function model used in these plots was (4). The regression analysis results for transmission function (5) were identical with about twice the amount of CH_4 required for best fit.

Figure 21. The C3 EUVS data for the south with a three-layer model atmosphere of 1 x 10^{16} cm^{-2} of H_2 at T = 1000 K in layer 1, of 1 x 10^{18} cm^{-2} of H_2 at T=900 K in layer 2, and 2 x 10^{17} cm^{-2} of CH_4 and 1 x 10^{20} cm^{-2} of H_2 at 600 K in layer 3, showing (a) the count rate produced by each layer at the top of the atmosphere, contributing to the measured signal, based on a linear regression analysis to the data, and (b) the resultant comparison of data and model. The transmission function model used in these plots was (4). The regression analysis results for transmission function (5) were identical with about twice the amount of CH_4 required for best fit.

Figure 22. The E4 EUVS data for the north with a three-layer model atmosphere of 1 x 10^{16} cm^{-2} of H_2 at T = 1000 K in layer 1, of 1 x 10^{18} cm^{-2} of H_2 at T=900 K in layer 2, and 2 x 10^{17} cm^{-2} of CH_4 and 1 x 10^{20} cm^{-2} of H_2 at 600 K in layer 3, showing (a) the count rate produced by each layer at the top of the atmosphere, contributing to the measured signal, based on a linear regression analysis to the data, and (b) the resultant comparison of data and model. The transmission function model used in these plots was (4). The regression analysis results for transmission function (5) were identical with about twice the amount of CH_4 required for best fit.

Figure 23. The linear regression fit to the summed EUVS data for G1 + C3 + E4: (a) north and (b) south. The transmission function model used in these plots was (4). The regression analysis results for transmission function (5) were identical with about twice the amount of CH_4 required for best fit.

Figure 24. Comparison of south auroral FUV spectra from HST GHRS from September 1996 and Galileo UVS spectra from G1 and E4 of the southern aurora. The GHRS spectrum was at 4.8 Å FWHM, compared to the UVS 6.5 Å FWHM.

Figure 25. A comparison of the H_2 electron impact induced fluorescence spectrum for an *Opal et al.* [1971] secondary electron distribution for a 500 K gas and a warm 27 eV secondary electron distribution for a 1400 K gas.

Figure 26. Depth of penetration of primary electrons based on cross sections of *Northcliffe and Schilling* [1970].

Figure 1. North ecliptic view of the Galileo trajectory during the orbital tour. The spacecraft z axis is nominally pointed in the Earth direction, and the UVS/EUVS can be boresighted to look at the torus and aurora. The orbit numbers are indicated. The white area is the time during which the bulk of the UVS/EUVS observations were planned. Jupiter and the Io torus are available in the region called Io torus period. The 15 R_J radiation constraint is a predicted closest approach distance to operate the instrument. The dark stippled area is the time when the cone angle of Jupiter system is less than 90° and unobservable by the UVS because of spacecraft obstructions.

Plate 1. (a) The geometry for the simultaneous UVS/EUVS observations on C3 (G02C-sequence) at time of crossing the CML of Jupiter. The UVS slit is 1°x 0.1° FWHM rectangular field of view. The EUVS slit is 0.87°x 0.17° triangular field of view. The sector size for the EUVS is 0.87° x 0.4°. (b) The EUVS image of the aurora for G1, C3, and E4 in H Lyα and in the H_2 Rydberg bands. Time is the linear x axis scale as produced by spacecraft motion. The width of each pixel is proportional to the spectral integration time (30 or 60 RIMS), and the height is proportional to the sector size (0.4°) traced out by the spacecraft spin in 21.4 ms.

Figure 2. The EUVS north spectrum for three of the Big Four orbits that obtained spectra: G1, C3, and E4. The units for signals are shown in counts per 0.2 RIM and counts per second. The signal rate magnitudes are close to the total counts received in that orbit. The 1σ error bar for the signal at any wavelength can be found by dividing the count rate by 2.5, which gives the photon events. The square root of the number of photon events is the 1σ error bar. We show the 1σ error bar for the peak signal. The wavelength regions of the Rydberg bands are indicated.

Figure 3. The EUVS south spectrum for three of the Big Four orbits that obtained spectra: G1, C3, and E4. The units for signals are shown in counts per 0.2 RIM and counts per second. The signal rate magnitudes are close to the total counts received in that orbit. The 1σ error bar for the signal at any wavelength can be found by dividing the count rate by 2.5, which gives the photon events. The square root of the number of photon events is the 1σ error bar. We show the 1σ error bar for the peak signal.

Figure 4. The EUVS G1 north spectrum count rate (dotted line) compared to the predicted torus background signal (solid line) for the length of time of the observation. The torus background is obtained from a summation of all the total torus spectra from the Big Four. There is a torus background present in all aurora observations over the approximately 0.2 RIM of the observation. The torus spectrum is subtracted from all EUVS aurora observations by normalizing the estimated torus background signal to the actual auroral observation. The signal rate magnitudes are close to the total counts received in that orbit. The 1σ error bar for the signal at any wavelength can be found by dividing the count rate by 2.5, which gives the photon events. The square root of the number of photon events is the 1σ error bar.

Figure 5. The spectrum of the total of all counts received in G1+ C3+ E4 for (a) the south and (b) the north. The ± 1σ signal statistics are indicated as plus signs.

Figure 6. The UVS spectrum measured simultaneous to or closest in time to the EUVS observations for the north aurora for G1, C3, and E4. The preflight UVS $H_2 + e$ (100 eV) electron impact calibration spectrum is also shown. The 1σ error bar for the signal level in any channel can be calculated as the square root of the plotted count rate times the length of time of the measurement, given in seconds in the plot.

Figure 7. The UVS relative intensity variation as a function of wavelength, normalized to 1580 Å for the northern aurora G1, C3, E4. The preflight electron impact spectrum is also shown.

Figure 8. The UVS spectrum measured simultaneous to or closest in time to the EUVS observations for the south aurora for G1, C3, and E4. The 1σ error bar for the signal level in any channel can be calculated as the square root of the plotted count rate times the length of time of the measurement, given in seconds in the plot.

Figure 9. The UVS relative intensity variation as a function of wavelength, normalized to 1580 Å for the southern aurora G1, C3, and E4. The preflight electron impact spectrum is also shown.

Plate 2. Hubble Space Telescope WFPC 2 image of the G1 south aurora as would be observed by Galileo UVS at time of G1 south observation. The HST observation occurred at day 176 15^h 07^m with a CML of 6°.

Plate 3. Hubble Space Telescope WFPC 2 image of the G1 north aurora as would be observed by Galileo UVS at time of G1 north observation. The HST observation occurred at day 176 18^h 19^m with a CML of 119°. The terminator is shown near 60°W longitude.

Figure 10. Transmission function of hydrocarbon absorbers in the FUV for two analytic models and the model atmosphere of *Gladstone and Skinner* [1989].

Figure 11. Secondary electron flux from $e + H_2$ primary ionization. The data of *Opal et al.*, [1971] and model are shown, along with the model parameters as described in the text. $f(E)$ is the secondary electron distribution.

Figure 12. The Maxwellian model of secondary electrons of Figure 11 are used for the production of an electron impact induced FUV spectrum and a monoenergetic electron impact model spectrum at 100 eV. In addition, we show the preflight laboratory spectrum at 100 eV spectrum.

Figure 13. The low-latitude nonauroral atmosphere based on the Galileo probe results [*Seiff et al.*, 1996; 1997] and the photochemical models for CH_4 [*Gladstone et al.*, 1996].

Figure 14. The G1 UVS FUV observations on day of year (DOY) 176 and model (a) north and (b) south for the hydrocarbon transmission function of (4) and model (c) north for the hydrocarbon transmission function of (5), $1./(1. + \tau)$. In Figures 14d and 14e are the absorption cross section of the six absorbers, CH_4 [*Mount et al.*, 1977], C_2H_2 [*Nakayama and Watanabe*, 1964; *Suto and Lee*, 1984; *Wu et al.*, 1989], C_2H_6 [*Mount et al.*, 1978], C_3H_8, C_2H_4, and C_4H_{10} (see *Gladstone et al.* [1996] for remaining absorption cross section references) to model the G1 south aurora. In Figure 14f is the transmission function derived from the *Gladstone et al.* [1996] model atmosphere. The number density at the Chapman layer peak is 1.2×10^{14} cm^{-3}. We plot the best fit model in Figure 14g of the G1 south observation compared with the G1 south data and the source region H_2 emission spectrum. We plot in Figure 14h the altitude profile of the model atmosphere [*Gladstone et al.*, 1996] and the volume emission rate, $V(cm^{-3}s^{-1})$. The Chapman layer vertical peak column abundances are listed along with the altitude z_* and number density $N(z_*)$.

Figure 15. The C3 UVS FUV observations on DOY 304 and model (a) north and (b) south for the hydrocarbon transmission function of (4).

Figure 16. The E4 UVS FUV observations on DOY 347 and model (a) north and (b) south for the hydrocarbon transmission function of (4).

Figure 17. The G1 EUVS data for the south aurora with a two-layer model atmosphere of 1×10^{18} cm^{-2} of H_2 in layer 1 and 5×10^{16} cm^{-2} of CH_4 and 1×10^{21} cm^{-2} H_2 in layer 2, showing (a) the amount of radiation from each layer at the top of the atmosphere, contributing to the measured signal, based on a linear regression analysis to the data, and (b) the resultant comparison of data and model.

Figure 18. The C3 EUVS data for the south aurora with a two-layer model atmosphere of 1×10^{19} cm^{-2} of H_2 in layer 1 and 5×10^{16} cm^{-2} of CH_4 and 1×10^{21} cm^{-2} of H_2 at a temperature of 3000 K for H_2 in layer 2, showing (a) the output of each layer at the top of the atmosphere contributing to the measured signal, based on a linear regression analysis to the data, and (b) the resultant comparison of data and model.

Figure 19. The G1 EUVS data for the north aurora with a three-layer model atmosphere of 1×10^{16} cm^{-2} of H_2 at $T = 1000$ K in layer 1, of 1×10^{18} cm^{-2} of H_2 at T=900 K in layer 2 and 2×10^{17} cm^{-2} of CH_4 and 1×10^{20} cm^{-2} H_2 at 600 K in layer 3, showing (a) the count rate produced by each layer contributing to the measured signal, based on a linear regression analysis to the data with (4) as the transmission function, and (b) the resultant comparison of data and model.

Figure 20. The G1 EUVS data for the south aurora with a three-layer model atmosphere of 1×10^{16} cm^{-2} of H_2 at $T = 1000$ K in layer 1, of 1×10^{18} cm^{-2} of H_2 at T=900 K in layer 2, and 2×10^{17} cm^{-2} of CH_4 and 1×10^{20} cm^{-2} of H_2 at 600 K in layer 3, showing (a) the count rate produced by each layer at the top of the atmosphere, contributing to the measured signal, based on a linear regression analysis to the data, and (b) the resultant comparison of data and model. The transmission function model used in these plots was (4). The regression analysis results for transmission function (5) were identical with about twice the amount of CH_4 required for best fit.

Figure 21. The C3 EUVS data for the south with a three-layer model atmosphere of 1×10^{16} cm^{-2} of H_2 at $T = 1000$ K in layer 1, of 1×10^{18} cm^{-2} of H_2 at T=900 K in layer 2, and 2×10^{17} cm^{-2} of CH_4 and 1×10^{20} cm^{-2} of H_2 at 600 K in layer 3, showing (a) the count rate produced by each layer at the top of the atmosphere, contributing to the measured signal, based on a linear regression analysis to the data, and (b)

the resultant comparison of data and model. The transmission function model used in these plots was (4). The regression analysis results for transmission function (5) were identical with about twice the amount of CH_4 required for best fit.

Figure 22. The E4 EUVS data for the north with a three-layer model atmosphere of 1 x 10^{16} cm^{-2} of H_2 at T = 1000 K in layer 1, of 1 x 10^{18} cm^{-2} of H_2 at T=900 K in layer 2, and 2 x 10^{17} cm^{-2} of CH_4 and 1 x 10^{20} cm^{-2} of H_2 at 600 K in layer 3, showing (a) the count rate produced by each layer at the top of the atmosphere, contributing to the measured signal, based on a linear regression analysis to the data, and (b) the resultant comparison of data and model. The transmission function model used in these plots was (4). The regression analysis results for transmission function (5) were identical with about twice the amount of CH_4 required for best fit.

Figure 23. The linear regression fit to the summed EUVS data for G1 + C3 + E4: (a) north and (b) south. The transmission function model used in these plots was (4). The regression analysis results for transmission function (5) were identical with about twice the amount of CH_4 required for best fit.

Figure 24. Comparison of south auroral FUV spectra from HST GHRS from September 1996 and Galileo UVS spectra from G1 and E4 of the southern aurora. The GHRS spectrum was at 4.8 Å FWHM, compared to the UVS 6.5 Å FWHM.

Figure 25. A comparison of the H_2 electron impact induced fluorescence spectrum for an *Opal et al.* [1971] secondary electron distribution for a 500 K gas and a warm 27 eV secondary electron distribution for a 1400 K gas.

Figure 26. Depth of penetration of primary electrons based on cross sections of *Northcliffe and Schilling* [1970].

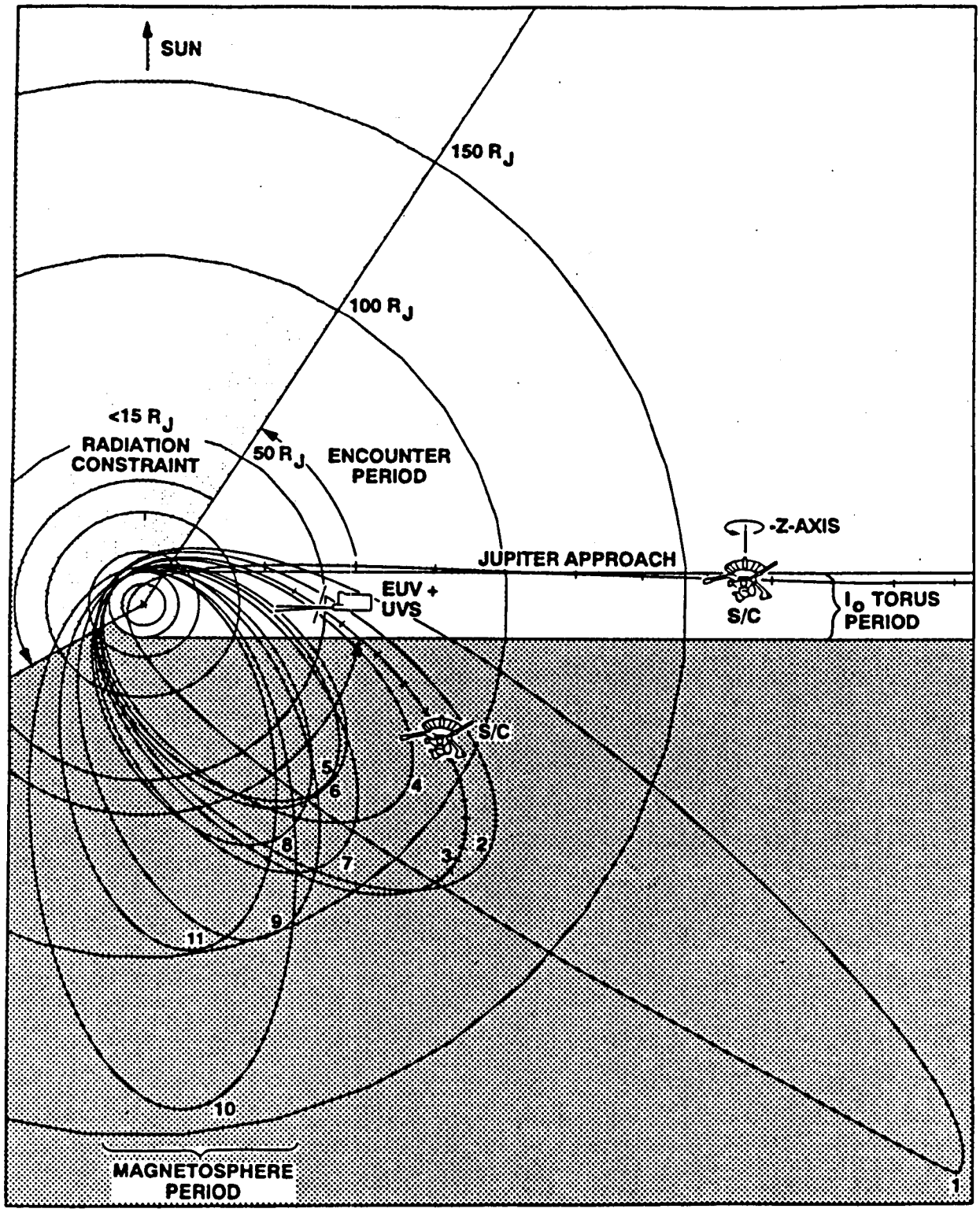
SUN
150 R J
100 R J
<15 R J
RADIATION CONSTRAINT
50 R J
ENCOUNTER PERIOD
-Z-AXIS
JUPITER APPROACH
EUV + UVS
S/C
I o TORUS PERIOD
S/C
1
2
3
4
5
6
7
8
9
10
11
MAGNETOSPHERE PERIOD

Fig. 1

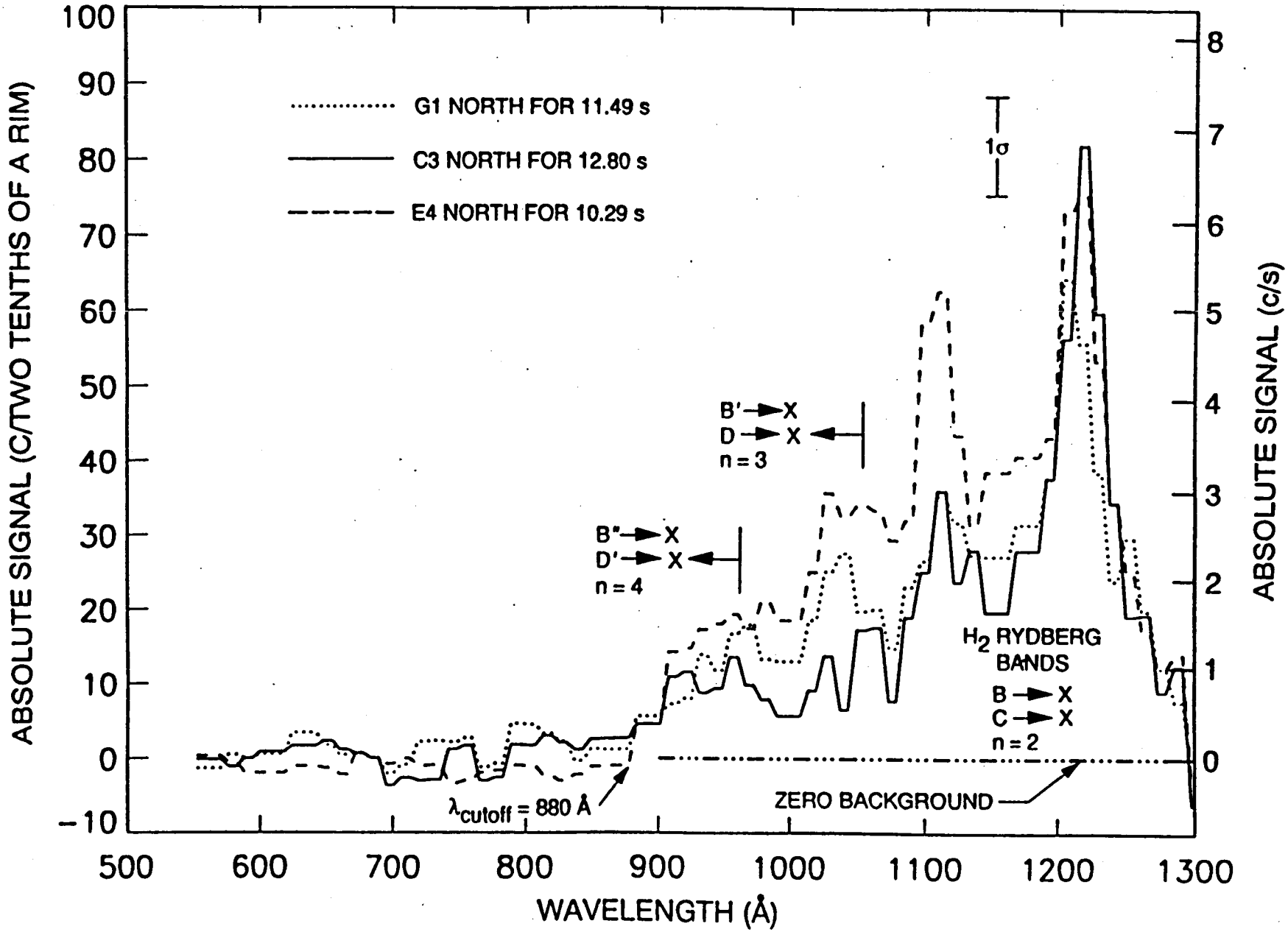
G1 NORTH FOR 11.49 s
C3 NORTH FOR 12.80 s
E4 NORTH FOR 10.29 s
1σ
B' → X
D → X
n = 3
B'' → X
D' → X
n = 4
H2 RYDBERG BANDS
B → X
C → X
n = 2
λcutoff = 880 Å
ZERO BACKGROUND
ABSOLUTE SIGNAL (C/TWO TENTHS OF A RIM)
ABSOLUTE SIGNAL (c/s)
WAVELENGTH (Å)
100
90
80
70
60
50
40
30
20
10
0
−10
8
7
6
5
4
3
2
1
0
500
600
700
800
900
1000
1100
1200
1300

Fig. 2

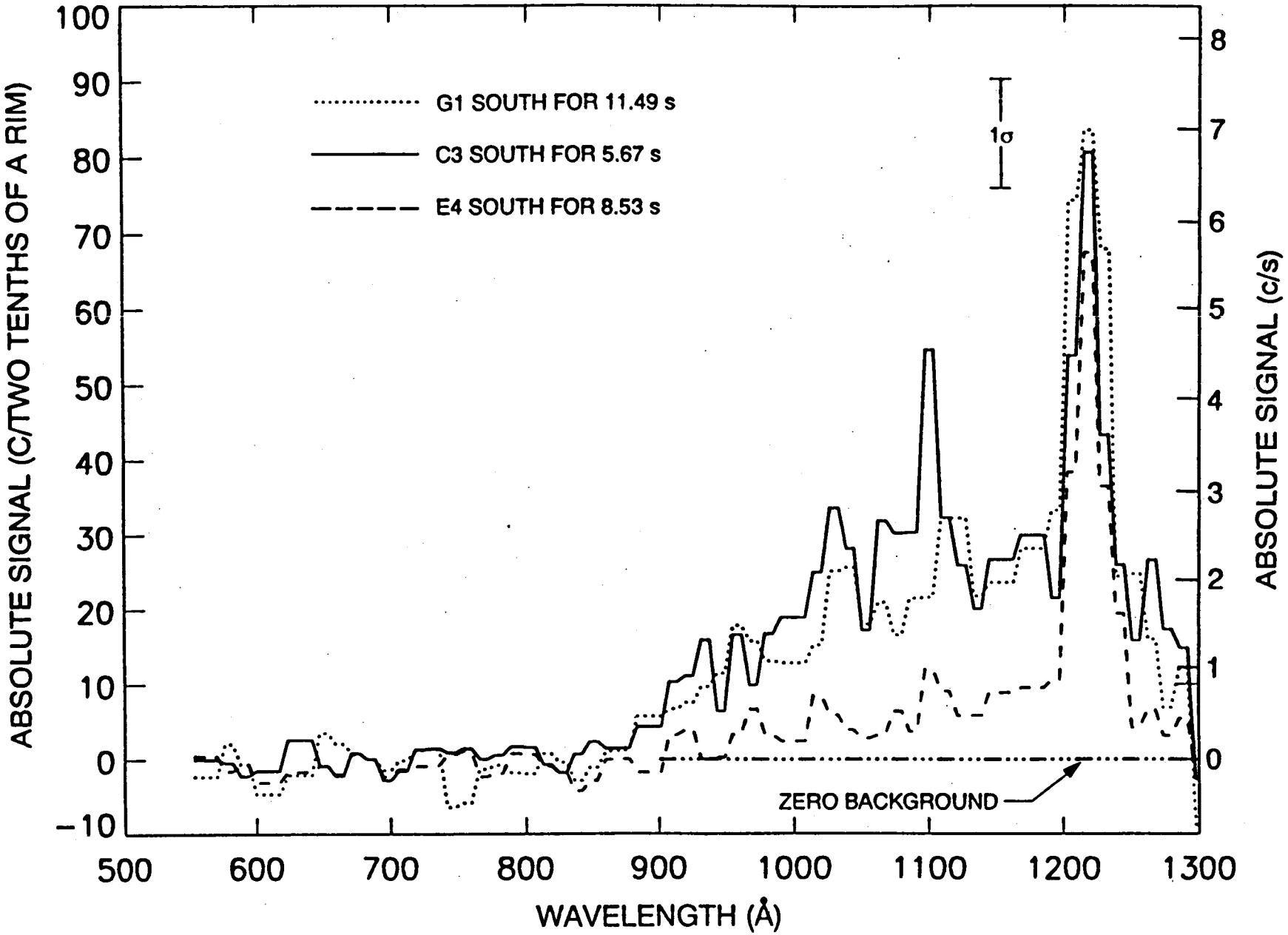
G1 SOUTH FOR 11.49 s
C3 SOUTH FOR 5.67 s
E4 SOUTH FOR 8.53 s
1σ
ZERO BACKGROUND
ABSOLUTE SIGNAL (C/TWO TENTHS OF A RIM)
ABSOLUTE SIGNAL (c/s)
WAVELENGTH (Å)
100
90
80
70
60
50
40
30
20
10
0
−10
8
7
6
5
4
3
2
1
0
500
600
700
800
900
1000
1100
1200
1300

Fig. 3

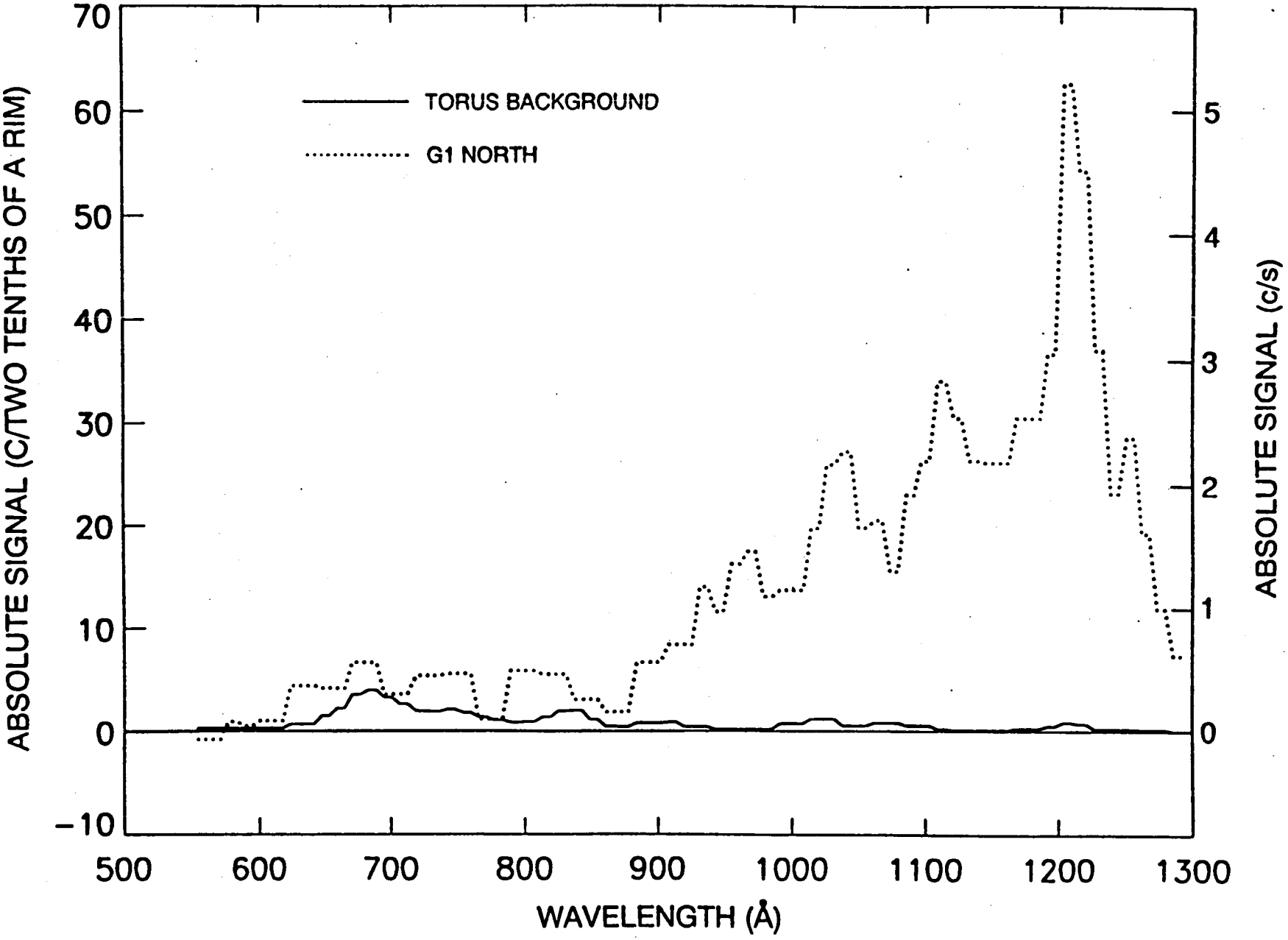
TORUS BACKGROUND
G1 NORTH
ABSOLUTE SIGNAL (C/TWO TENTHS OF A RIM)
ABSOLUTE SIGNAL (c/s)
WAVELENGTH (Å)
70
60
50
40
30
20
10
0
−10
5
4
3
2
1
0
500
600
700
800
900
1000
1100
1200
1300

Fig. 4

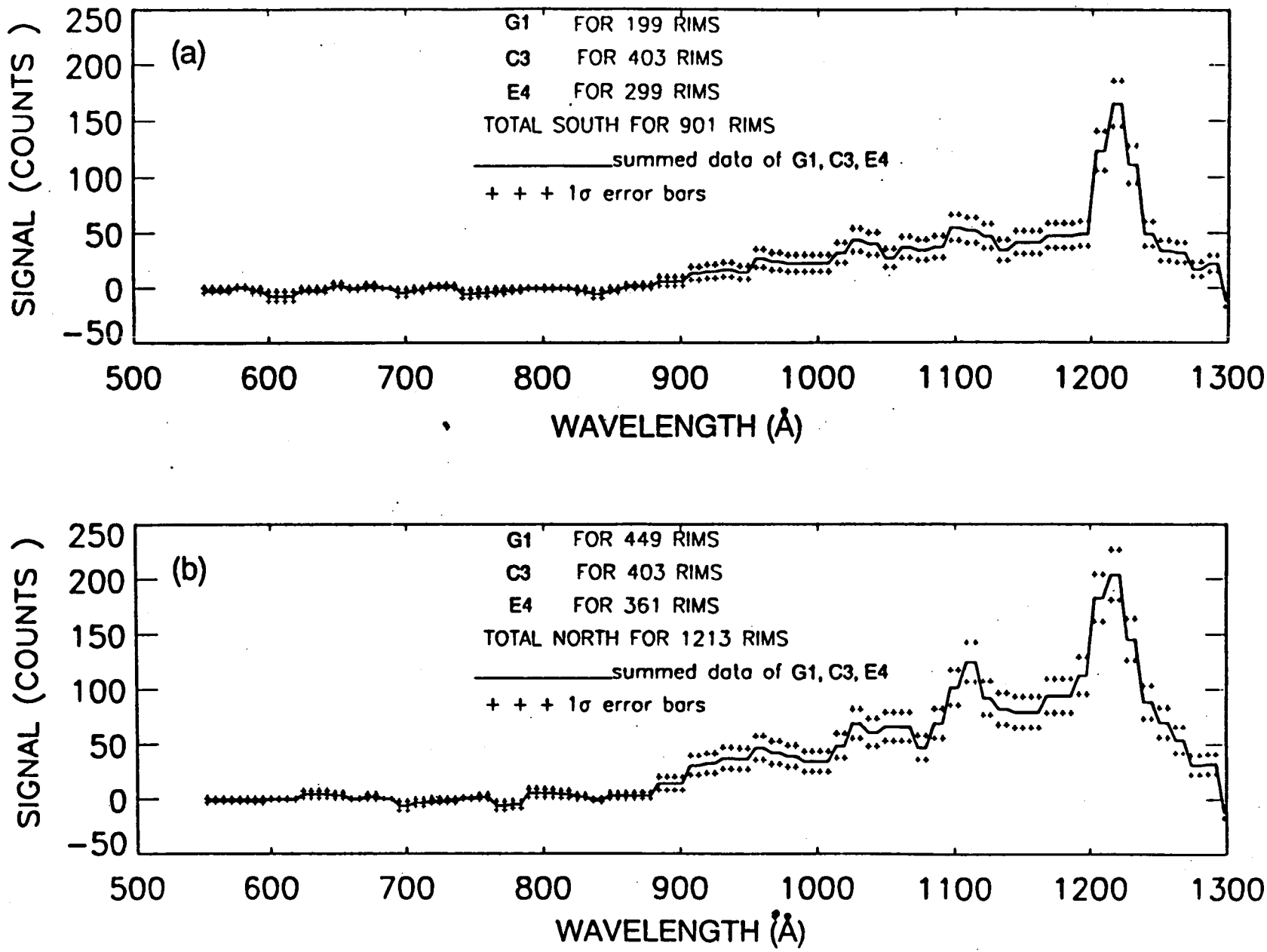
(a)
G1 FOR 199 RIMS
C3 FOR 403 RIMS
E4 FOR 299 RIMS
TOTAL SOUTH FOR 901 RIMS
summed data of G1, C3, E4
+ + + 1σ error bars
SIGNAL (COUNTS)
250
200
150
100
50
0
−50
500
600
700
800
900
1000
1100
1200
1300
WAVELENGTH (Å)
(b)
G1 FOR 449 RIMS
C3 FOR 403 RIMS
E4 FOR 361 RIMS
TOTAL NORTH FOR 1213 RIMS
summed data of G1, C3, E4
+ + + 1σ error bars
SIGNAL (COUNTS)
250
200
150
100
50
0
−50
500
600
700
800
900
1000
1100
1200
1300
WAVELENGTH (Å)

Fig. 5

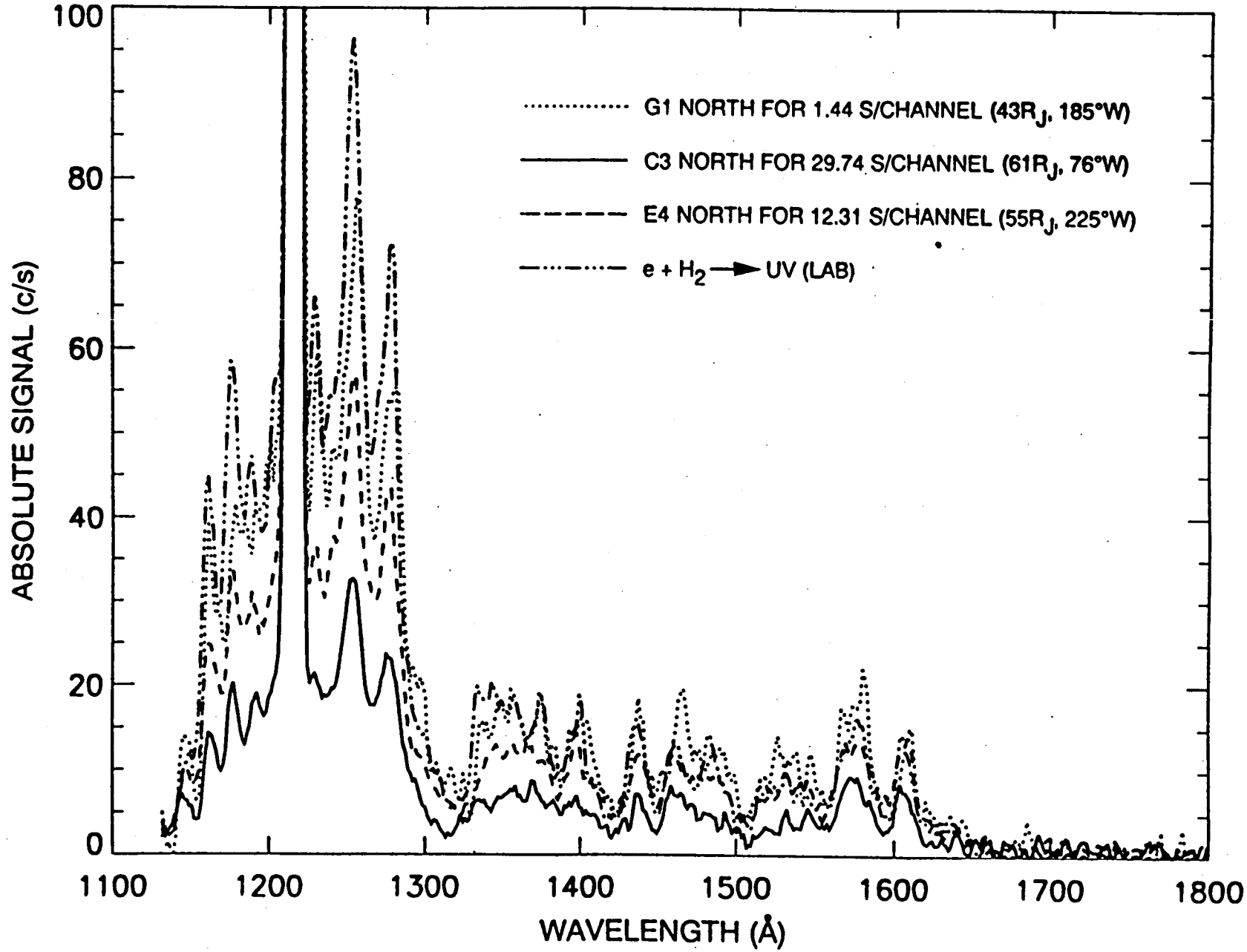
G1 NORTH FOR 1.44 S/CHANNEL (43R$_J$, 185°W)
C3 NORTH FOR 29.74 S/CHANNEL (61R$_J$, 76°W)
E4 NORTH FOR 12.31 S/CHANNEL (55R$_J$, 225°W)
e + H$_2$ → UV (LAB)
ABSOLUTE SIGNAL (c/s)
0
20
40
60
80
100
1100
1200
1300
1400
1500
1600
1700
1800
WAVELENGTH (Å)

Fig. 6

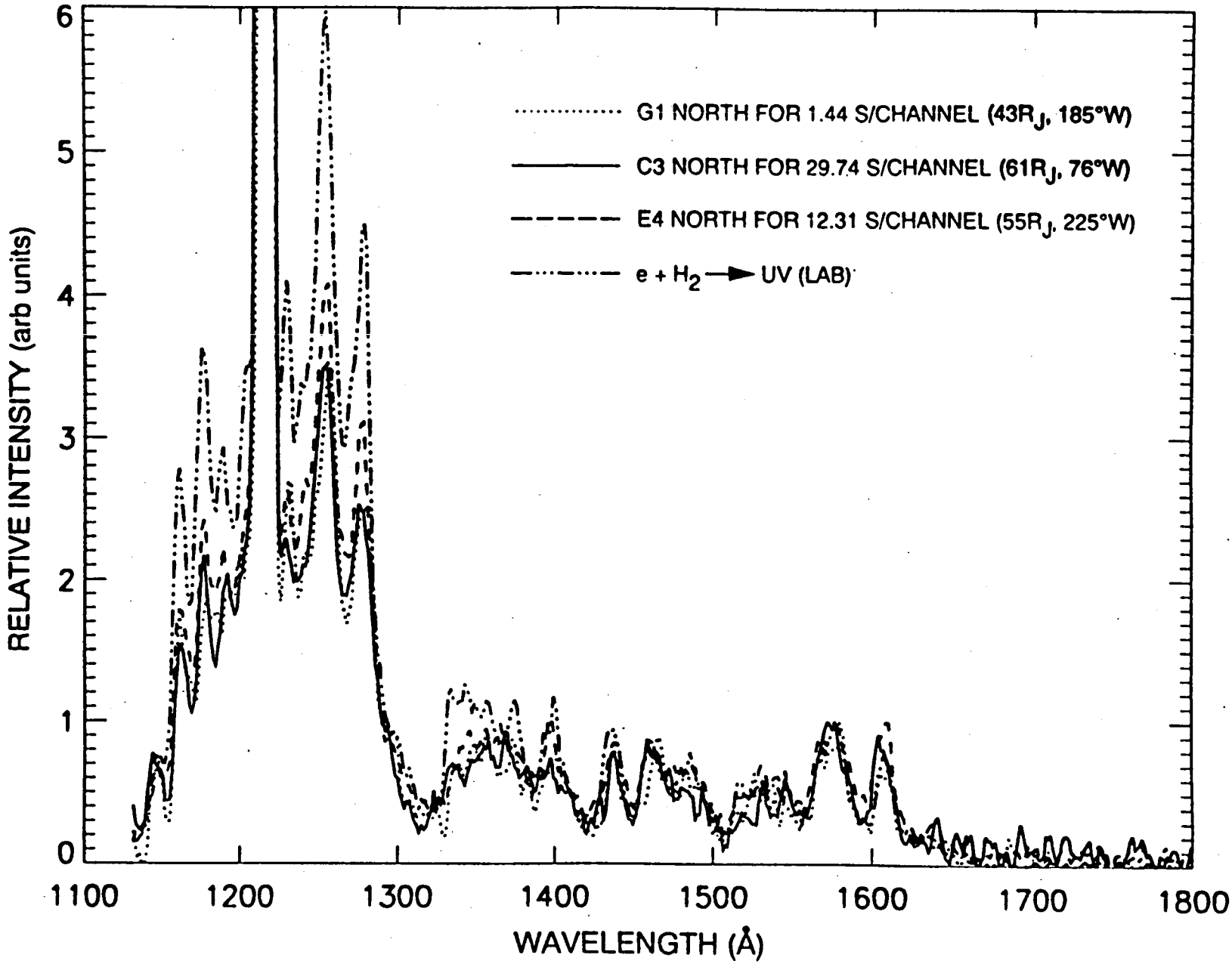
G1 NORTH FOR 1.44 S/CHANNEL (43R$_J$, 185°W)
C3 NORTH FOR 29.74 S/CHANNEL (61R$_J$, 76°W)
E4 NORTH FOR 12.31 S/CHANNEL (55R$_J$, 225°W)
e + H$_2$ → UV (LAB)
RELATIVE INTENSITY (arb units)
0
1
2
3
4
5
6
1100
1200
1300
1400
1500
1600
1700
1800
WAVELENGTH (Å)

Fig. 7

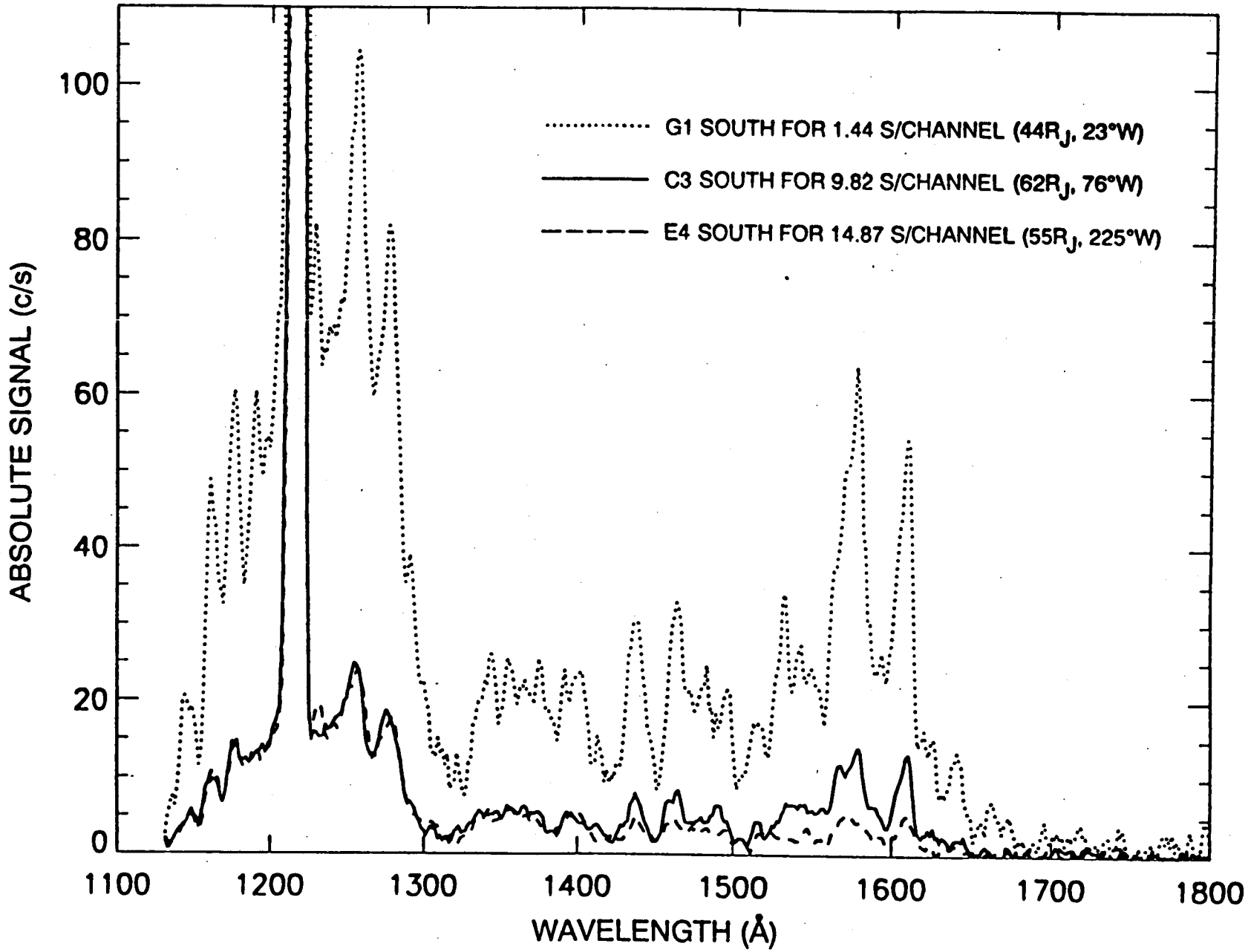
G1 SOUTH FOR 1.44 S/CHANNEL (44R$_J$, 23°W)
C3 SOUTH FOR 9.82 S/CHANNEL (62R$_J$, 76°W)
E4 SOUTH FOR 14.87 S/CHANNEL (55R$_J$, 225°W)
ABSOLUTE SIGNAL (c/s)
0
20
40
60
80
100
1100
1200
1300
1400
1500
1600
1700
1800
WAVELENGTH (Å)

ig. 8

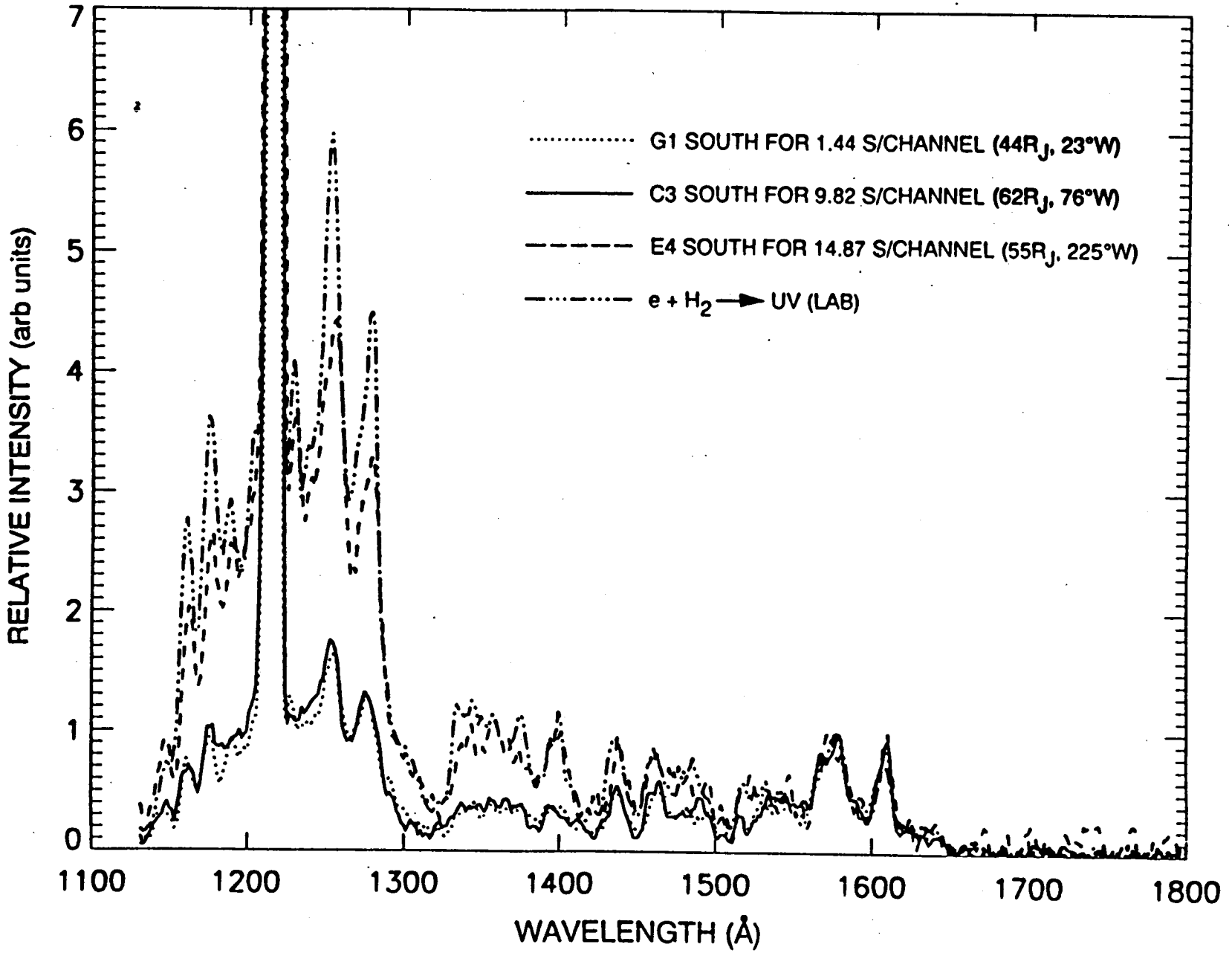
G1 SOUTH FOR 1.44 S/CHANNEL (44R$_J$, 23°W)
C3 SOUTH FOR 9.82 S/CHANNEL (62R$_J$, 76°W)
E4 SOUTH FOR 14.87 S/CHANNEL (55R$_J$, 225°W)
e + H$_2$ → UV (LAB)
RELATIVE INTENSITY (arb units)
WAVELENGTH (Å)
0
1
2
3
4
5
6
7
1100
1200
1300
1400
1500
1600
1700
1800

Fig. 9

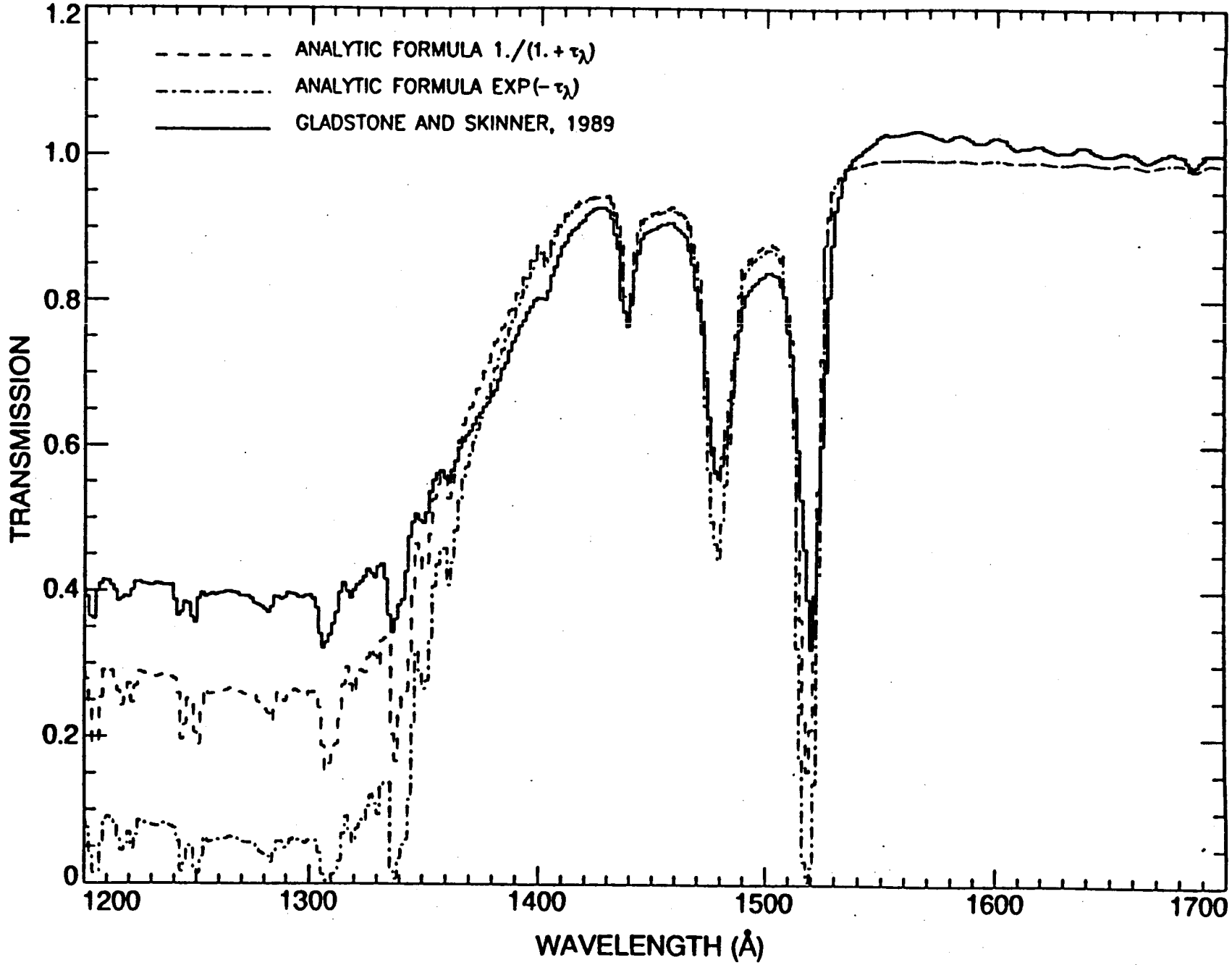
ANALYTIC FORMULA 1./(1. + τλ)
ANALYTIC FORMULA EXP(− τλ)
GLADSTONE AND SKINNER, 1989
TRANSMISSION
WAVELENGTH (Å)
0
0.2
0.4
0.6
0.8
1.0
1.2
1200
1300
1400
1500
1600
1700

Fig. 10

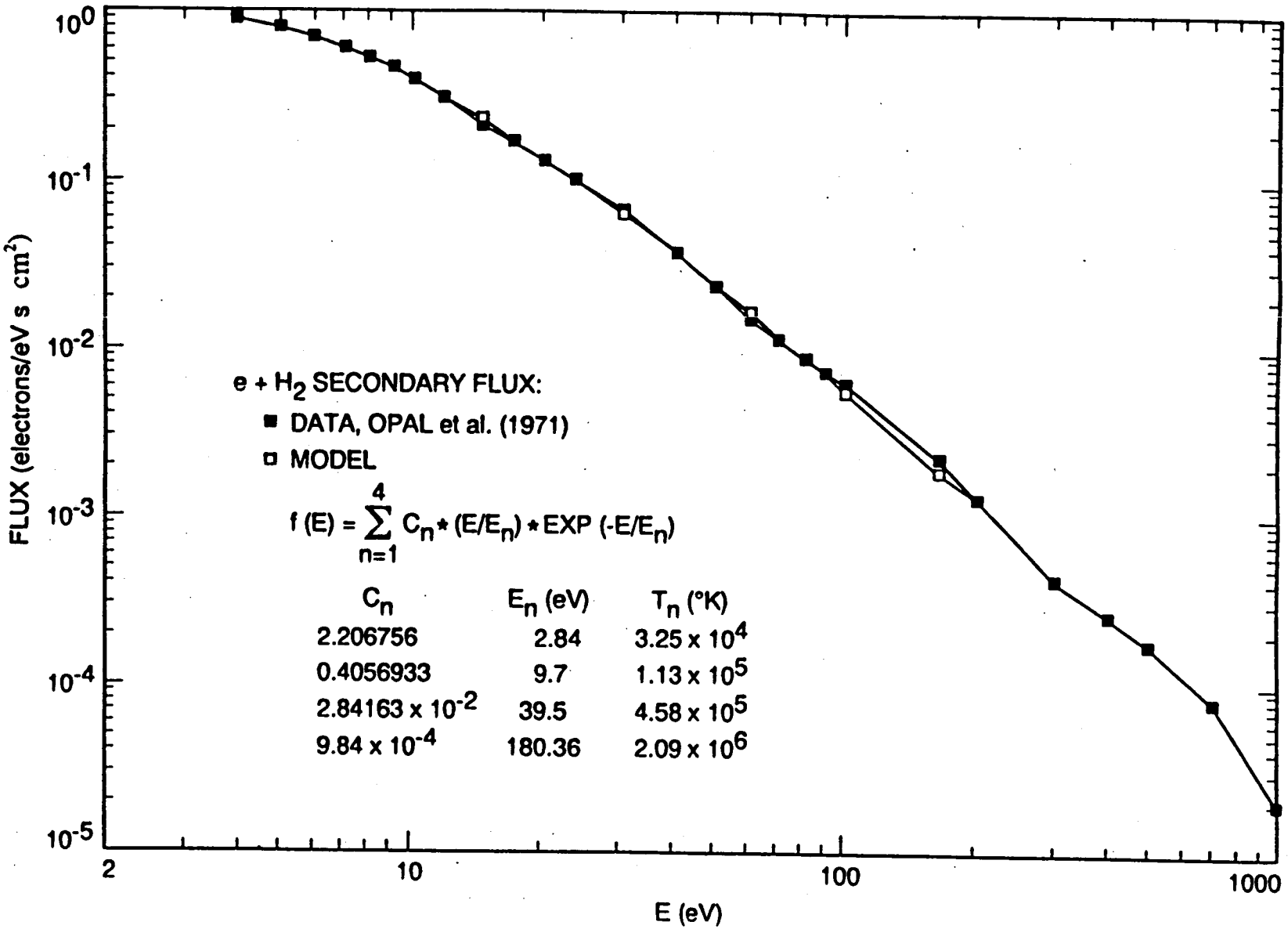
FLUX (electrons/eV s cm²)
E (eV)
e + H2 SECONDARY FLUX:
DATA, OPAL et al. (1971)
MODEL
f (E) = Σ (n=1 to 4) Cn * (E/En) * EXP (-E/En)
Cn | En (eV) | Tn (°K)
2.206756 | 2.84 | 3.25 x 10^4
0.4056933 | 9.7 | 1.13 x 10^5
2.84163 x 10^-2 | 39.5 | 4.58 x 10^5
9.84 x 10^-4 | 180.36 | 2.09 x 10^6

Fig. 11

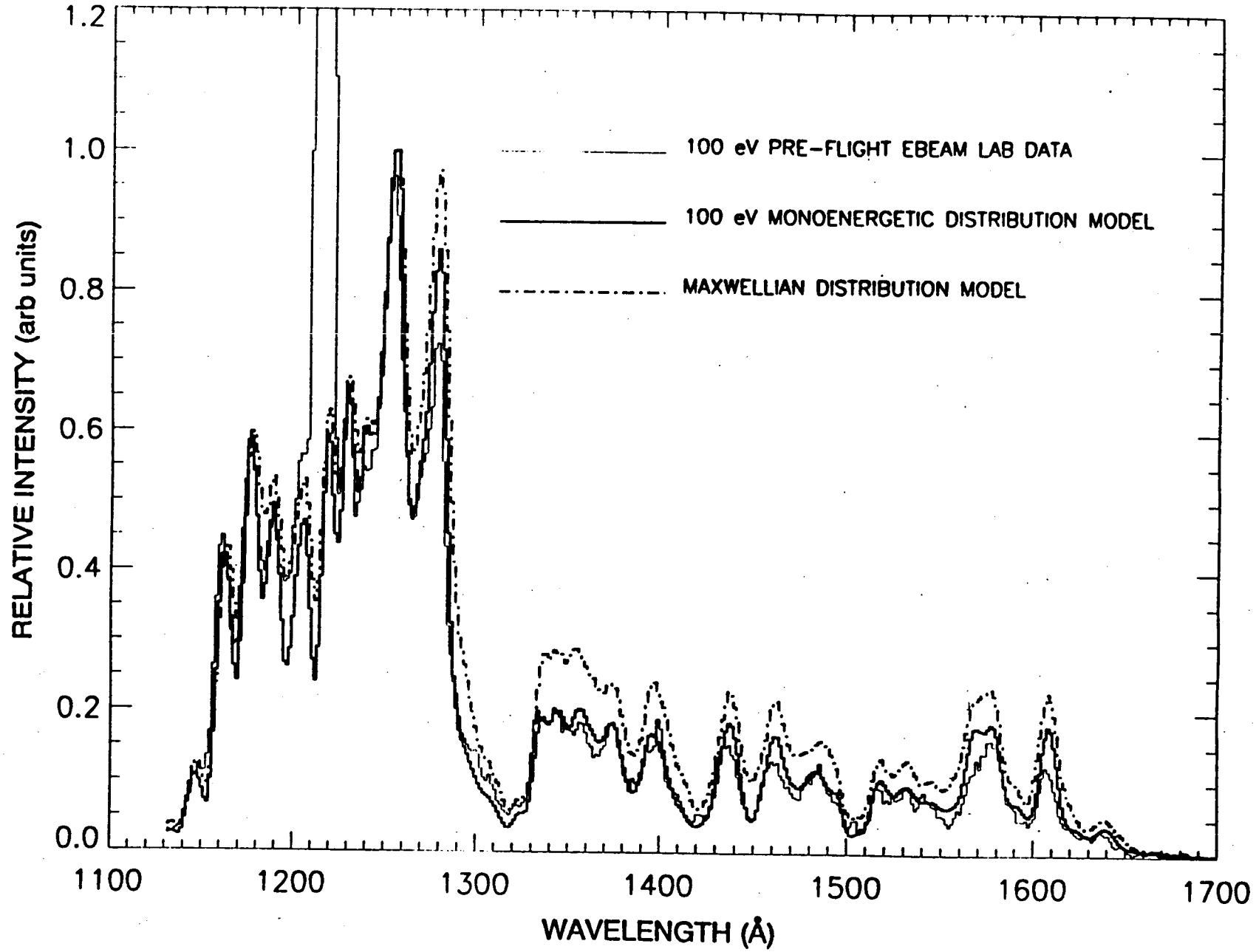
100 eV PRE-FLIGHT EBEAM LAB DATA
100 eV MONOENERGETIC DISTRIBUTION MODEL
MAXWELLIAN DISTRIBUTION MODEL
RELATIVE INTENSITY (arb units)
WAVELENGTH (Å)
0.0
0.2
0.4
0.6
0.8
1.0
1.2
1100
1200
1300
1400
1500
1600
1700

Fig. 12

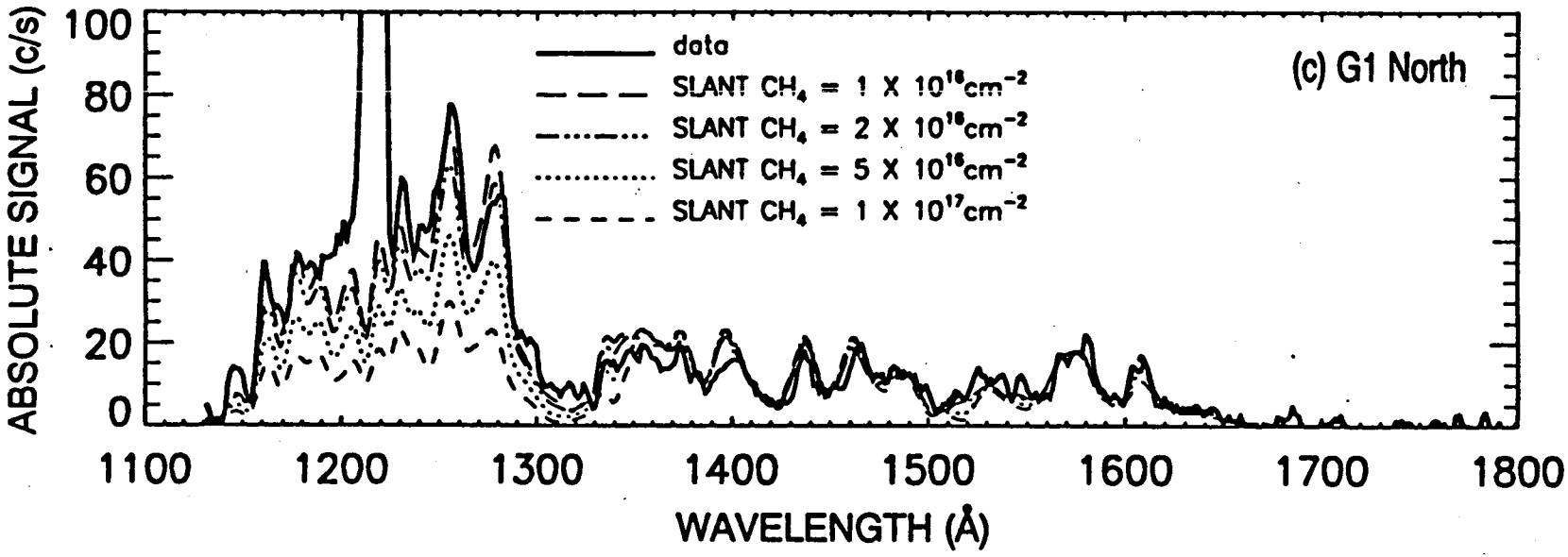
ABSOLUTE SIGNAL (c/s)
100
80
60
40
20
0
1100
1200
1300
1400
1500
1600
1700
1800
WAVELENGTH (Å)
data
SLANT CH4 = 1 X 10^16cm^-2
SLANT CH4 = 2 X 10^16cm^-2
SLANT CH4 = 5 X 10^16cm^-2
SLANT CH4 = 1 X 10^17cm^-2
(c) G1 North

Fig. 14c

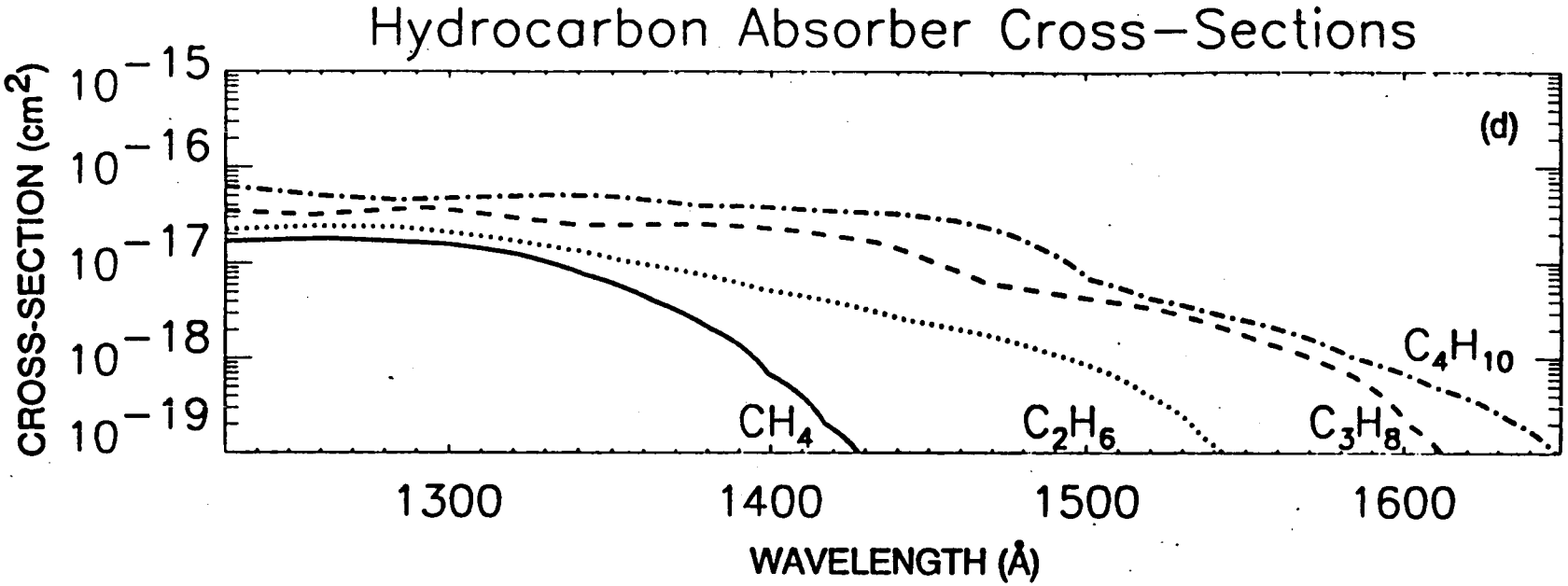
Hydrocarbon Absorber Cross-Sections
CROSS-SECTION (cm²)
10⁻¹⁵
10⁻¹⁶
10⁻¹⁷
10⁻¹⁸
10⁻¹⁹
(d)
C₄H₁₀
CH₄
C₂H₆
C₃H₈
1300
1400
1500
1600
WAVELENGTH (Å)

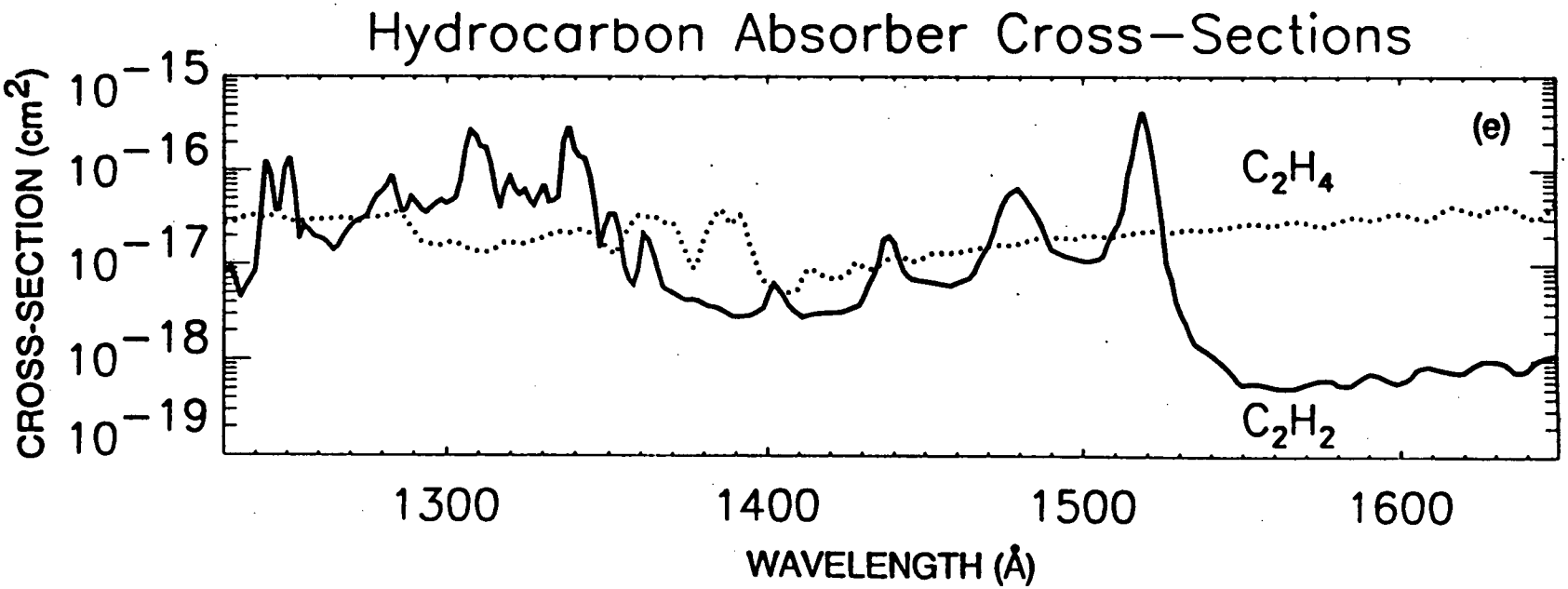
Hydrocarbon Absorber Cross-Sections
CROSS-SECTION (cm²)
10⁻¹⁵
10⁻¹⁶
10⁻¹⁷
10⁻¹⁸
10⁻¹⁹
(e)
C₂H₄
C₂H₂
1300
1400
1500
1600
WAVELENGTH (Å)

Fig. 14d,e

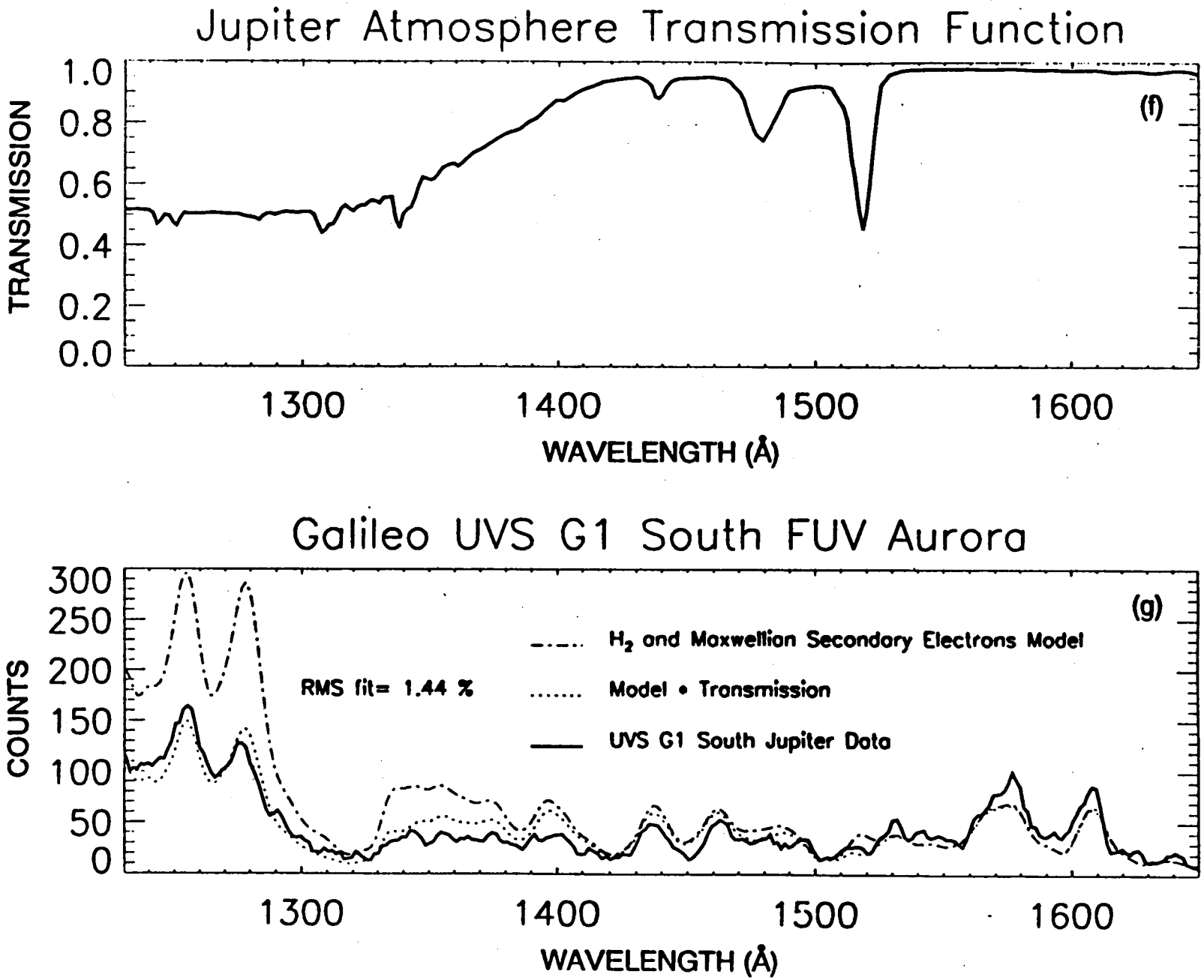
Jupiter Atmosphere Transmission Function
TRANSMISSION
1.0
0.8
0.6
0.4
0.2
0.0
(f)
1300
1400
1500
1600
WAVELENGTH (Å)
Galileo UVS G1 South FUV Aurora
COUNTS
300
250
200
150
100
50
0
(g)
RMS fit= 1.44 %
H2 and Maxwellian Secondary Electrons Model
Model • Transmission
UVS G1 South Jupiter Data
1300
1400
1500
1600
WAVELENGTH (Å)

Fig. 14f,g

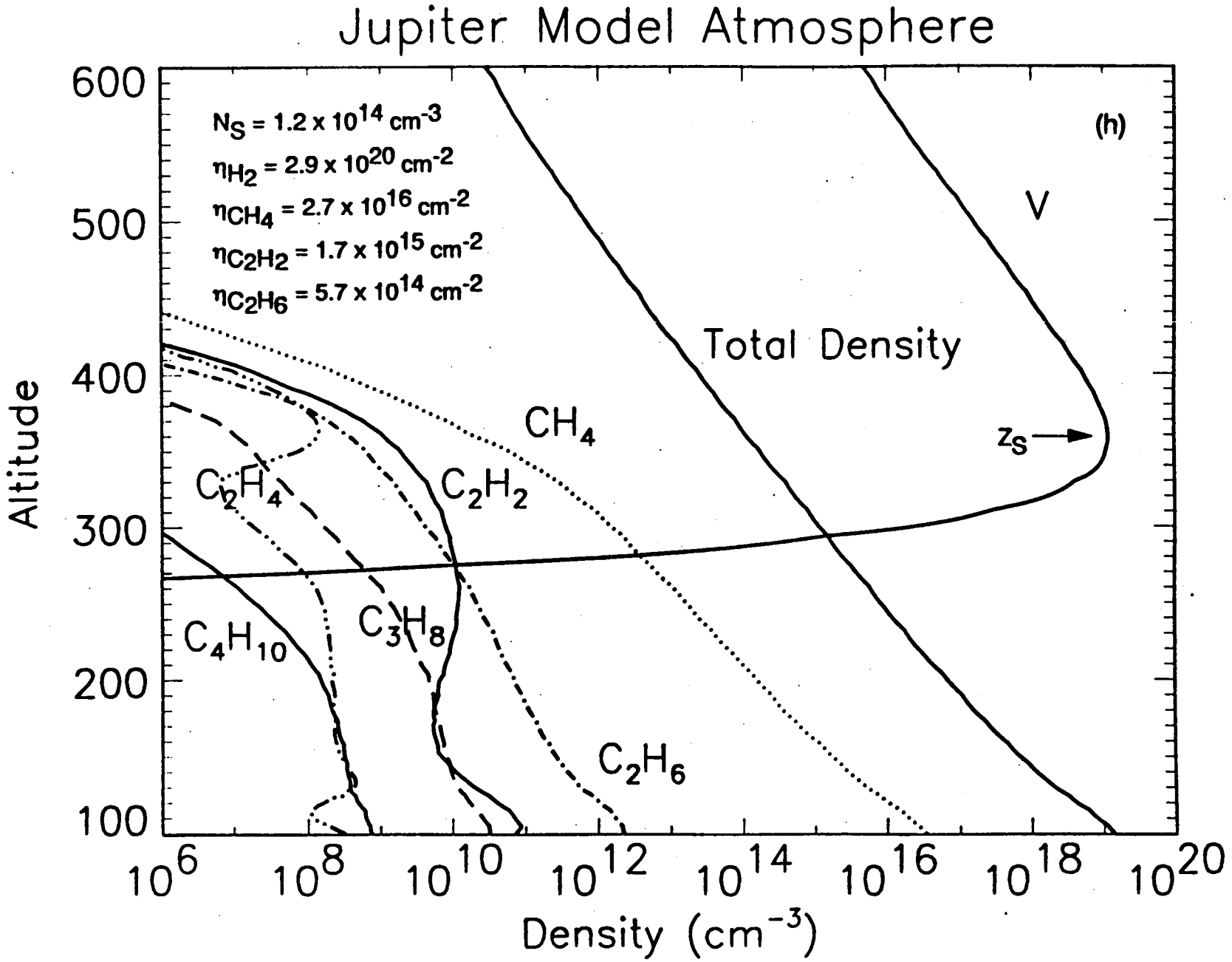
Jupiter Model Atmosphere
$N_S = 1.2 \times 10^{14}$ cm^{-3}
$\eta_{H_2} = 2.9 \times 10^{20}$ cm^{-2}
$\eta_{CH_4} = 2.7 \times 10^{16}$ cm^{-2}
$\eta_{C_2H_2} = 1.7 \times 10^{15}$ cm^{-2}
$\eta_{C_2H_6} = 5.7 \times 10^{14}$ cm^{-2}
(h)
V
Total Density
z_S
CH_4
C_2H_4
C_2H_2
C_4H_{10}
C_3H_8
C_2H_6
Altitude
600
500
400
300
200
100
10^6 10^8 10^{10} 10^{12} 10^{14} 10^{16} 10^{18} 10^{20}
Density (cm^{-3})

Fig. 14h

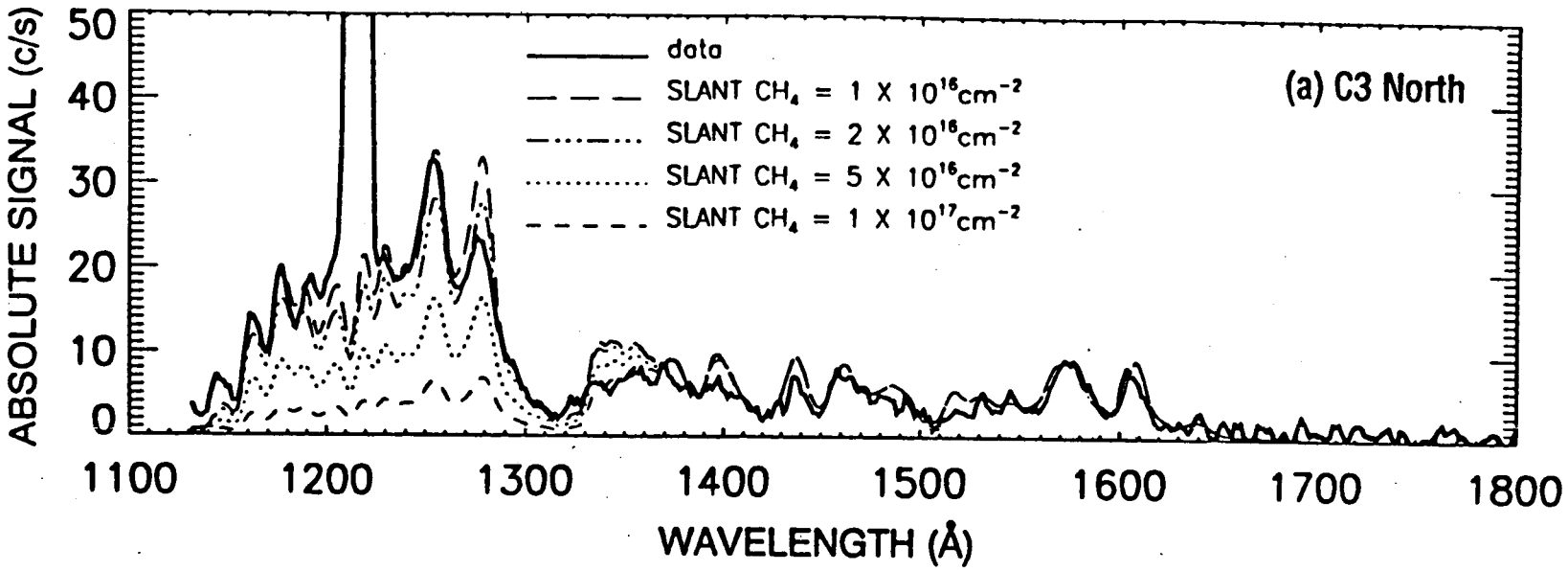
ABSOLUTE SIGNAL (c/s)
50
40
30
20
10
0
data
SLANT CH_4 = 1 X $10^{16}cm^{-2}$
SLANT CH_4 = 2 X $10^{16}cm^{-2}$
SLANT CH_4 = 5 X $10^{16}cm^{-2}$
SLANT CH_4 = 1 X $10^{17}cm^{-2}$
(a) C3 North
1100
1200
1300
1400
1500
1600
1700
1800
WAVELENGTH (Å)

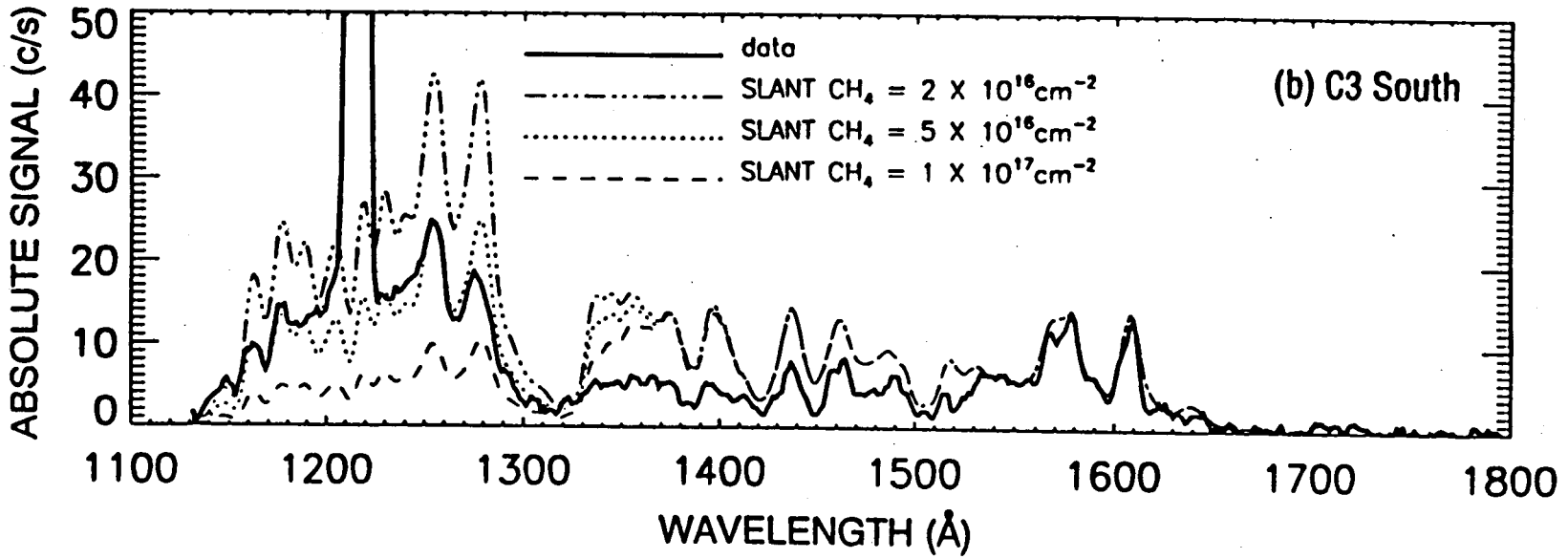
ABSOLUTE SIGNAL (c/s)
50
40
30
20
10
0
data
SLANT CH_4 = 2 X $10^{16}cm^{-2}$
SLANT CH_4 = 5 X $10^{16}cm^{-2}$
SLANT CH_4 = 1 X $10^{17}cm^{-2}$
(b) C3 South
1100
1200
1300
1400
1500
1600
1700
1800
WAVELENGTH (Å)

Fig. 15

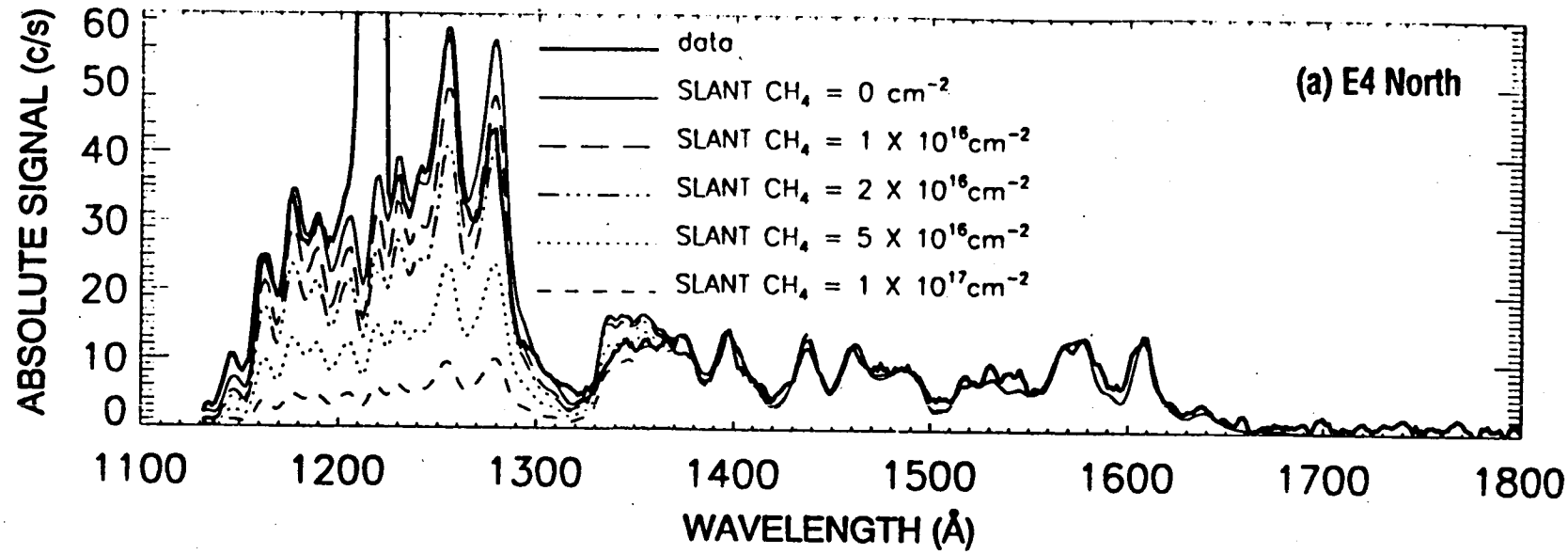
ABSOLUTE SIGNAL (c/s)
60
50
40
30
20
10
0
data
SLANT CH_4 = 0 cm^{-2}
SLANT CH_4 = 1 X $10^{16}cm^{-2}$
SLANT CH_4 = 2 X $10^{16}cm^{-2}$
SLANT CH_4 = 5 X $10^{16}cm^{-2}$
SLANT CH_4 = 1 X $10^{17}cm^{-2}$
(a) E4 North
1100
1200
1300
1400
1500
1600
1700
1800
WAVELENGTH (Å)

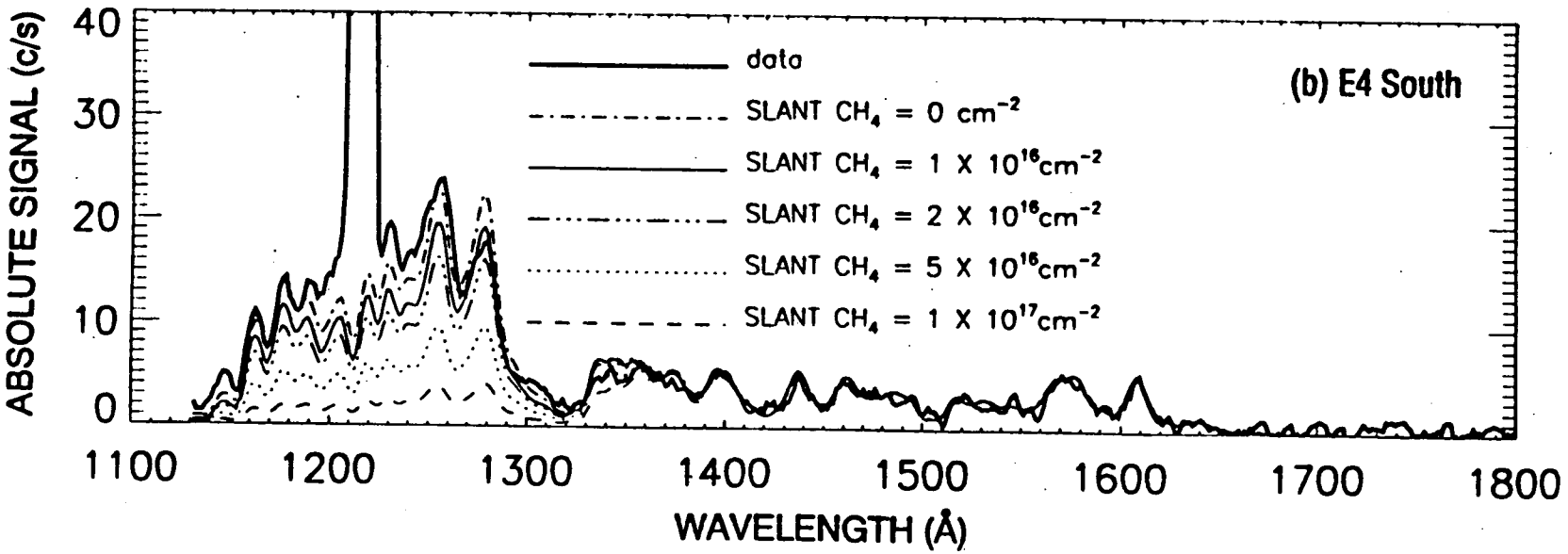
ABSOLUTE SIGNAL (c/s)
40
30
20
10
0
data
SLANT CH_4 = 0 cm^{-2}
SLANT CH_4 = 1 X $10^{16}cm^{-2}$
SLANT CH_4 = 2 X $10^{16}cm^{-2}$
SLANT CH_4 = 5 X $10^{16}cm^{-2}$
SLANT CH_4 = 1 X $10^{17}cm^{-2}$
(b) E4 South
1100
1200
1300
1400
1500
1600
1700
1800
WAVELENGTH (Å)

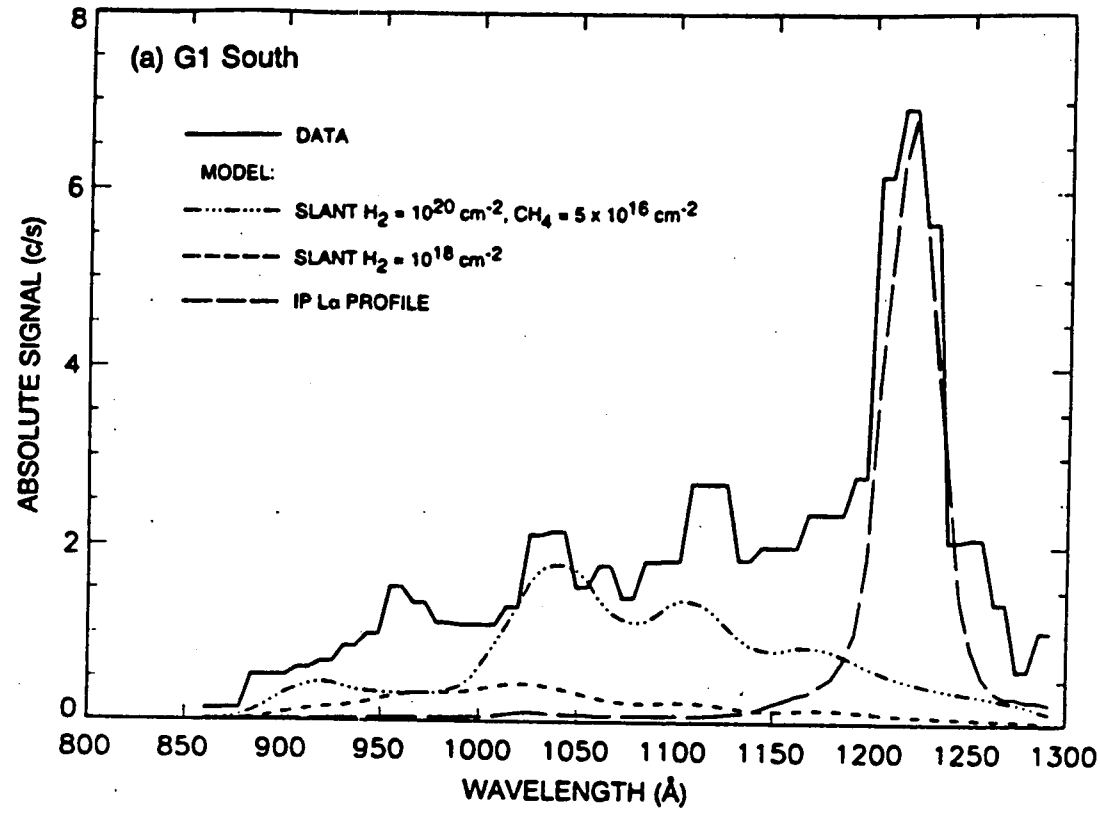
(a) G1 South
DATA
MODEL:
SLANT $H_2 = 10^{20}$ cm^{-2}, $CH_4 = 5 \times 10^{16}$ cm^{-2}
SLANT $H_2 = 10^{18}$ cm^{-2}
IP Lα PROFILE
ABSOLUTE SIGNAL (c/s)
WAVELENGTH (Å)
0
2
4
6
8
800
850
900
950
1000
1050
1100
1150
1200
1250
1300

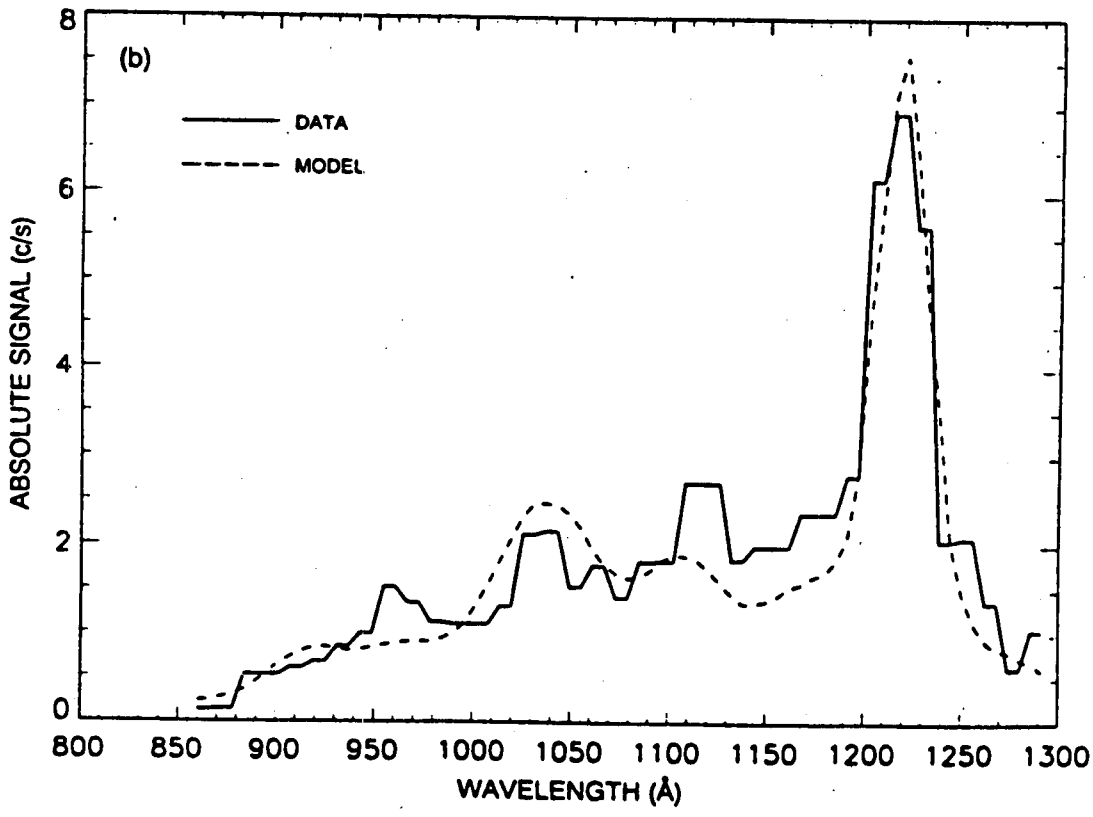
(b)
DATA
MODEL
ABSOLUTE SIGNAL (c/s)
WAVELENGTH (Å)
0
2
4
6
8
800
850
900
950
1000
1050
1100
1150
1200
1250
1300

Fig. 17

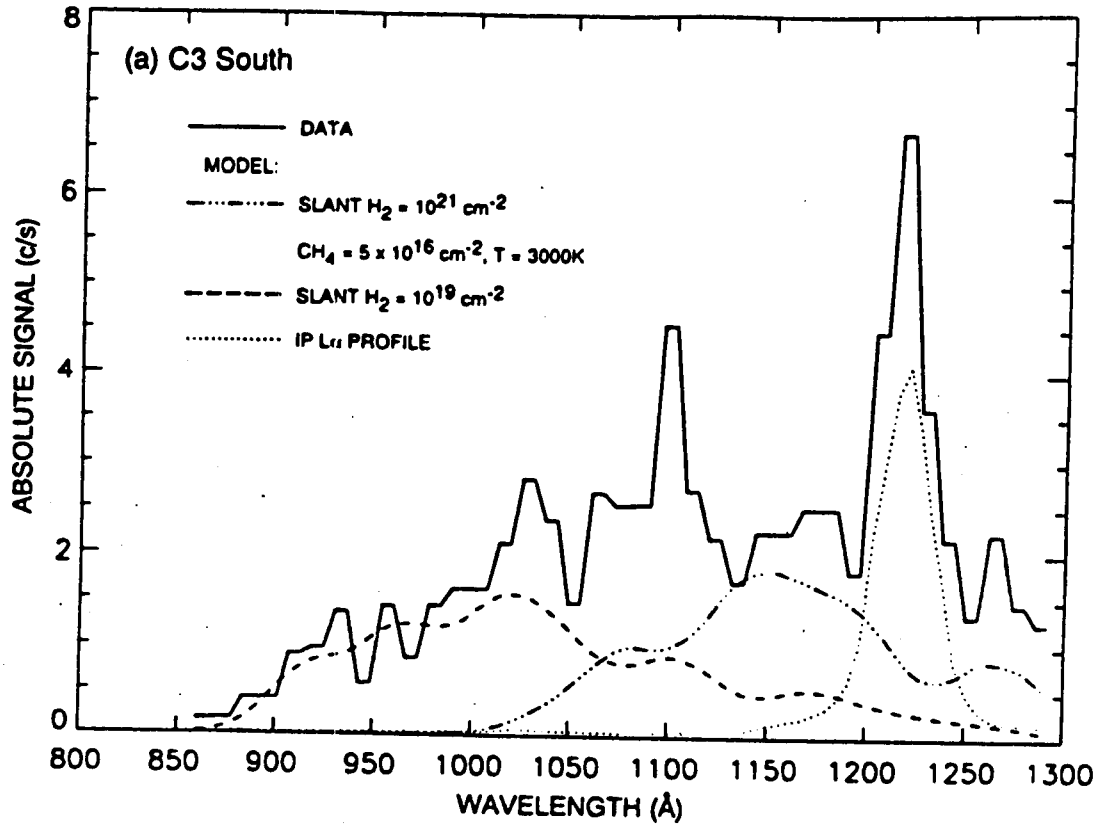
(a) C3 South
DATA
MODEL:
SLANT $H_2 = 10^{21}$ cm^{-2}
$CH_4 = 5 \times 10^{16}$ cm^{-2}, T = 3000K
SLANT $H_2 = 10^{19}$ cm^{-2}
IP Lα PROFILE
ABSOLUTE SIGNAL (c/s)
WAVELENGTH (Å)
0
2
4
6
8
800
850
900
950
1000
1050
1100
1150
1200
1250
1300

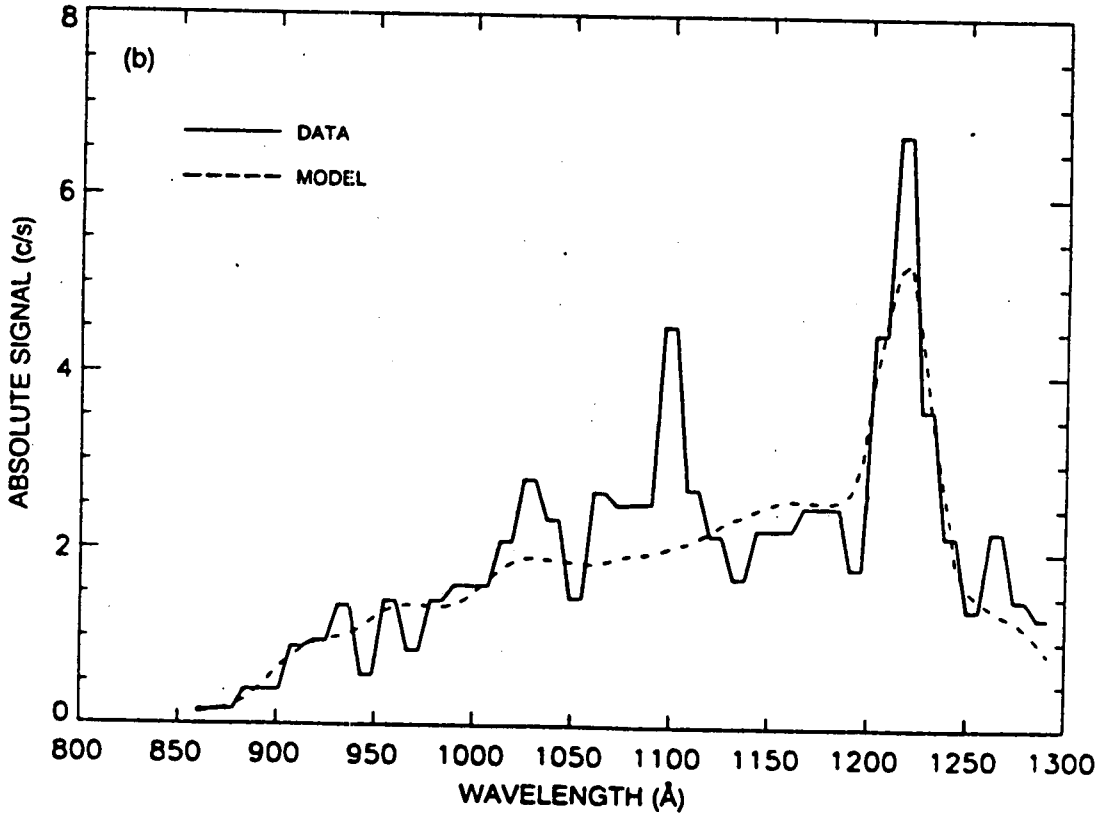
(b)
DATA
MODEL
ABSOLUTE SIGNAL (c/s)
WAVELENGTH (Å)
0
2
4
6
8
800
850
900
950
1000
1050
1100
1150
1200
1250
1300

Fig. 18

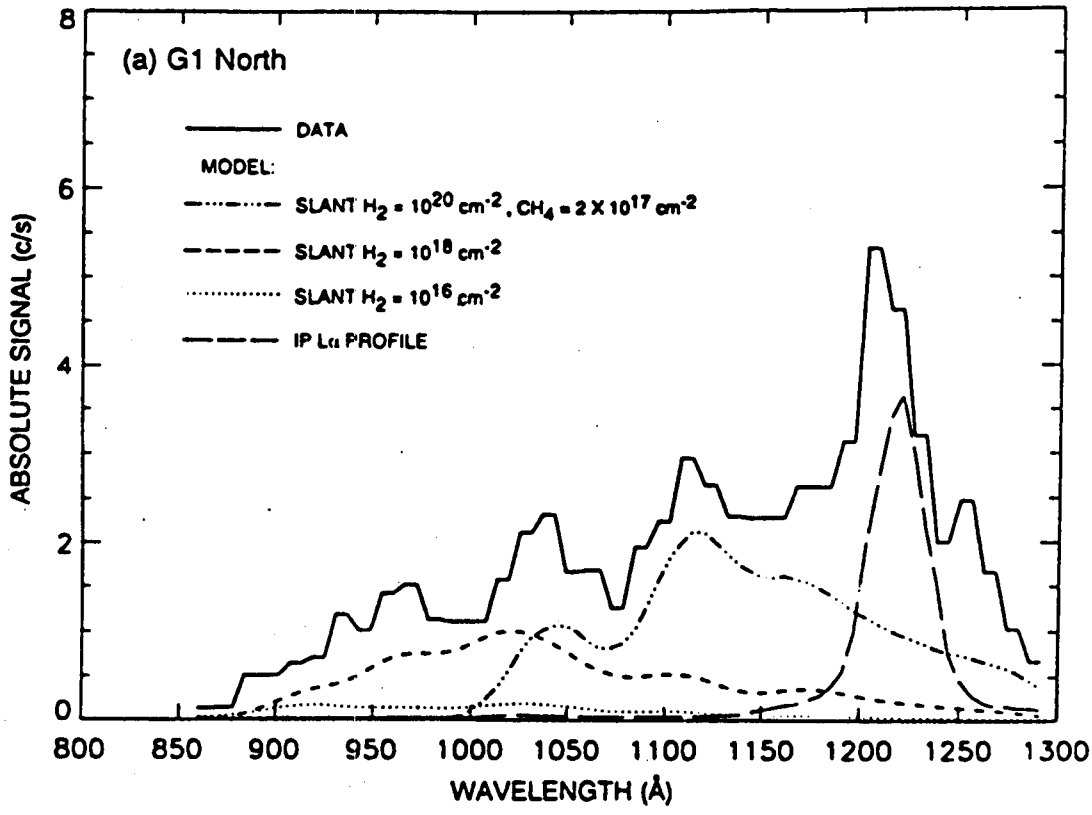
(a) G1 North
DATA
MODEL:
SLANT $H_2 = 10^{20}$ cm^{-2}, $CH_4 = 2 \times 10^{17}$ cm^{-2}
SLANT $H_2 = 10^{18}$ cm^{-2}
SLANT $H_2 = 10^{16}$ cm^{-2}
IP Lα PROFILE
ABSOLUTE SIGNAL (c/s)
WAVELENGTH (Å)
0
2
4
6
8
800
850
900
950
1000
1050
1100
1150
1200
1250
1300

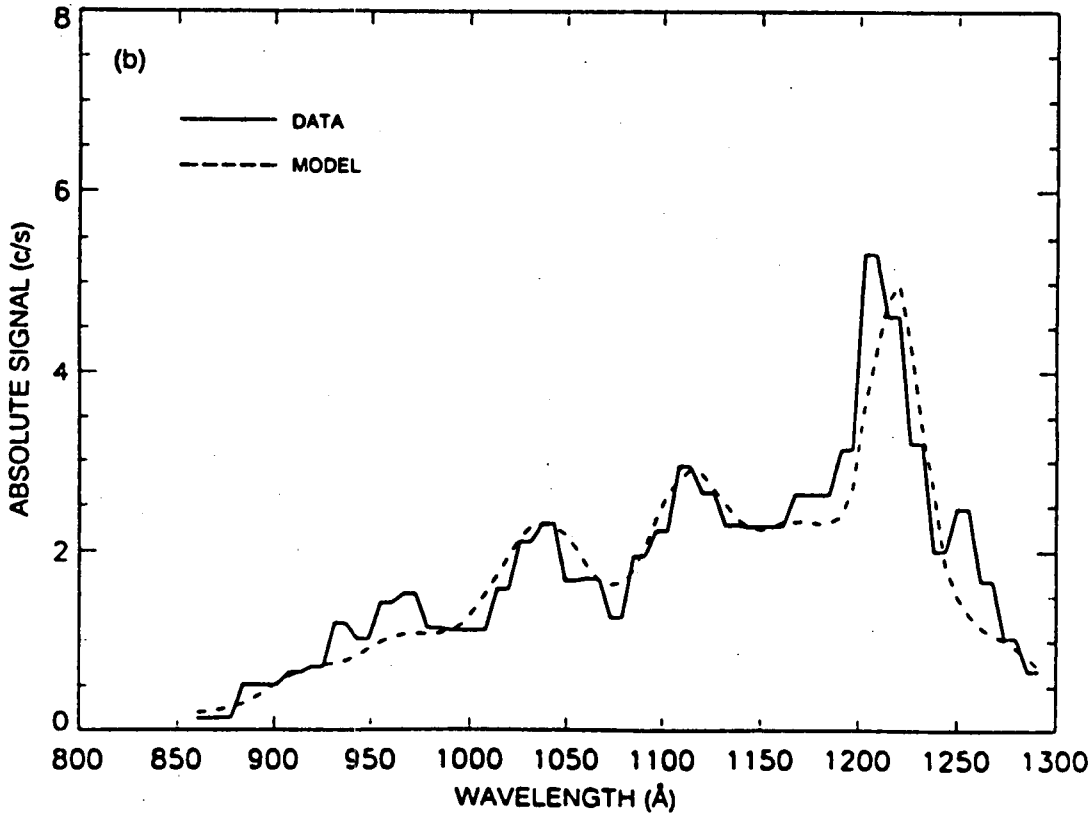
(b)
DATA
MODEL
ABSOLUTE SIGNAL (c/s)
WAVELENGTH (Å)
0
2
4
6
8
800
850
900
950
1000
1050
1100
1150
1200
1250
1300

Fig. 19

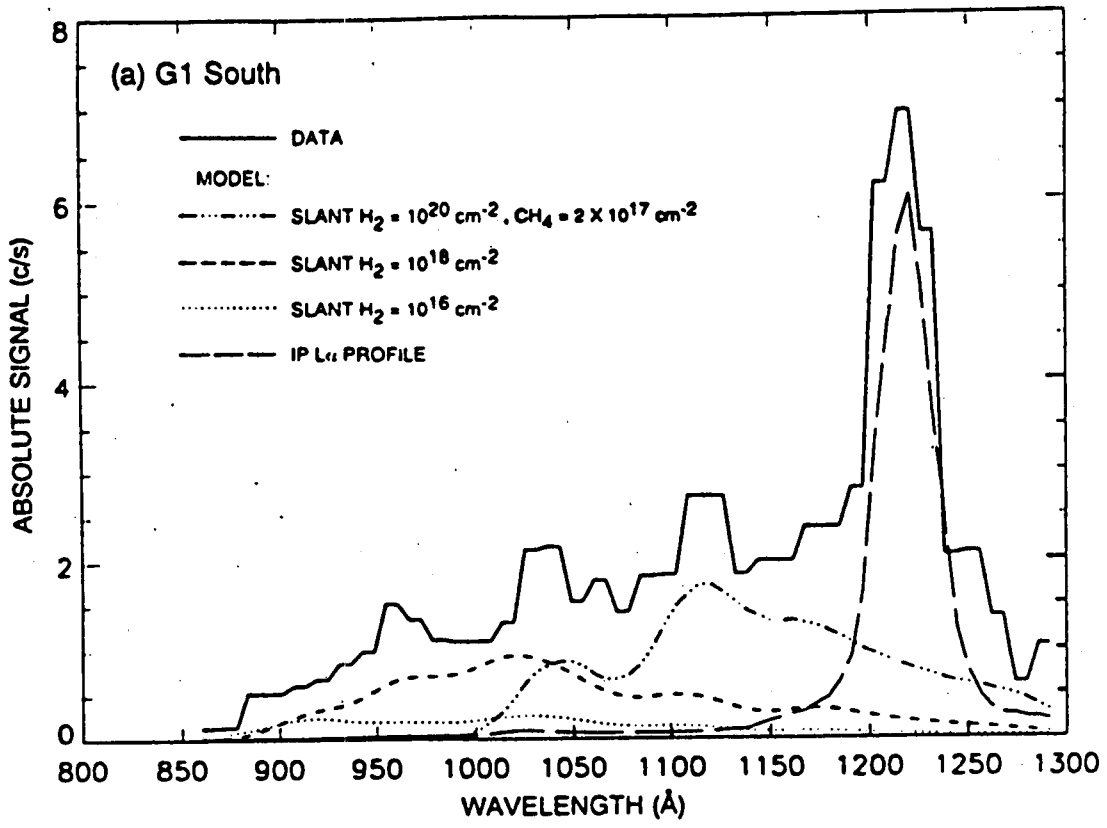
(a) G1 South
DATA
MODEL:
SLANT $H_2 = 10^{20}$ cm^{-2}, $CH_4 = 2 \times 10^{17}$ cm^{-2}
SLANT $H_2 = 10^{18}$ cm^{-2}
SLANT $H_2 = 10^{16}$ cm^{-2}
IP Lα PROFILE
ABSOLUTE SIGNAL (c/s)
WAVELENGTH (Å)
0
2
4
6
8
800
850
900
950
1000
1050
1100
1150
1200
1250
1300

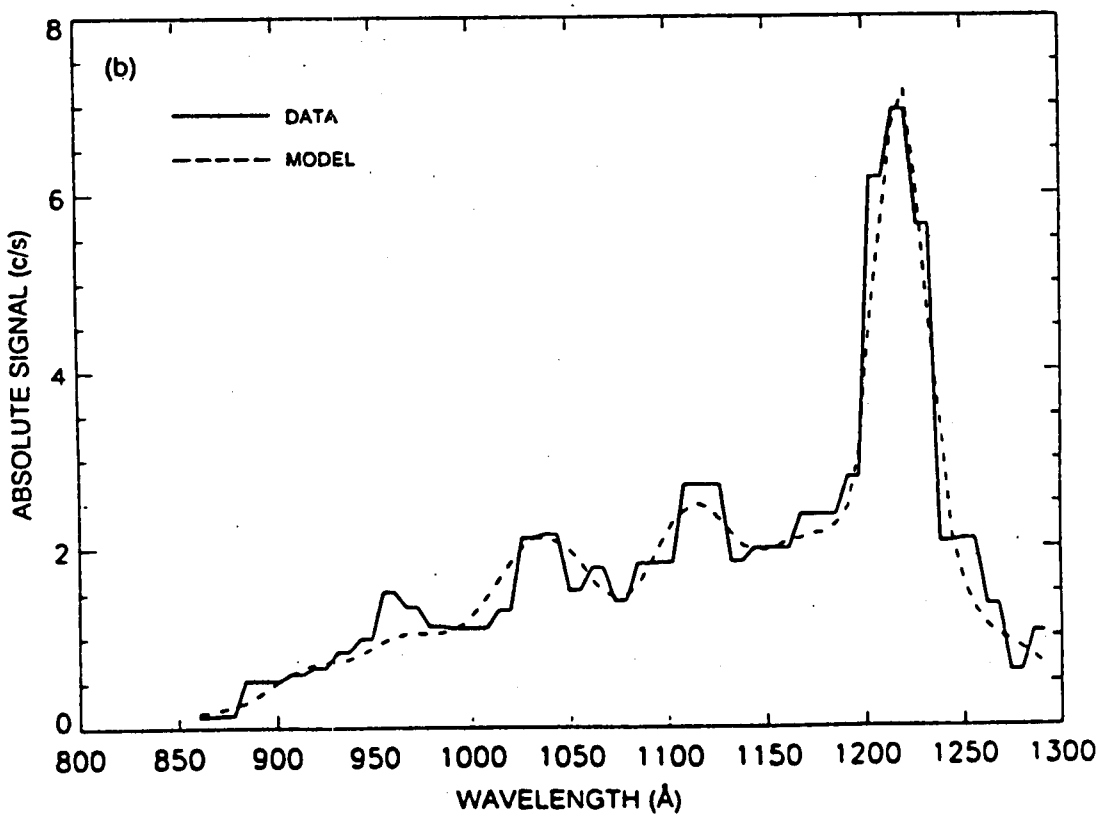
(b)
DATA
MODEL
ABSOLUTE SIGNAL (c/s)
WAVELENGTH (Å)
0
2
4
6
8
800
850
900
950
1000
1050
1100
1150
1200
1250
1300

Fig. 20

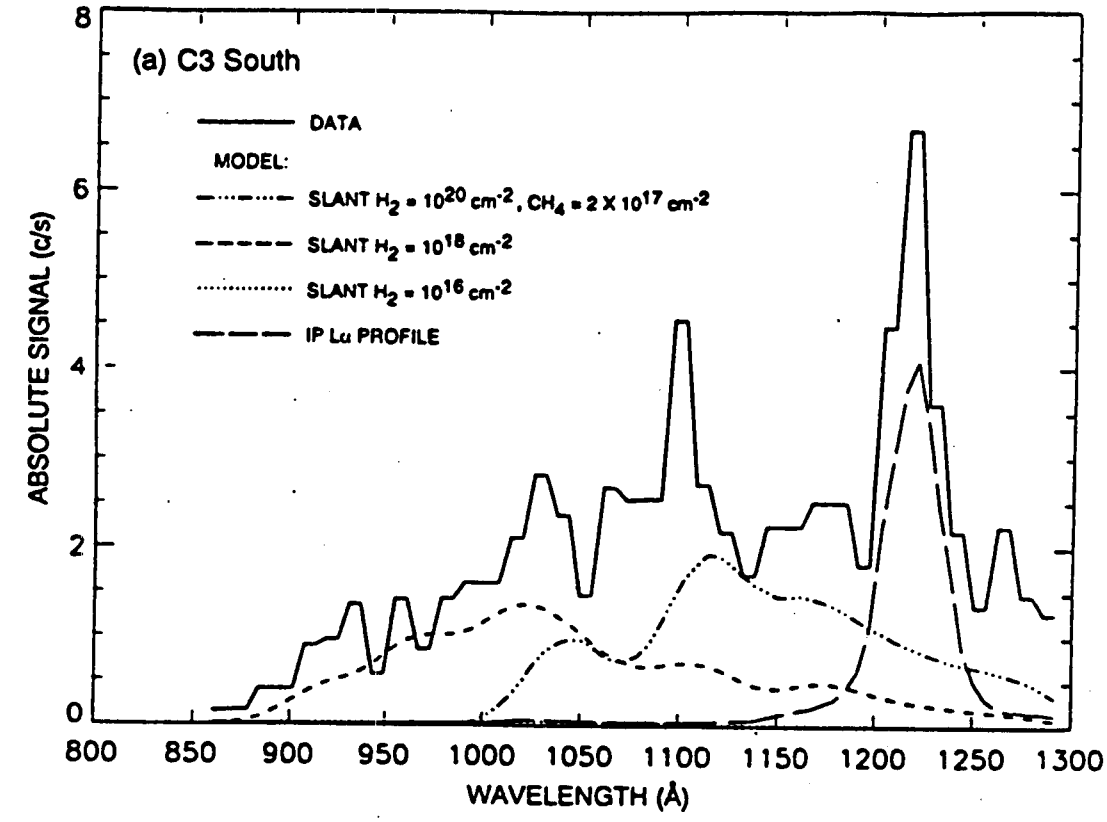
(a) C3 South
DATA
MODEL:
SLANT $H_2 = 10^{20}$ cm^{-2}, $CH_4 = 2 \times 10^{17}$ cm^{-2}
SLANT $H_2 = 10^{18}$ cm^{-2}
SLANT $H_2 = 10^{16}$ cm^{-2}
IP Lα PROFILE
ABSOLUTE SIGNAL (c/s)
WAVELENGTH (Å)
0
2
4
6
8
800
850
900
950
1000
1050
1100
1150
1200
1250
1300

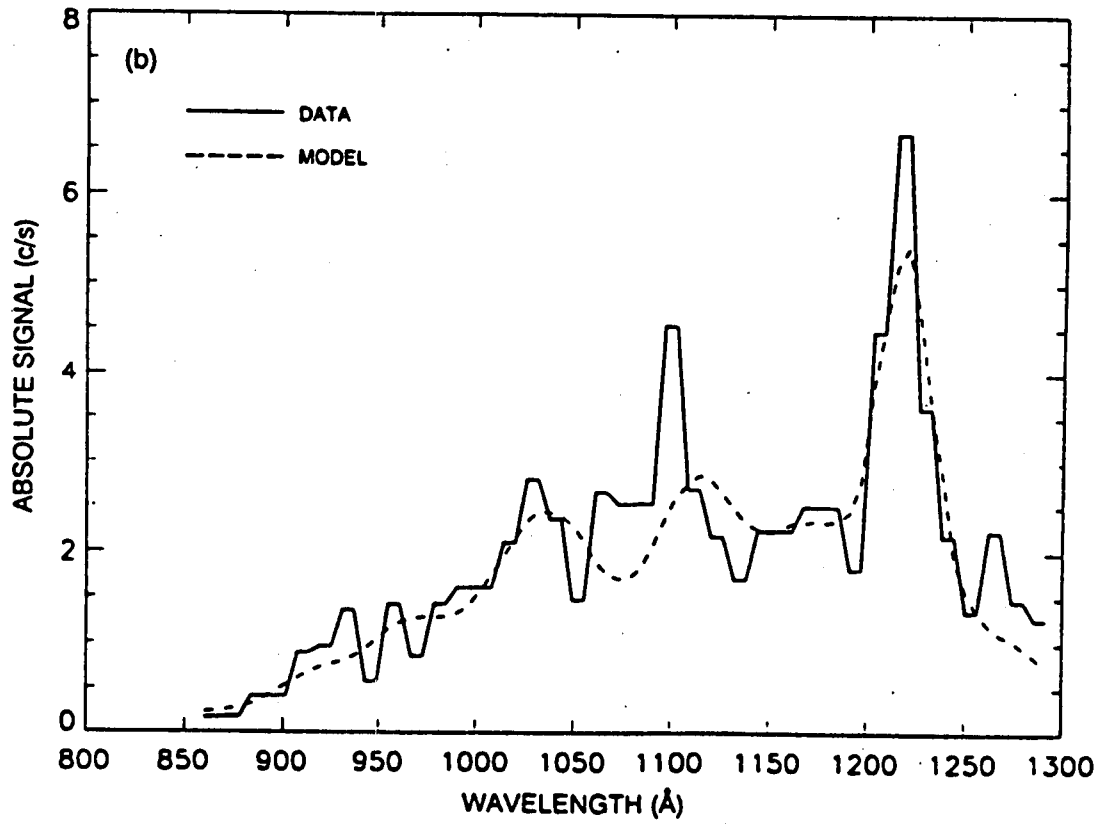
(b)
DATA
MODEL
ABSOLUTE SIGNAL (c/s)
WAVELENGTH (Å)
0
2
4
6
8
800
850
900
950
1000
1050
1100
1150
1200
1250
1300

Fig. 21

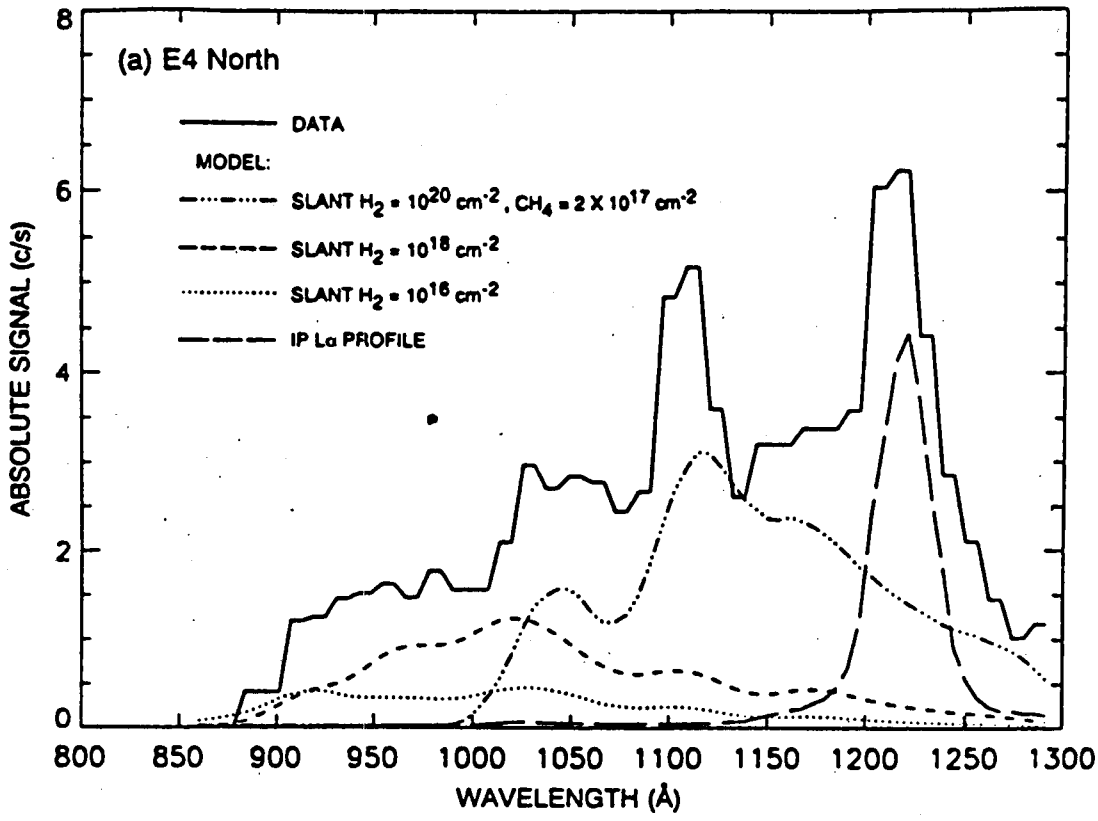
(a) E4 North
DATA
MODEL:
SLANT $H_2 = 10^{20}$ cm^{-2}, $CH_4 = 2 \times 10^{17}$ cm^{-2}
SLANT $H_2 = 10^{18}$ cm^{-2}
SLANT $H_2 = 10^{16}$ cm^{-2}
IP Lα PROFILE
ABSOLUTE SIGNAL (c/s)
WAVELENGTH (Å)
0
2
4
6
8
800
850
900
950
1000
1050
1100
1150
1200
1250
1300

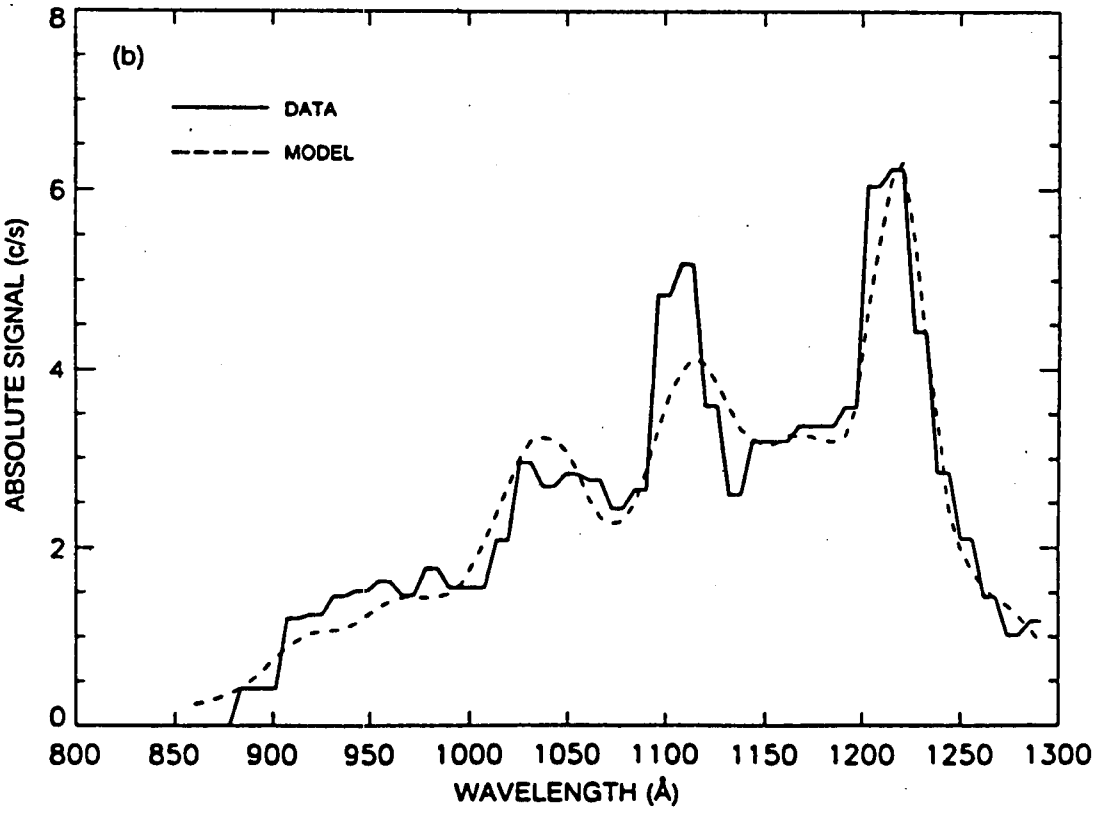
(b)
DATA
MODEL
ABSOLUTE SIGNAL (c/s)
WAVELENGTH (Å)
0
2
4
6
8
800
850
900
950
1000
1050
1100
1150
1200
1250
1300

Fig. 22

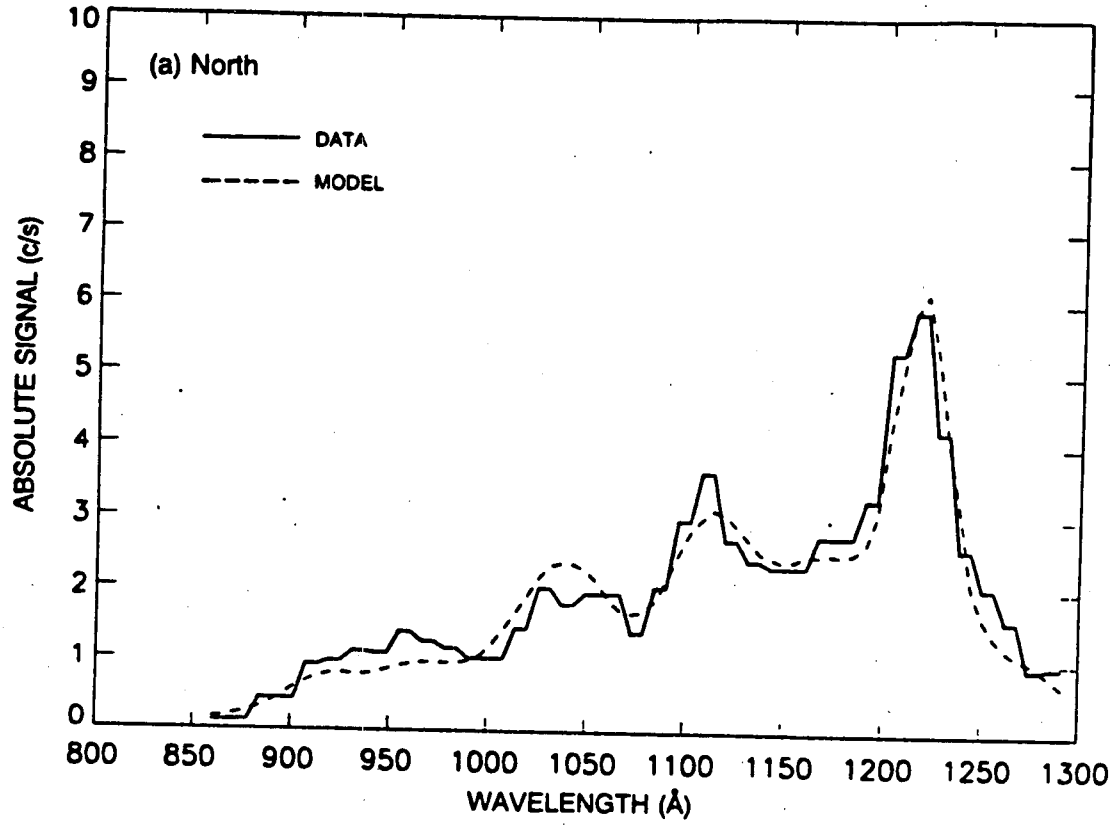
(a) North
DATA
MODEL
ABSOLUTE SIGNAL (c/s)
WAVELENGTH (Å)
0
1
2
3
4
5
6
7
8
9
10
800
850
900
950
1000
1050
1100
1150
1200
1250
1300

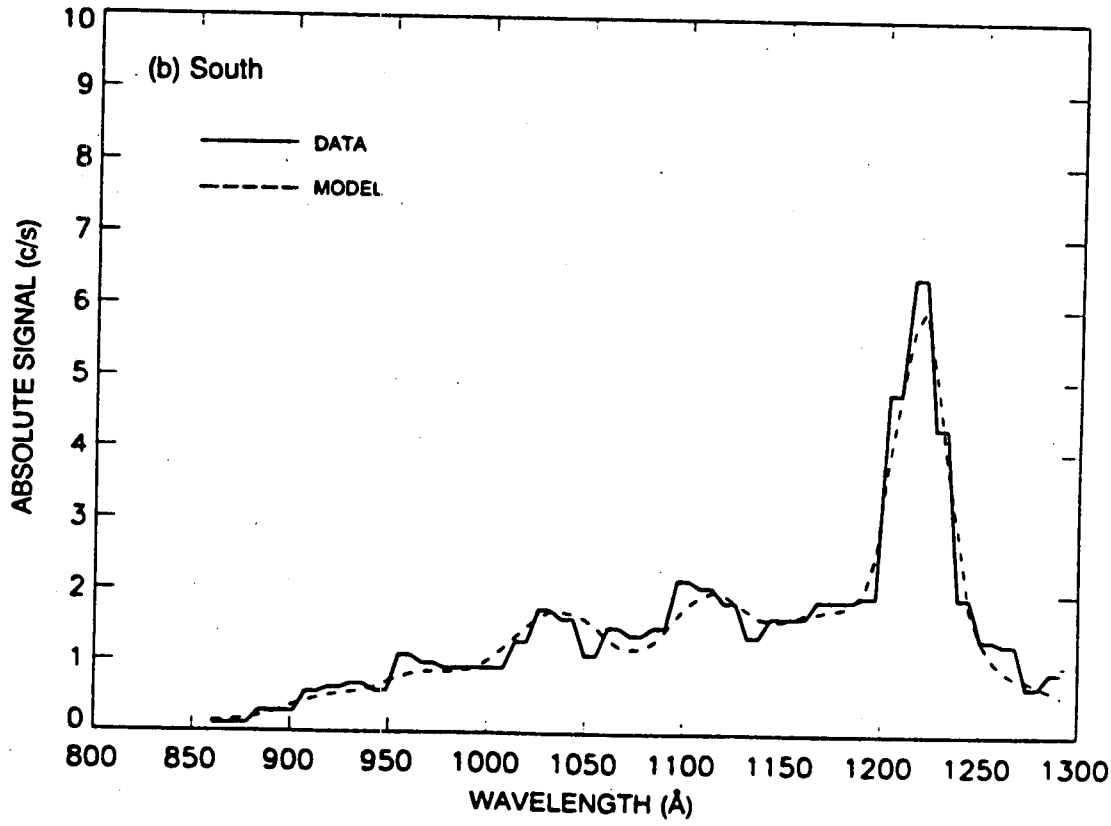
(b) South
DATA
MODEL
ABSOLUTE SIGNAL (c/s)
WAVELENGTH (Å)
0
1
2
3
4
5
6
7
8
9
10
800
850
900
950
1000
1050
1100
1150
1200
1250
1300

Fig. 23

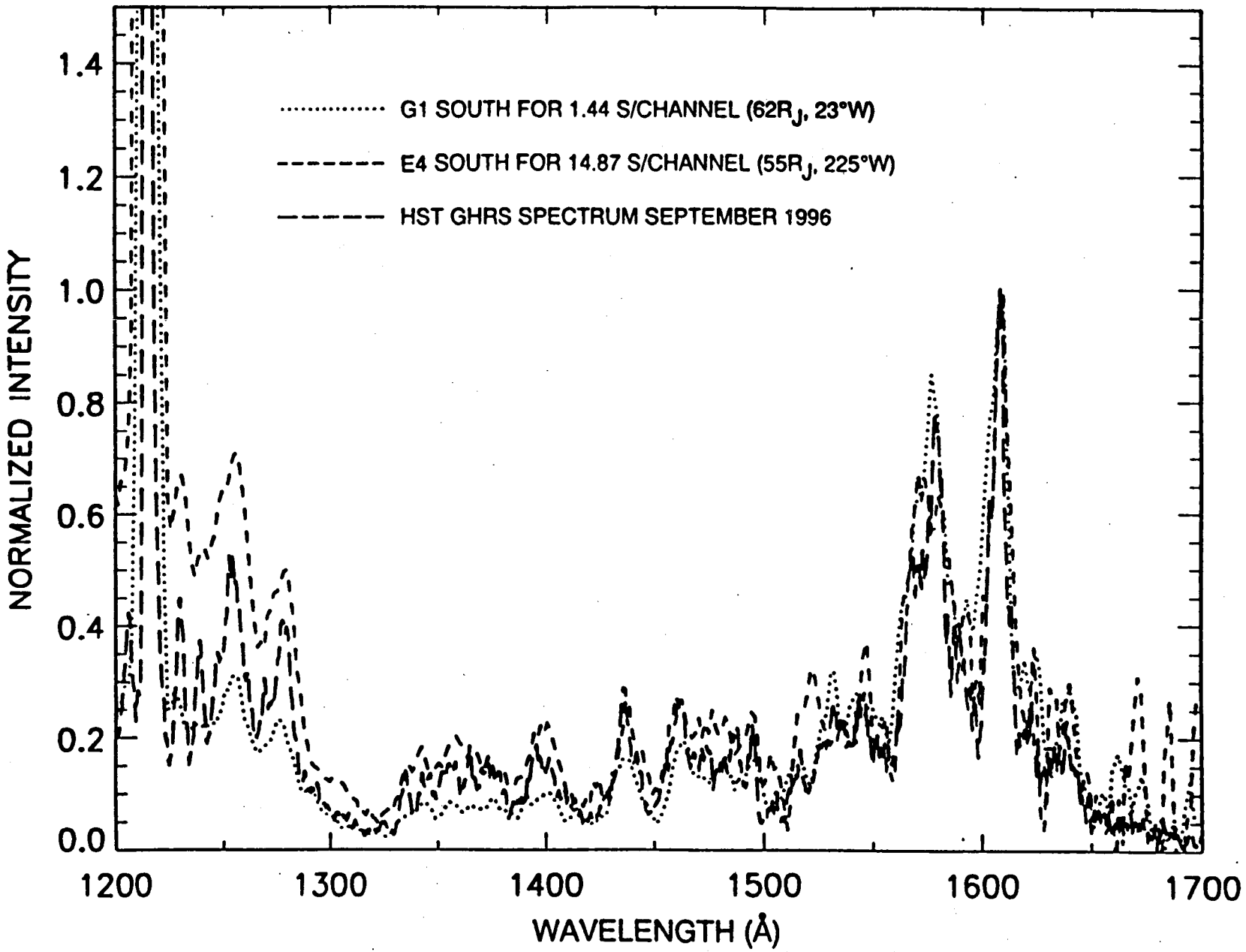
G1 SOUTH FOR 1.44 S/CHANNEL (62R$_J$, 23°W)
E4 SOUTH FOR 14.87 S/CHANNEL (55R$_J$, 225°W)
HST GHRS SPECTRUM SEPTEMBER 1996
NORMALIZED INTENSITY
0.0
0.2
0.4
0.6
0.8
1.0
1.2
1.4
1200
1300
1400
1500
1600
1700
WAVELENGTH (Å)

Fig. 24

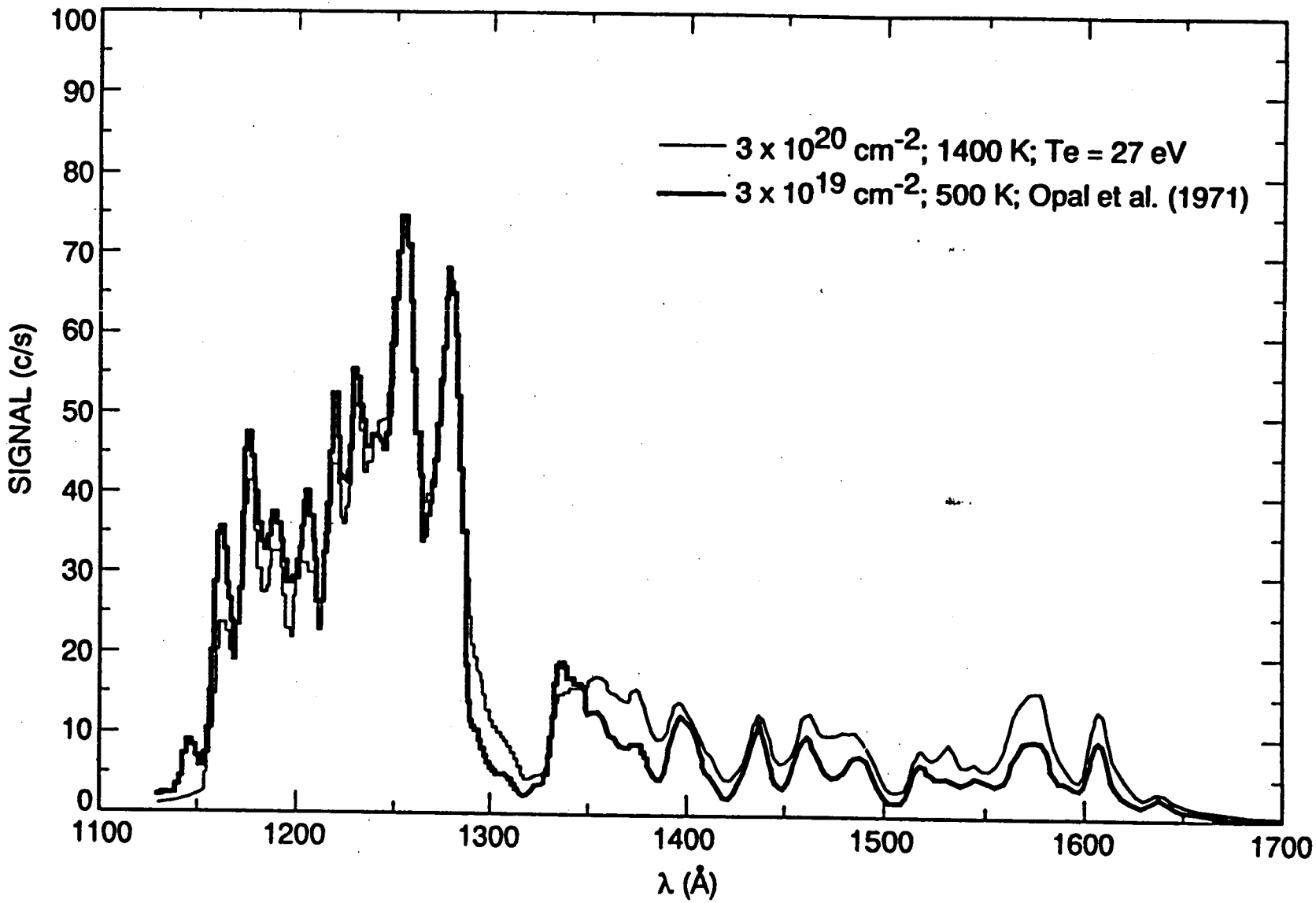
100
90
80
70
60
50
40
30
20
10
0
SIGNAL (c/s)
1100
1200
1300
1400
1500
1600
1700
λ (Å)
3 x 10^20 cm^-2; 1400 K; Te = 27 eV
3 x 10^19 cm^-2; 500 K; Opal et al. (1971)

Fig. 25

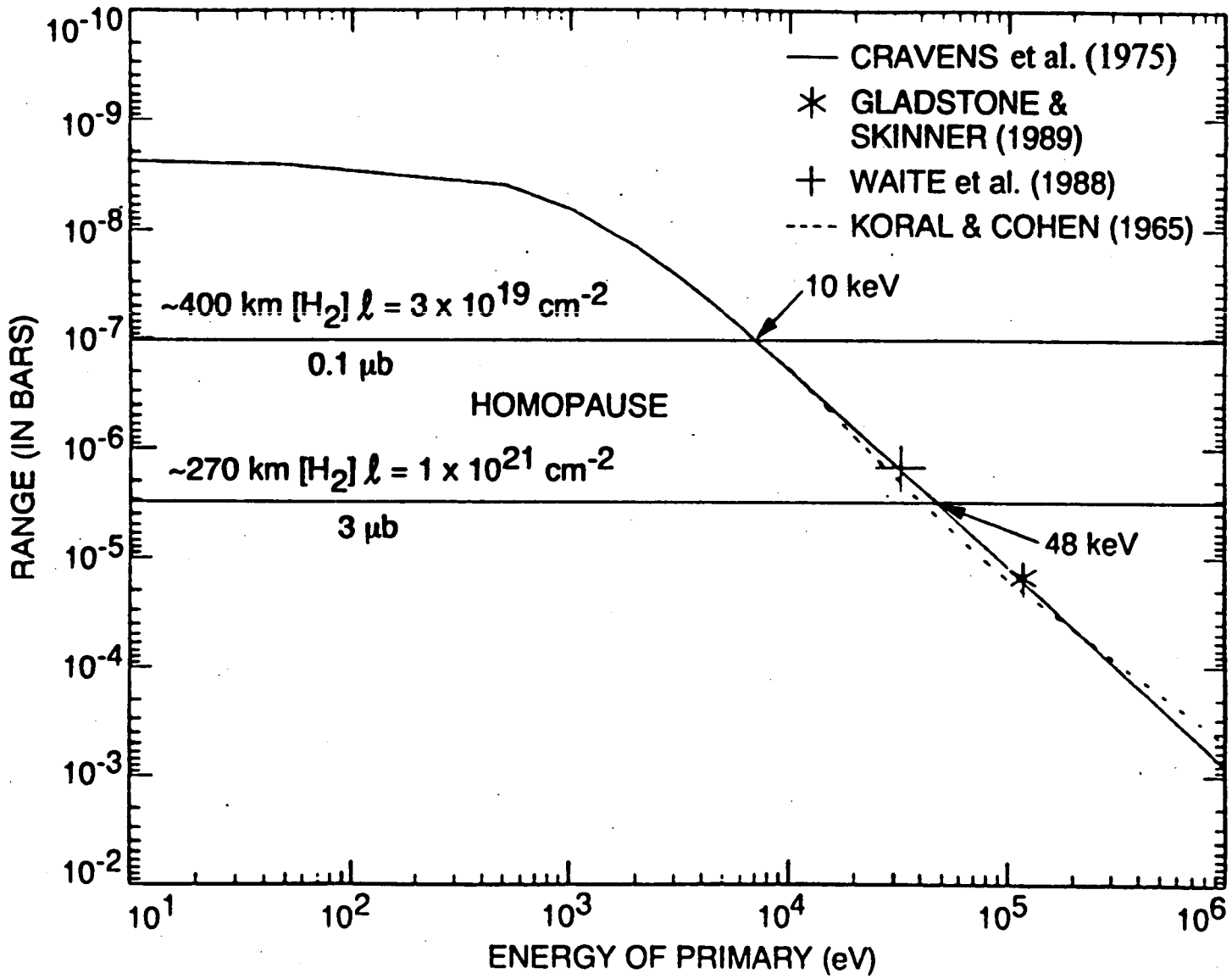
CRAVENS et al. (1975)
GLADSTONE & SKINNER (1989)
WAITE et al. (1988)
KORAL & COHEN (1965)
10 keV
48 keV
~400 km [H2] ℓ = 3 x 10^19 cm^-2
0.1 μb
HOMOPAUSE
~270 km [H2] ℓ = 1 x 10^21 cm^-2
3 μb
RANGE (IN BARS)
ENERGY OF PRIMARY (eV)
10^-10
10^-9
10^-8
10^-7
10^-6
10^-5
10^-4
10^-3
10^-2
10^1
10^2
10^3
10^4
10^5
10^6

Fig. 26